Monitoring seismicity in the context of activities in the deep subsurface of Flanders

Opvolging van seismiciteit in de context van toepassingen in de diepe ondergrond van Vlaanderen

Michel Van Camp, Koen Van Noten, Thomas Lecocq, Kris Vanneste

Royal Observatory of Belgium, Ringlaan 3, 1180 Brussel

REPORT ROB-VPO 2020-01

Commissioned by:

Vlaams Planbureau voor Omgeving
Graaf De Ferraris
Koning Albert II laan 20, bus 8
1000 Brussels
Belgium

Vlaanderen

31 January 2020

Table of contents

1. RATIONALE

1.1 CONTEXT: EXPERTISE REQUESTED BY VPO ON 24 JULY 2019

In 2007, Flanders asked to review the natural seismic activity and seismic hazard probability of Flanders and its surroundings. The main contractor was the Royal Observatory of Belgium and the final report (VLA07-4.2) was finalised in 2009. Flanders, in cooperation with the Royal Observatory of Belgium, also took the initiative in 2008 to install a seismometer at depth (in a newly drilled borehole to a depth of 307 m in Oostende) so that Flanders would have a qualitative measuring point at which the seismometer would be anchored directly in hard rock.

For applications in the deep subsurface that influence the local pressure conditions there is a risk of the occurrence of induced (micro)seismicity. Although a large volume of natural gas is stored in the deep subsurface of Flanders for more than 40 years, no seismic monitoring has ever been carried out to monitor subsurface activities. During the first deep geothermal project at Balmatt that started in 2016, a seismic monitoring was set up on the project's own initiative. Hundreds of earthquakes were registered at the start of these geothermal activities. In the future, Flanders aims at better monitoring the natural and induced seismicity for all activities in the deep subsurface.

Through the Flemish legislation on the deep subsurface (*Vlaams decreet inzake de diepe ondergrond; DDO*) Flanders is able to request a measurement plan on seismic monitoring for Flemish subsurface activities, if it appears necessary. For federal activities that take place in the deep subsurface of Flanders, such as the strategic gas storage, monitoring can be imposed through the Flemish regulation by an environmental permit.

The Flemish Planning Bureau for the Environment and Spatial Development (VPO) would like to investigate 1) to what extent (magnitude) the existing Belgian seismometer network (UCC) can register natural and induced tremors in Flanders; 2) how an operator best installs and operates a seismic monitoring network and which aspects should be taken into account in a measurement plan; 3) how monitoring results can be assessed in a responsible way in relation to the Flemish geological and seismic context. In addition, Flanders also wants to gain insight into the baseline (zero reference) seismicity prior to the start of subsurface activities and what may be needed to establish a reliable baseline for the future.

[NL] *Vlaanderen liet in 2007 de natuurlijke seismische activiteit en de seismische gevarenkans in Vlaanderen en zijn omgeving onderzoeken. De hoofdopdrachtnemer was de Koninklijke Sterrenwacht van België en het eindrapport (VLA07-4.2) werd in 2009 gefinaliseerd.*

Vlaanderen nam, in samenwerking met de Koninklijke Sterrenwacht van België, in 2008 eveneens initiatief om een seismometer op diepte (in een nieuw uitgevoerd boorgat tot 307 m diepte te Oostende) te installeren zodat Vlaanderen over een kwalitatief meetpunt zou beschikken waarbij de seismometer rechtstreeks in hard sokkelgesteente verankerd is.

Bij toepassingen in de diepe ondergrond die de lokale drukcondities beïnvloeden bestaat een risico op het optreden van geïnduceerde (micro)seismiciteit. Hoewel er al meer dan 40 jaar een groot volume aan aardgas wordt opgeslagen in de diepe ondergrond van Vlaanderen werd er geen seismische monitoring uitgevoerd. Het eerste diepe geothermieproject dat in 2016 gestart is, heeft op eigen initiatief een seismische monitoring opgezet. Bij aanvang van de activiteiten zijn enkele honderden

aardbevingen geregistreerd. Vlaanderen wil daarom in de toekomst de seismiciteit voor alle toepassingen in haar diepe ondergrond beter opvolgen.

In de wetgeving (Vlaams decreet inzake de diepe ondergrond; DDO) is voorzien om voor de Vlaams bevoegde toepassingen waar nodig een meetplan voor monitoring op te leggen. Voor de federaal bevoegde toepassingen die plaatsvinden in de diepe ondergrond van Vlaanderen, zoals de ondergrondse strategische gasopslag, kan monitoring opgelegd worden via de Vlaamse regelgeving inzake de omgevingsvergunning.

Het Vlaams Planbureau voor Omgeving (VPO) van het departement Omgeving wenst nu te laten onderzoeken 1) in hoeverre het bestaande netwerk van seismometers toelaat de natuurlijke en geïnduceerde bevingen in Vlaanderen te registreren; 2) hoe monitoring best verloopt en met welke aspecten rekening gehouden dient te worden in een meetplan; 3) hoe de monitoringsresultaten op een verantwoorde manier beoordeeld kunnen worden in functie van de Vlaamse geologische en seismische context. Daarnaast wil Vlaanderen zicht krijgen op de baseline (nulreferentie) seismiciteit van vóór aanvang van ondergrondse activiteiten en wat eventueel nodig is om een betrouwbare baseline voor de toekomst vast te leggen.

1.2 AIM OF THIS STUDY

This study provides expertise to the Flemish government for implementing a policy on seismic monitoring and deep subsurface management. In this report, the Royal Observatory of Belgium provides:

- An update of the earthquake catalogs including the tectonic - natural - earthquake catalog, the full instrumental catalog since 1910 and a list of induced earthquakes at Balmatt since 2016 (Chapter 2);
- An overview of the detection capability of the Belgian seismic network, the capability of borehole seismometers and an explanation why local and regional seismic networks can provide different magnitudes (Chapter 3);
- An explanation of the design and minimal needs for installing a local network, how to test the capability of this network using the local geological information (Chapter 4);
- An unambiguous discrimination between natural and induced seismicity (Chapter 5);
- A discussion on critical parameters that need to be monitored during a geothermal operation, in which units and according to which protocols, and an overview on Traffic Light Systems (Chapter 6);
- An overview of research that best needs to be investigated on the long term to understand seismicity responding to geothermal activities (Chapter 7).

[NL] *In deze studie biedt de Koninklijke Sterrenwacht van België expertise aan om een onderbouwd beleid inzake seismische monitoring en inzake beheer van de diepe ondergrond te kunnen voeren. In dit rapport voorziet de Koninklijke Sterrenwacht van België:*

- *Een update van de aardbevingscatalogi inclusief de tektonische - natuurlijke - aardbevingscatalogus, de volledige instrumentele catalogus sinds 1910 en een lijst van geïnduceerde aardbevingen te Balmatt sinds 2016 op basis van template matching (Hoofdstuk 2);*

- *Een overzicht over de bekwaamheid van het Belgische seismische netwerk om aardbevingen op te sporen, een aanbeveling van de mogelijkheden van boorgatseismometers en een discussie waarom lokale en regionale seismische netwerken verschillende magnitudes kunnen leveren (Hoofdstuk 3);*
- *Een uitleg over het ontwerp en de minimale set-up van een lokaal seismisch netwerk om ondergrondse activiteiten op te sporen, hoe de capaciteit van dit netwerk zou moeten worden getest, o.a. met behulp van de lokale geologische informatie (Hoofdstuk 4);*
- *Een discussie over het verschil tussen natuurlijke en geïnduceerde aardbevingen (Hoofdstuk 5);*
- *Een overzicht welke parameters moeten worden gemonitord tijdens een geothermische operatie, in welke eenheden en volgens welke protocollen, en een overzicht van verkeerslichtsystemen (Hoofdstuk 6);*
- *Een overzicht van het onderzoek dat het best op lange termijn kan worden uitgevoerd om de seismiciteit gerelateerd aan geothermische activiteiten beter te begrijpen (Hoofdstuk 7).*

2. EARTHQUAKE CATALOGS

2.1 INTRODUCTION

In this section, we provide three different earthquake catalogs for Flanders and neighboring areas:

- The catalog of natural (i.e., tectonic) earthquakes since the middle of the 14th century: this is an expansion of the catalog provided in project VLA07-4.2 (Vanneste *et al.*, 2009), containing all new seismicity that occurred since 2009, as well as updated parameters of some earlier earthquakes;
- The full catalog of instrumental seismicity since 1910: besides known earthquakes, this catalog also includes suspected earthquakes, known and suspected induced earthquakes, known and suspected quarry blasts, known and suspected rockbursts, known and suspected mine explosions, known and suspected experimental explosions and known and suspected controlled explosions.
- A list of induced earthquakes at Balmatt since 2016 based on a template matching technique.

2.2 CATALOG OF TECTONIC EARTHQUAKES

Overview

The catalog of tectonic earthquakes comprises all events that are marked as "known earthquake" (ke) in the ROB database. This database is based on two types of information: historical archives for earthquakes before the twentieth century, and instrumental records for earthquakes since ~1910 AD. Currently, the catalog contains 2270 events in the rectangular area between 1° and 8° E and between 49° and 52° N, and in the time period between 1 January 1350 and 31 December 2019. A map of this catalog is shown in Figure 1.

Since the VLA07-4.2 report in 2009, ROB has recorded 832 new earthquakes. Of those, three have a local magnitude (M_L) ≥ 4.0, three have M_L between 3.0 and 4.0, and 66 have M_L between 2.0 and 3.0. All earthquakes with $M_L \geq 2.0$ are listed in Table 1. During this period, the largest event with epicenter in Flanders was the M_L=3.1 earthquake of 2018-05-25 near Kinrooi, and the largest event overall was the M_L=4.3 earthquake of 2011-09-08 near Goch, Germany.

Since 2009, six earthquakes have been felt by the population in Flanders:

- 2009-03-03, Court-Saint-Etienne, M_L=2.8: this earthquake is part of a sequence in Walloon Brabant that started in 2008 (see VLA07-4.2 report; Van Noten *et al.,* 2015);
- 2009-08-05, Zutendaal, M_L=2.7;
- 2011-08-02, Veldegem, M_L=2.4;
- 2011-09-08, Goch (Germany), M_L=4.3 (Van Noten *et al.,* 2017);
- 2015-05-22, Ramsgate (UK), M_L=4.1 (Van Noten *et al.,* 2017);
- 2018-05-25, Kinrooi, M_L=3.1.

Macroseismic maps of these events based on the online "Did You Feel It" (DYFI) enquiry of the ROB are shown in Figure 2. These maps indicate how strongly (intensity), and over which area, the earthquakes have been felt by the local population. We refer to the VLA07-4.2 report for a detailed description of the macroseismic intensity scale. These maps only show the macroseismic data received

by the ROB. Complete macroseismic maps of the Goch and Ramsgate cross-border felt earthquakes were developed by merging macroseismic data of seismological institutes of neighbouring countries (see Van Noten *et al.,* 2017). The 2015-05-22 earthquake near Ramsgate (UK) was felt over the largest area. In all cases, intensities were low (II to III), locally reaching IV for the 2009-08-05 earthquake near Zutendaal. None of these earthquakes caused any damage in Flanders.

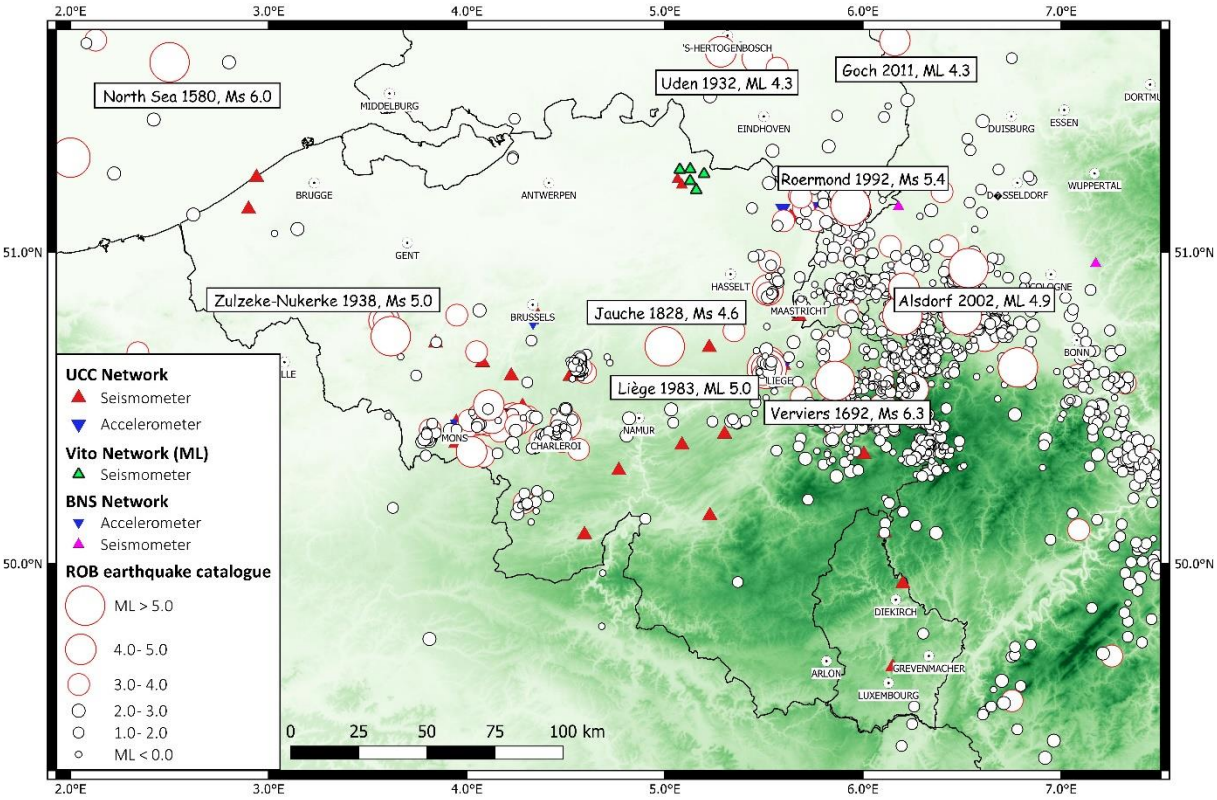

Figure 1: *ROB seismic catalog of tectonic earthquakes (01-01-1350 to 31-10-2019, code: ke = known earthquakes) with indication of most important seismic events.*

2. Earthquake catalogs

Table 1: *Tectonic earthquakes with intensities and local magnitude $M_L \geq 2.0$ recorded since 2009.*

ID	Date	Time	Name	Lon	Lat	Z	M_L	M_S	I_{max}
3252	2009-02-21	13:21:21	COURT-SAINT-ETIENNE (BE)	4.571	50.631	5.0	2.0		3.0
3273	2009-03-03	03:23:32	COURT-SAINT-ETIENNE (BE)	4.573	50.633	6.6	2.8		4.0
3275	2009-03-03	14:35:51	FOLKESTONE (UK)	1.170	51.100	5.0	2.8		
3301	2009-03-26	19:42:55	COURT-SAINT-ETIENNE (BE)	4.571	50.632	6.7	2.3		3.0
3337	2009-04-23	17:03:55	MONTFORT (NL)	5.994	51.145	16.1	2.1		
3429	2009-07-16	12:12:08	NORTH OF FRANCE (FR)	3.628	50.181	4.9	2.0	2.0	
3492	2009-07-23	19:55:12	ELSDORF (DE)	6.472	50.933	6.5	2.3		
3501	2009-08-05	21:18:36	ZUTENDAAL (BE)	5.560	50.915	11.2	2.7		4.0
3517	2009-09-10	12:36:22	KOBLENZ (DE)	7.652	50.370	12.2	2.8		
3552	2009-12-26	06:50:13	COURT-SAINT-ETIENNE (BE)	4.575	50.625	5.8	2.5		3.0
3772	2010-02-07	03:09:23	ADENAU (DE)	6.914	50.383	9.0	2.0		
3853	2010-04-11	11:16:17	MAYEN (DE)	7.338	50.343	13.9	2.9		
3886	2010-06-07	00:45:29	MONTFORT (NL)	5.944	51.150	14.8	2.1		
3936	2010-08-27	12:20:04	GENSINGEN (DE)	7.960	49.884	16.3	2.0		
4062	2011-02-14	12:43:12	KOBLENZ (DE)	7.811	50.299	13.3	4.1		5.0
4064	2011-02-14	12:50:43	KOBLENZ (DE)	7.806	50.412	7.0	2.6		3.0
4065	2011-02-14	13:38:00	KOBLENZ (DE)	7.789	50.226		2.3		4.0
4066	2011-02-14	17:23:32	KOBLENZ (DE)	7.775	50.366	5.0	3.3		4.0
4067	2011-02-14	17:30:30	KOBLENZ (DE)	7.723	50.346		2.0		
4068	2011-02-14	19:35:09	KOBLENZ (DE)	7.789	50.348	6.8	2.4		
4069	2011-02-15	12:15:46	KOBLENZ (DE)	7.734	50.373		2.5		
4070	2011-02-16	22:09:33	GERMANY (DE)	8.000	50.090	10.0	3.3		
4327	2011-03-07	20:45:52	ROGNY (FR)	3.812	49.755	18.3	2.3		
4565	2011-08-02	18:37:08	VELDEGEM (BE)	3.146	51.074	6.9	2.4		3.0
4567	2011-08-05	09:29:36	OCHTENDUNG (DE)	7.352	50.331	4.3	2.2		
4580	2011-09-08	19:02:50	GOCH (DE)	6.162	51.668	10.0	4.3		4.0
4588	2011-11-10	00:31:42	NASTAETTEN (DE)	7.843	50.207		2.2		
4594	2011-12-05	18:06:00	SIEVERNICH (DE)	6.671	50.729	11.8	2.0		
4646	2012-02-21	02:34:57	PLAIDT (DE)	7.334	50.337	8.6	2.4		3.0
4656	2012-03-04	04:47:31	AYWAILLE (BE)	5.741	50.465	15.1	2.1		
4681	2012-03-12	19:00:42	KOBERN-GONDORF (DE)	7.399	50.306	10.0	2.4		
4803	2012-11-15	16:40:24	LONNIG (DE)	7.416	50.318	10.3	2.0		
4807	2012-11-22	15:43:15	LONNIG (DE)	7.409	50.304	11.5	2.5		3.0
4816	2012-12-04	09:50:18	STOUMONT (BE)	5.846	50.403	18.8	2.1		
4821	2013-01-05	20:16:53	MECHELEN (NL)	5.943	50.795	18.4	2.3		3.0
4823	2013-01-20	18:26:32	MONTFORT (NL)	5.967	51.140	14.8	2.7		3.0
4832	2013-02-26	09:21:42	IDAR-OBERSTEIN (DE)	7.212	49.709	13.6	2.2		
4843	2013-04-18	03:37:33	PLAIDT (DE)	7.370	50.344	10.0	2.3		3.0
4930	2013-08-15	09:20:29	STOLBERG (DE)	6.310	50.746	10.7	2.4		3.0
5004	2013-11-30	18:09:57	OCHT. / NEUW. BECKEN (DE)	7.367	50.343	13.0	2.4		3.0
5219	2014-11-10	07:43:58	ROERDALEN (NL)	5.961	51.137	15.9	2.0		
5256	2014-12-25	08:52:57	TIEL (NL)	5.452	51.933	17.0	2.7		
5324	2015-05-13	15:23:56	SPA (BE)	5.873	50.462	22.7	2.9		2.0
5327	2015-05-20	19:36:54	NIEDERZIER (DE)	6.456	50.913	8.6	2.0		
5329	2015-05-22	01:52:17	UNITED KINGDOM	1.270	51.360	15.0	4.1		4.0
5428	2015-11-30	05:54:56	HEEZE-LEENDE (NL)	5.544	51.322	10.8	2.1		
5476	2016-04-11	06:15:21	ESCHWEILER (DE)	6.270	50.857	17.9	2.3		
5477	2016-04-11	06:20:11	ESCHWEILER (DE)	6.248	50.843	15.8	2.0		
5531	2016-06-02	08:48:47	ESCHWEILER (DE)	6.310	50.821	19.0	2.0		
5555	2016-09-23	01:10:23	STOCKHEIM (DE)	6.552	50.750	8.1	2.0		
5573	2016-11-04	10:10:33	NOERVENICH (DE)	6.610	50.798	17.2	2.8		
5603	2016-12-22	05:32:17	ST GOAR (DE)	7.688	50.133	10.1	2.7		
5607	2016-12-26	02:20:58	BAD MUNSTEREIFEL (DE)	6.810	50.634	12.3	2.0		
5650	2017-03-14	05:29:06	OCHTENDUNG (DE)	7.442	50.340	5.6	2.5		
5663	2017-03-30	18:40:05	PLAIDT (DE)	7.389	50.398	4.1	2.1		
5735	2017-06-14	23:53:02	KRUFT (DE)	7.186	50.353	10.0	2.6		
5915	2017-09-29	00:36:27	NIEDERSOHREN (DE)	7.348	49.936	16.5	2.3		
5990	2017-11-08	16:40:40	HUERTH (DE)	6.866	50.871	17.3	2.8		
6245	2018-01-22	07:20:35	SAUERTHAL (DE)	7.889	50.109	16.6	2.4		
6250	2018-01-22	07:35:58	SAUERTHAL (DE)	7.900	50.113	16.7	2.3		
6410	2018-03-17	08:08:18	NICKENICH (DE)	7.339	50.379	11.8	2.0		
6505	2018-04-21	11:47:47	DUEREN (DE)	6.531	50.860	16.5	2.7		
6625	2018-05-25	22:43:27	KINROOI (BE)	5.687	51.175	16.6	3.1		
6815	2018-06-21	21:23:48	PLAIDT (DE)	7.372	50.349	13.6	2.1		
6970	2018-07-18	03:40:50	OCHTENDUNG (DE)	7.405	50.366	9.9	2.4		
6995	2018-07-23	08:38:05	HEERLEN (NL)	5.987	50.896	5.6	2.2		
7165	2018-09-13	22:31:18	SPRIMONT (BE)	5.678	50.504	17.6	2.3		
7290	2018-11-17	05:25:01	RAFFELSBRAND (DE)	6.297	50.654	5.8	2.6		
7610	2019-01-11	03:20:15	LINNICH (DE)	6.264	51.004	12.6	2.0		
7815	2019-02-11	04:13:58	KOBERN-GONDORF (DE)	7.429	50.312	10.2	2.5		
7825	2019-02-12	04:21:28	KOBERN-GONDORF (DE)	7.401	50.283	9.6	2.3		
8990	2019-12-10	21:37:50	HAMBACH (DE)	6.439	50.902	5.8	2.2		

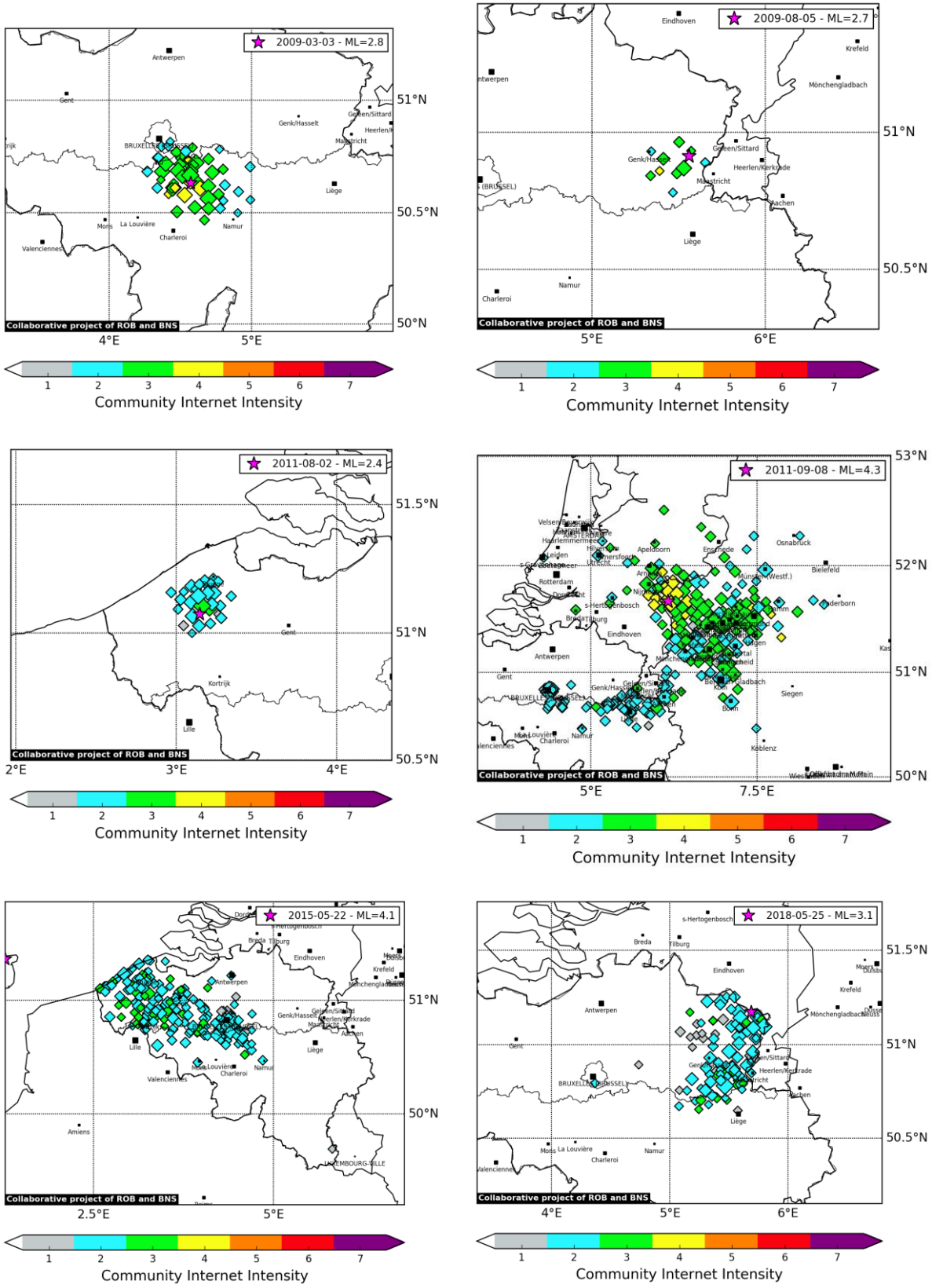

Figure 2: *Macroseismic maps based on the online ROB "Did You Feel It" enquiry of earthquakes felt in Flanders since 2009. Dates are indicated. Diamond-shaped symbols represent average intensity reported in different communes, the size corresponding to the number of replies.*

Catalog processing

Introduction

Compared to the VLA07-4.2 report, processing of the catalog in order to compute seismic activity rates or so-called magnitude-frequency distributions (MFDs) has significantly improved. This includes the following consecutive steps:

- Conversion to a homogeneous magnitude scale: conversion of local magnitude M_L (most instrumental earthquakes) and surface-wave magnitude M_S (most historical earthquakes) using appropriate relations to moment magnitude M_W (used in all modern seismic hazard assessments; see Section 3.3 for details on magnitude scales);
- Declustering or removal of dependent earthquakes (i.e., fore- and aftershocks);
- Completeness analysis, in order to account for changes in the detection threshold with time due to changes in historical archives or changes in instrumental networks (Figure 3).

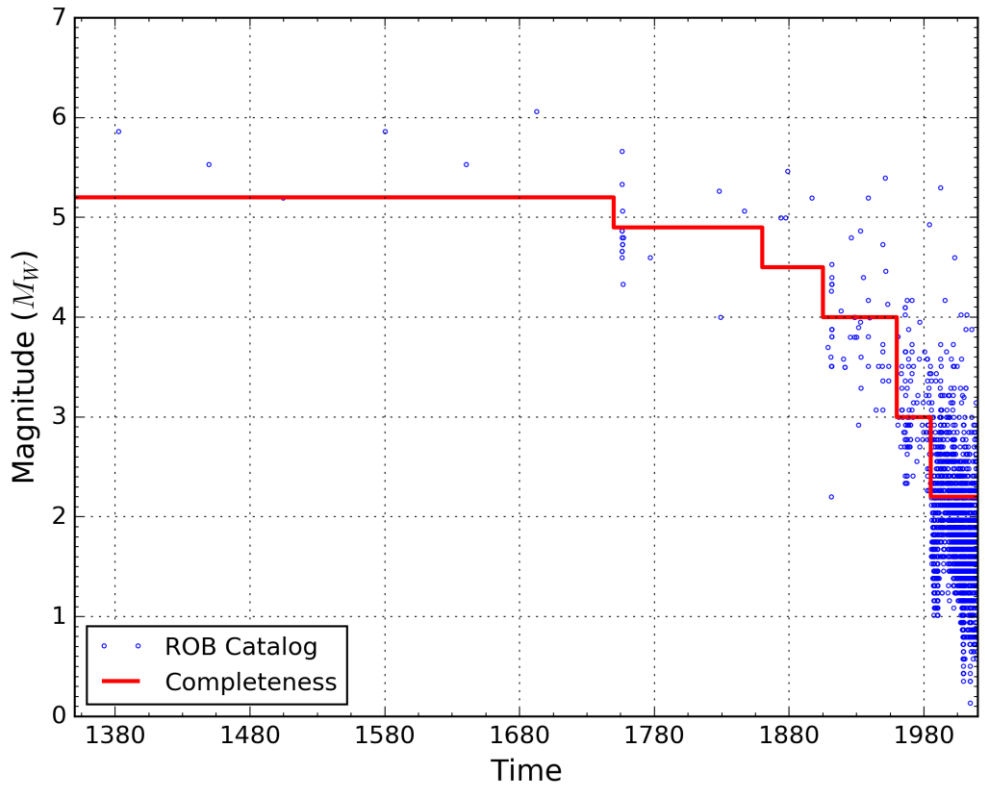

Figure 3: *Plot of magnitude versus time of the ROB seismic catalog, demonstrating a clear improvement (decrease) of the detection threshold with time. The red line corresponds to completeness definition MW_2013a.*

Compared to VLA07-4.2, we now use a different homogeneous magnitude scale (M_W instead of M_S), we decluster the catalog (was not implemented at the time), and we have re-evaluated the completeness using a different method (see below). These steps are briefly described below.

Magnitude scale conversion

Seismic hazard assessments make use of ground-motion models and rupture size scaling relationships that are mostly tied to moment magnitude. For that reason, the MFDs describing the seismic activity should be determined in function of moment magnitude as well. As the ROB catalog contains only few (15) earthquakes for which M_W has been determined, it is necessary to convert the available magnitude types (M_L and M_S) to M_W using relations published in literature. A number of these relations are shown

in Figure 4, together with earthquakes in the ROB catalog for which both magnitude types have been determined. Although the available data are sparse, we can infer that the relations by Geller (1976) and Utsu (2002) provide the best fit to convert M_S to M_W. To convert M_L to M_W, the relations by Reamer & Hinzen (2004) show the best fit for small magnitudes ($M_L < 3.5$), while the relation by Ahorner (1983) fits better for higher magnitudes ($M_L > 4.0$). As the two relations for M_S are nearly identical in the relevant magnitude range, we only retained the Geller (1976) relation in our final selection, whereas for M_L we selected both the relation by Ahorner (1983) and the linear relation of Reamer & Hinzen (2004) (ReamerHinzen2004L in Figure 4). Both are based on data from the neighboring seismic network of Bensberg (Germany), and it has been shown that local magnitudes determined by this network compare well to those in the ROB catalog (Lecocq, 2011). The conversion from M_S is preferred over the one from M_L if both magnitude types are available.

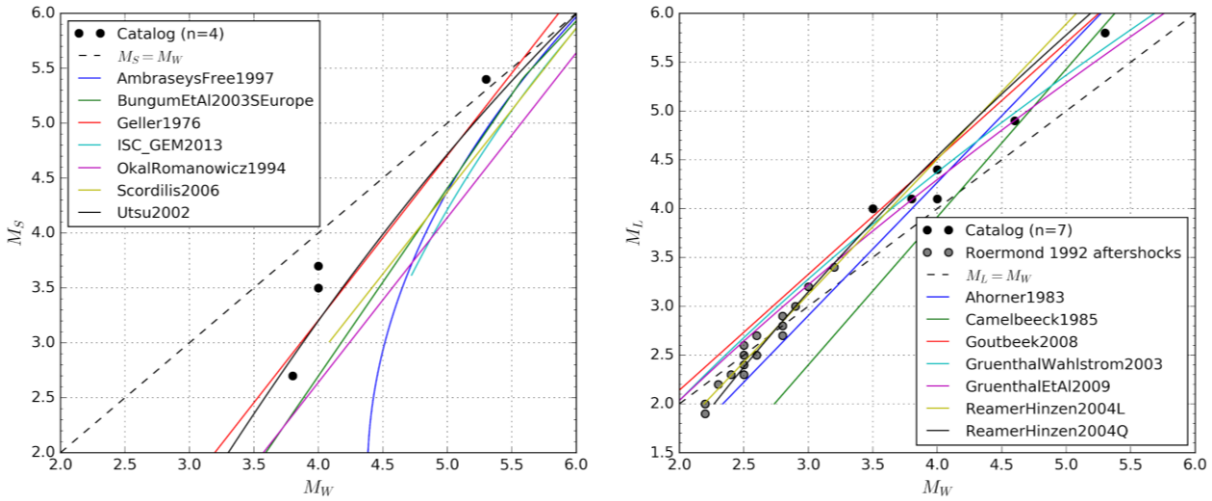

Figure 4: *Comparison of magnitude conversion relations to convert surface-wave magnitude M_S (left) and local magnitude M_L (right) to moment magnitude M_W, together with earthquakes in the ROB catalog that have both magnitude determinations.*

Declustering

To decluster the catalog, we apply the linked-window method, which is an adaptation of the original window method of Gardner & Knopoff (1974). This algorithm makes use of time and distance windows, the size of which depends on the (moment) magnitude of a given earthquake. All earthquakes that are within both the time and distance windows of a particular earthquake are considered to belong to the same cluster. The time and distance windows are then applied in turn to all the earthquakes in the cluster until no more earthquakes can be added to the cluster. The largest earthquake in the cluster that is thus assembled, is considered as the mainshock, and hence an independent earthquake, while all other earthquakes are considered to be dependent events that need to be removed. Note that the duration and extent of a cluster may thus exceed the time and distance windows corresponding to its mainshock. Besides the original window definitions by Gardner & Knopoff (1974), two other window definitions are commonly used in literature: the Uhrhammer window (Uhrhammer, 1986), which is based on data from Central California, and the Grünthal window (Grünthal *et al.*, 2009), which is based on European data and includes historical earthquakes. A comparison of these three window definitions is shown in Figure 5.

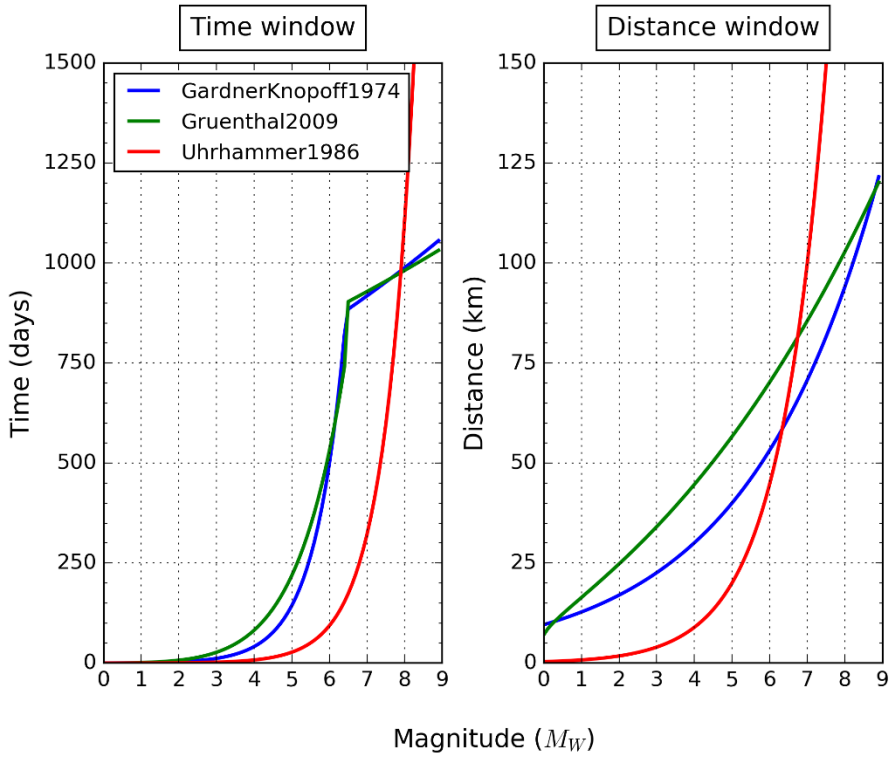

Figure 5: *Different time and distance window definitions for declustering.*

Table 2 shows the results obtained with the three different declustering windows. It is clear that the Uhrhammer window identifies much less clustered events than the other windows. The differences between the Gardner-Knopoff and Grünthal windows are smaller, but the latter is the most restrictive, resulting in the removal of 48% of the earthquakes in the original catalog. Based on manual analysis of the identified clusters, we consider that the Uhrhammer window misses many events that appear clustered to us, and hence is not appropriate for our catalog, probably because of the lower seismic activity in our region compared to plate boundaries. The other two windows seem equally appropriate to us.

Table 2: *Declustering results using different window definitions for the ROB catalog (2270 events)*

Window	No. of clusters identified	Max. cluster length	No. of clustered events (incl. mainshocks)	No. of independent events
Gardner & Knopoff (1974)	272	57	1148	1394
Uhrhammer (1986)	169	48	573	1866
Grünthal (2009)	284	118	1373	1181

The declustering result can also be evaluated by comparing with the theoretical distribution for a stationary Poisson process. This can be achieved by dividing the completeness filtered and declustered catalog in intervals of the same duration T, count the number of earthquakes with magnitude above a lower bound in each interval, and compare the distribution of the number of intervals with different number of events per interval with that predicted by the Poisson distribution for the same time interval T. This is shown in Figure 6 for two lower magnitudes M ≥ 2.5 and 3.5. The catalog declustered with the Uhrhammer window clearly shows a poorer match than the other two windows, while the Grünthal window shows a slightly better match than the Gardner-Knopoff window.

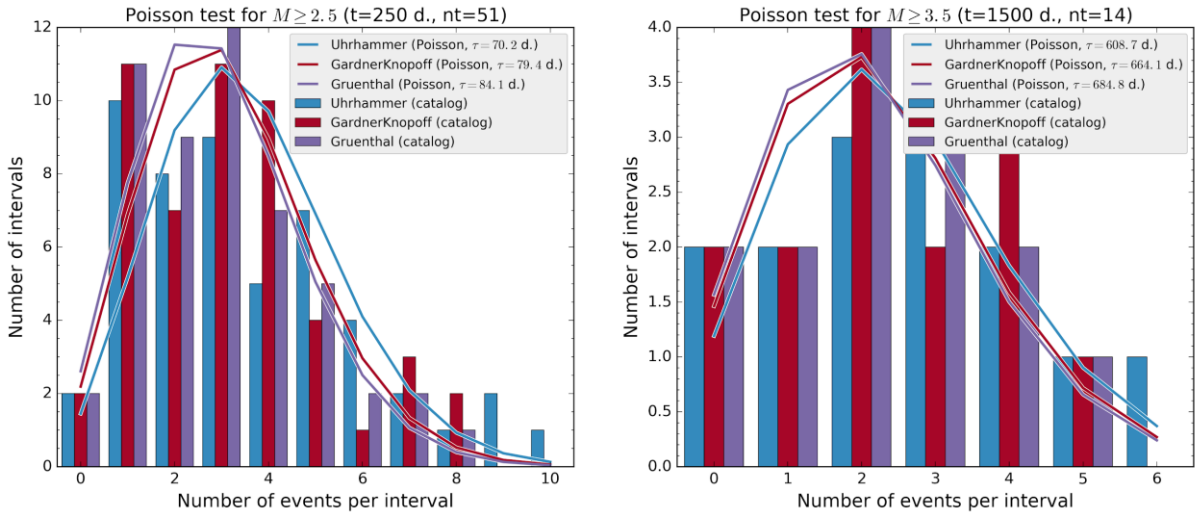

Figure 6: *Comparison of the distribution of the number of intervals of the same duration and the number of events with M≥M_{min} in each with that predicted by the Poisson distribution for the same time interval. Left: M_{min}=2.5, duration=250 days; Right: M_{min}=3.5, duration=1500 days*

Completeness evaluation

We evaluated the completeness of the ROB catalog using the CUVI (cumulative visual) method of Mulargia *et al. (*1987). In this method, plots are made of the number of earthquakes larger than or equal to a given magnitude versus time for successive, closely spaced, magnitudes. Changes in completeness are obvious as changes in slope (increasing towards present) for several subsequent lower magnitudes, resulting in a diverging set of curves. It is important that the catalog is declustered first, because aftershock sequences and swarms may also cause changes in slope.

In our plots, clear changes in completeness can be observed at or around the following years: 1996, 1985, 1960, 1905, 1860, and 1750. These years correspond to changes in the instrumental network or in the historical record:

- 1750 more or less corresponds to the time of the great Lisbon earthquake (7.7 ≤ M_W ≤ 8.5; still debated) and tsunami in 1755, which sparked an increasing awareness of earthquakes in Europe. Around the same time (1755 – 1757), a seismic crisis occurred in the German part of the Lower Rhine Graben, culminating in the M_S=5.7 Düren earthquake in 1756.
- The cause of the change in completeness around 1860 is not so clear. Seismographs were not yet operational at this time, so it must reflect a change in the historical record. Possible explanations are the development of the written press in the second half of the 19th century, and the increased interest of German historians in earthquakes from this time onward.
- 1905 corresponds to the time when the first seismograph in Uccle (installed in 1898) was handed over to the ROB, and continuous monitoring began.
- 1960 more or less corresponds with the emplacement of denser national networks in neighboring countries (mainly France and Germany).
- 1985 marks the deployment of the modern seismic network in Belgium following the M_S=4.6 Liège earthquake in 1983. At this time, the number of seismic stations strongly increased, and digital recording began.
- 1996 coincides with the start of the Eifel Plume project (Ritter *et al.*, 2001), in which the ROB participated by temporarily deploying mobile stations, and which resulted in an increased focus on identifying small local events.

- A more recent, smaller change can also be inferred around 2007, possibly related to the introduction of automatic detection systems at the ROB or perhaps to an increasing focus on small events raised by the Walloon Brabant swarm (2008 – 2009).

We then evaluated the completeness magnitude corresponding to each period of completeness from the plots as the lowest magnitude that shows a change (increase) in slope at that year, but does not show any further increase in slope beyond this year (towards more recent times). This is shown in Figure 7. Depending on the M_L-to-M_W conversion used in the first step, we defined two slightly different sets of completeness magnitudes (Table 3).

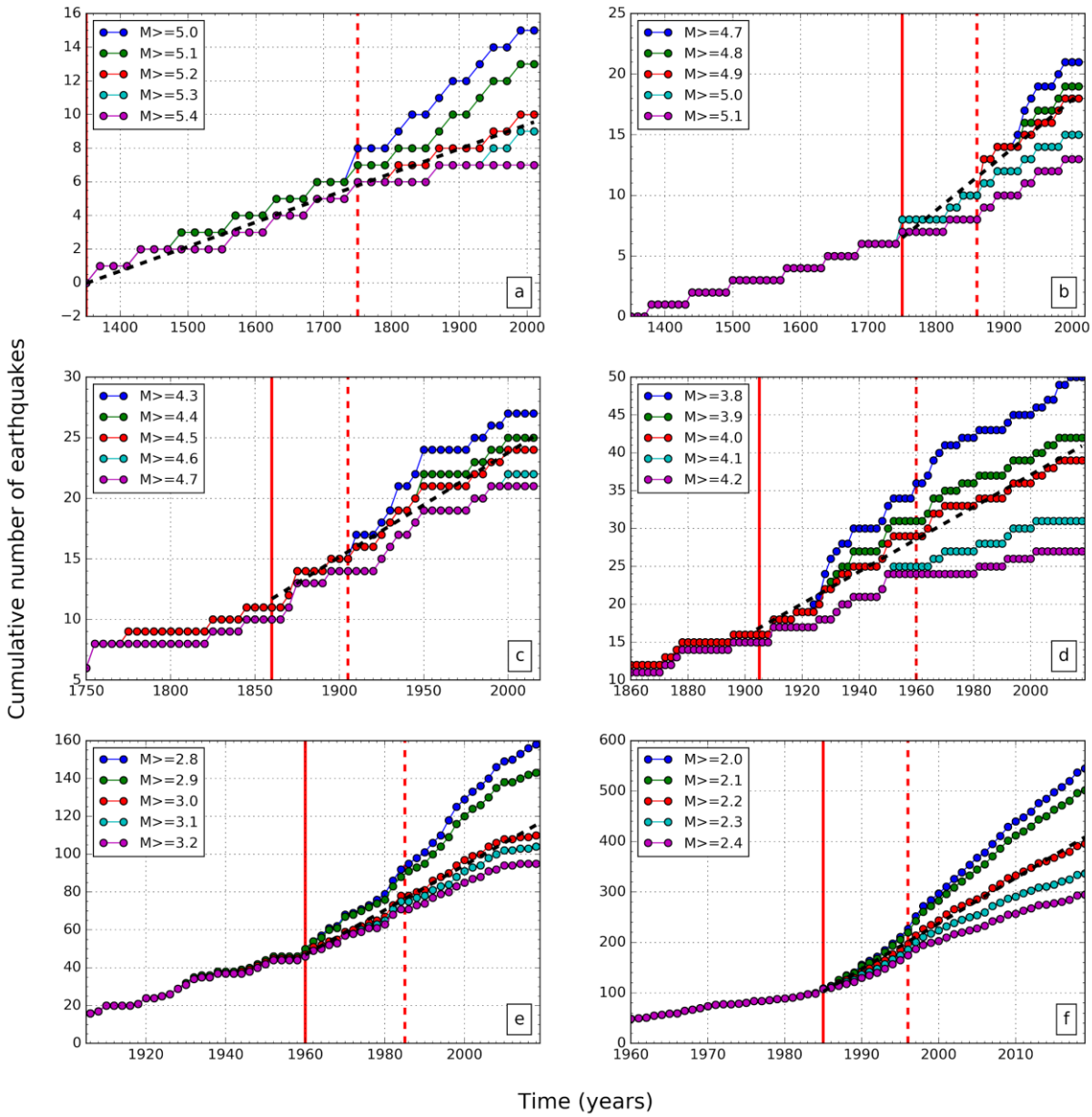

***Figure 7**: Evaluation of completeness MW_2013a using the CUVI method (Mulargia et al., 1987) applied to the catalog declustered with the Grünthal (2009) window. Panels correspond to different completeness years: a) 1350; b) 1760; c) 1860; d) 1905; e) 1960; f) 1985. Full red vertical line correspond to the evaluated year of completeness, dashed red vertical line to the subsequent year of completeness.*

Table 3: *Completeness results for the ROB catalog. MSC: magnitude scale conversion.*

Completeness year	Completeness magnitude	
	MW_2013a (Ahorner MSC)	MW_2013_b (Reamer-Hinzen MSC)
1996	1.8	1.7
1985	2.2	2.0
1960	3.0	2.9
1905	4.0	3.9
1860	4.5	4.5
1760	4.9	4.9
1350	5.2	5.2

An interesting side observation of this completeness evaluation is that the curves in Figure 7e show a clear decrease of M2.8 – M3.2 earthquakes in the last decade, suggesting that a deficit in this magnitude range has accrued since ~2010.

Magnitude-frequency distribution

After application of the completeness filter, the (annual) frequency of different magnitudes can be computed simply by counting the number of earthquakes with a given magnitude and dividing this number by the period of completeness for that magnitude. The result is the magnitude-frequency distribution. Gutenberg & Richter (1944) discovered that, if one considers a sufficiently large region, there exists a log-linear relation between the number (or frequency) of earthquakes and their magnitude . This relation is often referred to as the Gutenberg-Richter law:

$$logN(m > M) = a - bM$$

This is the equation of a straight line in a log-linear graph (Figure 8) with intercept a and slope$b$. Parameter a describes how active the region is, and parameter b determines the ratio of larger versus smaller earthquakes; usually, the b-value is around 1, which implies that the number of earthquakes roughly decreases by a factor of 10 when the magnitude increases by one unit.

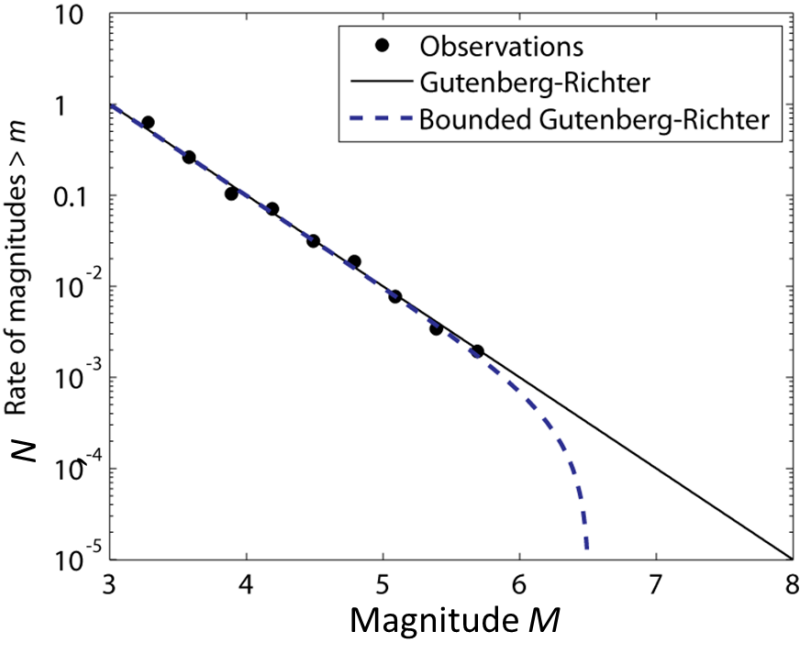

Figure 8: *Graph showing typical Gutenberg-Richter relation*

The Gutenberg-Richter relation applies both to incremental frequencies (number of earthquakes within a magnitude interval) and to cumulative frequencies (number of earthquakes with magnitude above a given value). In the latter case, as there is an upper bound corresponding to the maximum magnitude (Mmax), the relation changes from a straight line to an exponential taper as it approaches Mmax.

We construct the cumulative magnitude-frequency distribution for a range of magnitudes between the lowest completeness magnitude and the highest observed magnitude, and with a spacing of 0.1 units. The a- and b-values of the Gutenberg-Richter relation can then be estimated by fitting a truncated Gutenberg-Richter law using the method of Weichert (1980), which is based on maximum-likelihood estimation. This method is preferred over simple least-squares regression because it takes into account unequal observation periods for different magnitudes, as well as the exponential taper towards Mmax. It is also sensitive to empty magnitude bins (e.g., between the maximum observed magnitude and the assumed Mmax), but not very strongly (Musson, 2011). The Weichert method is also very sensitive to the minimum magnitude. We used a minimum magnitude of 2.0 or 2.2 (thus excluding the most recent completeness period since 1996, see Table 3), depending on the completeness used, and a maximum magnitude of 6.5. Figure 9 shows the results obtained using two different completeness criteria and two different declustering windows. The fit appears best for the combination of the MW_2013a completeness and the Gardner-Knopoff declustering window (panel b).

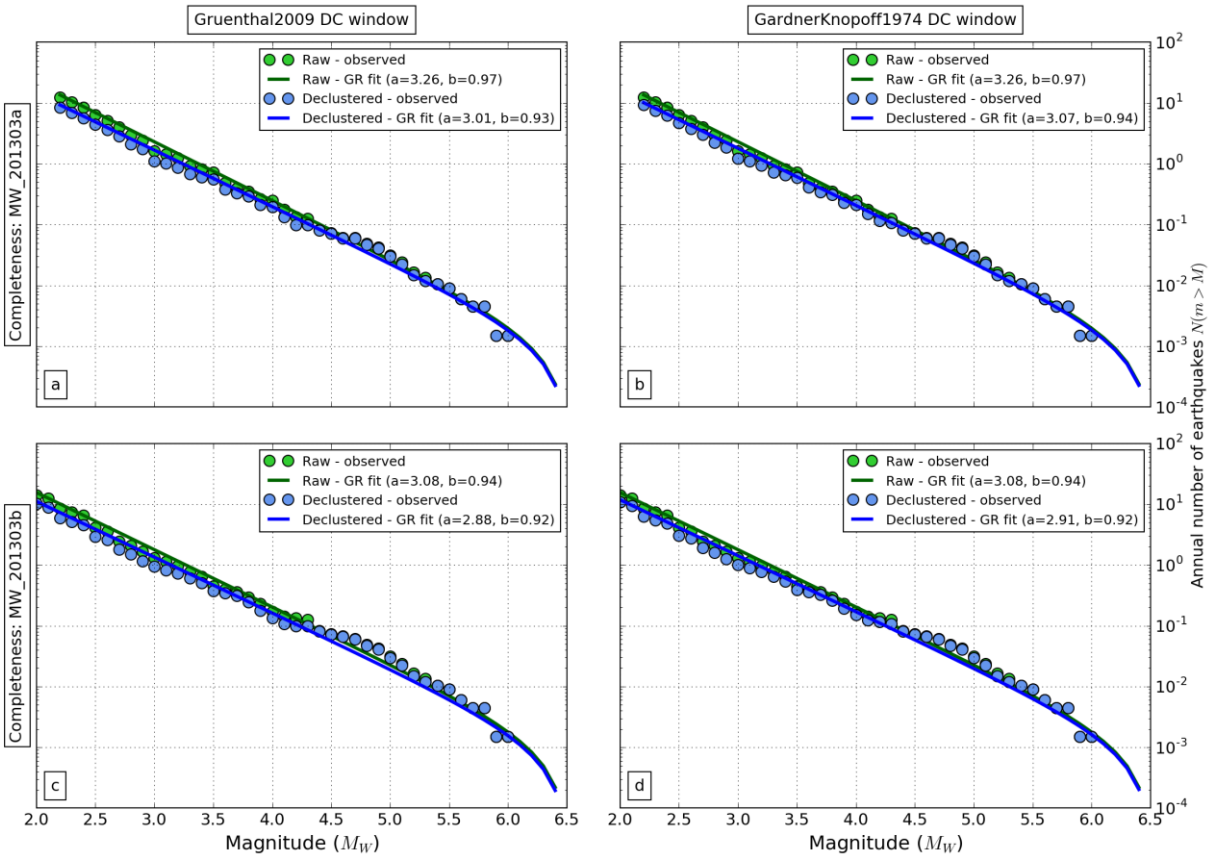

Figure 9: *Magnitude-frequency distributions and corresponding Gutenberg-Richter fits for the ROB catalog, obtained using two different completeness criteria (MW_2013a and MW_2013b) and two different declustering windows (Grünthal and Gardner-Knopoff). In each panel, filled circles correspond to observed exceedance frequencies for different magnitudes with a spacing of 0.1, and full lines indicate the Gutenberg-Richter fit based on the observed distribution. Observed distributions and fits are shown for the catalog before (green) and after (blue) declustering. The difference are evident by the different a- and b-values in the legend.*

Note that these MFDs represent the activity in the entire region covered by the ROB catalog. We can also determine the MFD for the region of Flanders only, in order to compute the frequency of earthquakes with different magnitudes that could affect the territory. In this case, however, we want to take into account that the distance over which the effects of an earthquake manifest themselves increases with magnitude. For example, a large earthquake with epicenter just outside the border would probably also cause damage in Flanders. This can be accounted for by including earthquakes at a distance from the border that increases with magnitude. There is no unique solution to this problem; the option we took was to use the distance function from the declustering window of Grünthal *et al. (*2009), as illustrated in Figure 10. The resulting observed MFD and Gutenberg-Richter fit are shown in Figure 11. Compared to the MFD for the entire ROB catalog (Figure 9), the b-value is noticeably lower (i.e., the slope is flatter). This is probably due to a combination of the lower number of earthquakes used, and of the increasing area with magnitude. Based on this MFD, we can compute the frequency of earthquakes with a given lower magnitude affecting the territory of Flanders. These frequencies (and their uncertainties) are listed for different lower magnitudes in Table 4. It should be noted that these values are only valid for moment magnitude.

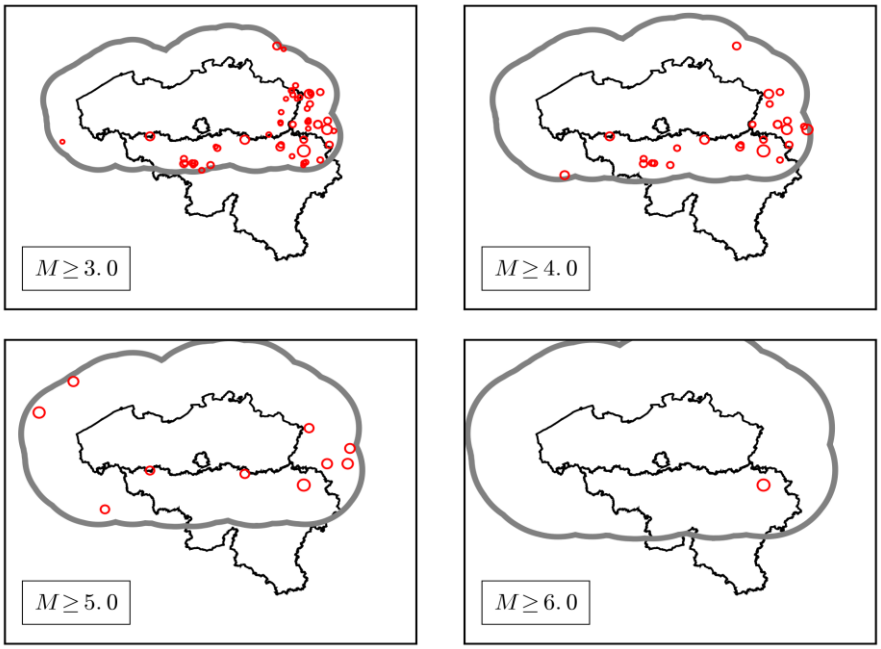

Figure 10: *Illustration of increasing selection distance with magnitude, used to compute the magnitude-frequency distribution for Flanders only.*

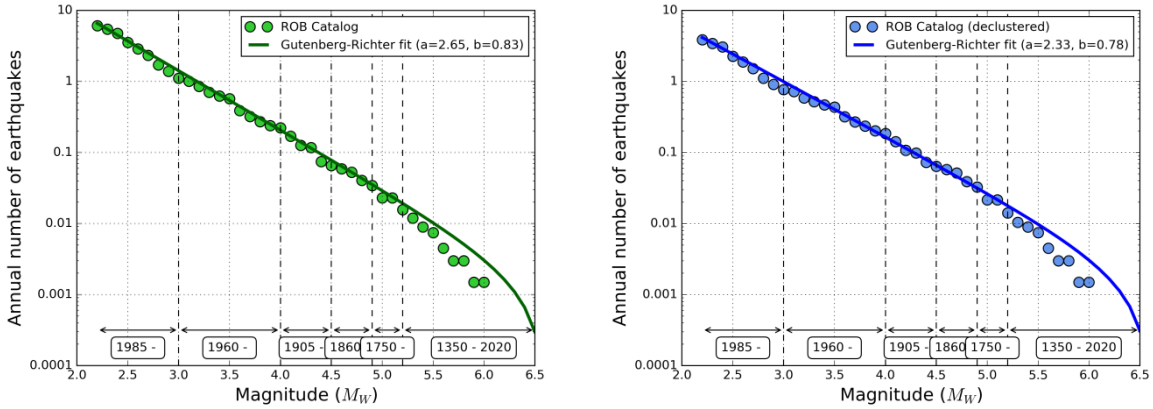

Figure 11*: Magnitude-frequency distributions computed for the region of Flanders only. Left: without declustering; Right: after declustering (Gardner-Knopoff window).*

Table 4: *Frequency (including uncertainty) of earthquakes with given lower magnitudes (M_W) affecting the territory of Flanders*

Lower magnitude	Frequency (no declustering)	Frequency (after declustering)
$M_W \geq 2.2$	6.0 – 7.2 per year	3.8 – 4.6 per year
$M_W \geq 3.0$	1.2 – 1.6 per year	0.8 – 1.2 per year
$M_W \geq 4.0$	1 every 3.9 – 6.1 years	1 every 4.8 – 7.8 years
$M_W \geq 5.0$	1 every 25.9 – 46.2 years	1 every 27.9 – 52.6 years
$M_W \geq 6.0$	1 every 232.6 – 465.7 years	1 every 224.7 – 480.6 years

2.3 FULL INSTRUMENTAL CATALOG SINCE 1910

This catalog contains all seismic events that have been recorded by the instruments of the Belgian seismic network. The start year of this catalog is 1910, the year when continuous recording started. The geographic extent is the same as that of the catalog of tectonic earthquakes. Besides known earthquakes, this catalog also contains other types of events, which are listed in Table 5.

Table 5: *Event types contained in the full instrumental seismic catalog*

Code	Event type	Number of events
ke	earthquake	2242
se	suspected earthquake	11
ki	induced event	148
si	suspected induced event	68
qb	quarry blast	486
sqb	suspected quarry blast	4
km	mine explosion	442
sm	suspected mine explosion	35
kr	rockburst	2
sr	suspected rockburst	1
cb	controlled explosion	39
scb	suspected controlled explosion	1
kx	experimental explosion	1
sx	suspected experimental explosion	1

Suspected earthquakes are seismic events that look like earthquakes, occur in areas without previous seismic activity, but cannot be linked to quarries or mines, and are too small to locate precisely and/or to unambiguously classify as earthquakes. An interesting suspected earthquake is the M_L=1.8 event on 01/08/2001 north of Loenhout, which may perhaps be related to gas storage operations in this region. Induced events mainly concern mining-related earthquakes in the Ruhr district north of Duisburg and in the Saarland, both in Germany, and since 2016 the geothermally induced earthquakes at Balmatt in Flanders. Quarry blasts and mine explosions correspond to explosions in open quarries and underground mines, respectively. The majority of these events is located in Wallonia. Rockbursts are spontaneous, violent failures of rock that occur under high stress in underground mines. The number of such events in our catalog is limited. Controlled explosions comprise intentional explosions of old world war ammunition and explosives, usually at sea, as well as explosions related to large infrastructure works (e.g., the M_L=1.7 explosion to break down the old quay walls in Antwerp on 01/07/2018). Experimental explosions are controlled explosions intended for seismic tests. Finally, suspected events indicate events that look like the event type but not sufficient data is available to link it to the event as such.

A map of the ROB instrumental catalog is shown in Figure 12. It should be noted, however, that the classification of event types is not very rigid (e.g., many controlled explosions at sea are classified as mine explosions). In addition, the coverage of non-tectonic events in the catalog is very heterogeneous

through time: it is not possible to establish their completeness, and the catalog should clearly not be used to infer changes in the rate of occurrence of non-tectonic seismic events! Finally, Figure 13 shows the macroseismic map (similar to those for tectonic earthquakes in Fig. 2) based on our DYFI enquiry for the largest induced earthquake at Balmatt, which was felt by the local population.

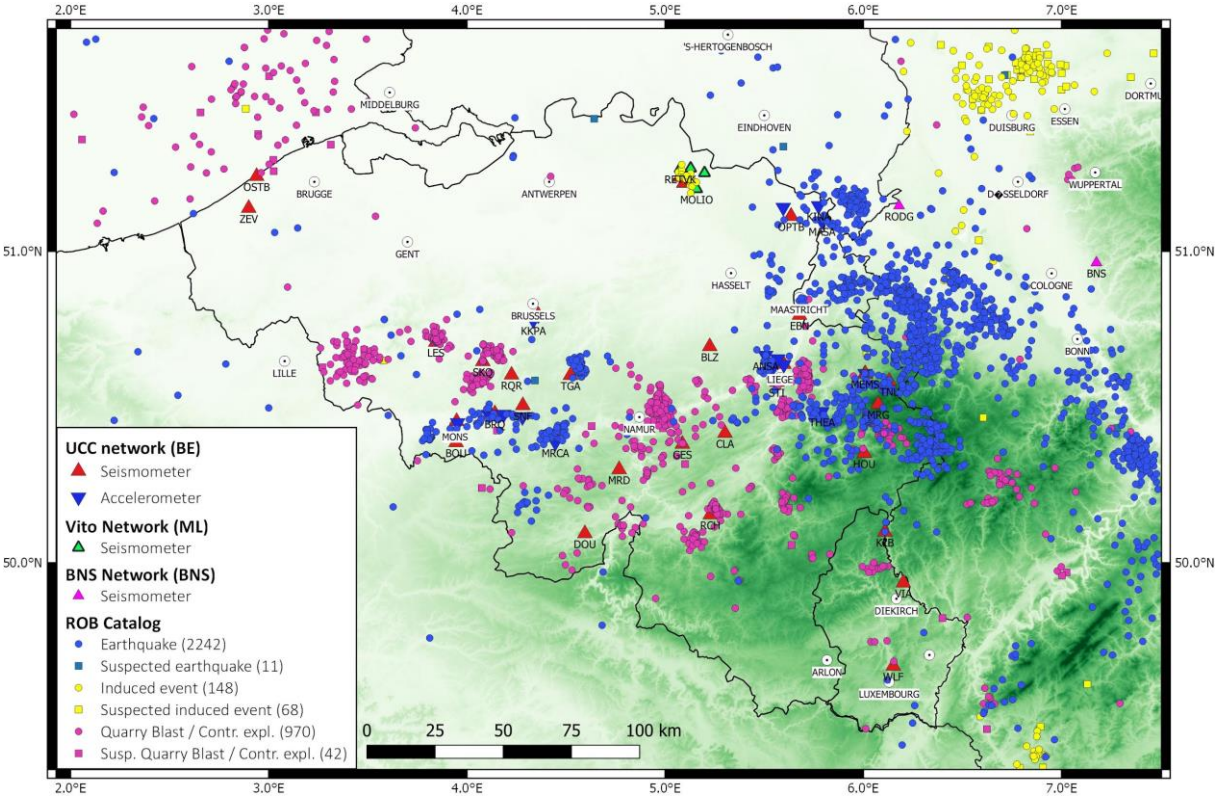

Figure 12: *Map of full instrumental ROB catalog (01-01-1910 to 31-10-2019). For simplicity, the (suspected) Quarry Blast / Contr. Explosion layer contains the (suspected) controlled explosions, experimental explosions, mine explosions, rockburst and quarry blasts event types.*

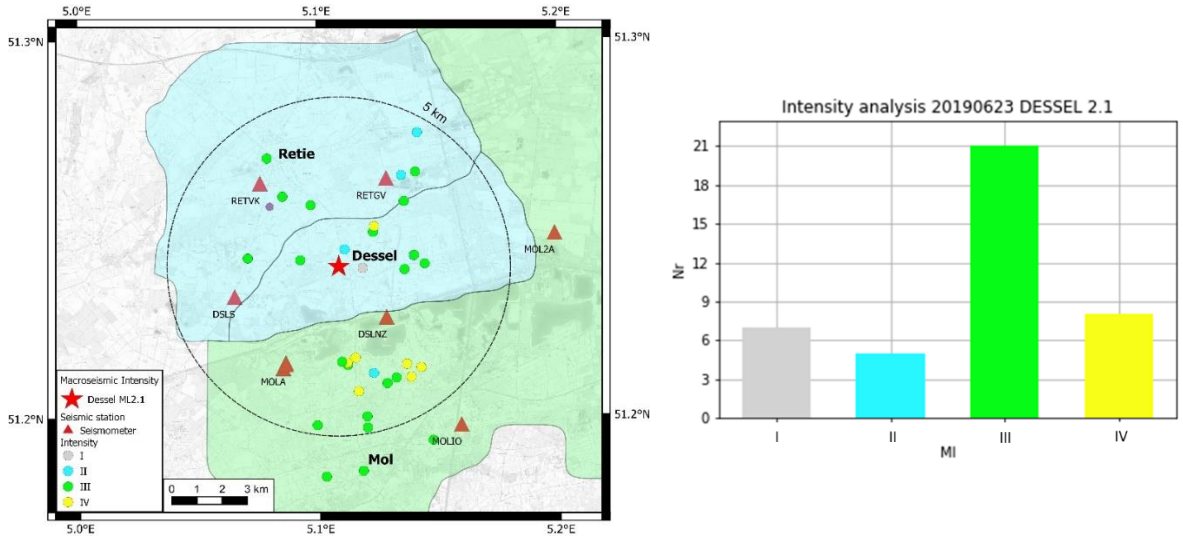

Figure 13: Left) *Macroseismic map of the M_L =2.1 induced earthquake on 23/06/2019. Macroseismic intensity of three communes (Retie, Mol, Dessel) could be calculated. Points show individual intensity points located after geocoding addresses.* ***Right)*** *Histogram of intensity data received after the 23/06/2019 event.*

2.4 List of induced earthquakes at Balmatt since 2016

VITO made the first injection tests in the MOL-GT2 borehole in September 2016. At that time the only monitoring equipment available were those owned by ONDRAF-NIRAS and operated by the Royal Observatory of Belgium in Mol and Dessel. After visually identifying the main induced earthquakes, we used the template matching data mining technique (e.g., Chamberlain *et al.*, 2017). This technique works by sliding a template (reference event) over continuous seismic data and evaluating a score, typically a cross-correlation value. When this score surpasses a predefined threshold, a detection is made. The detections are then checked visually to eliminate false detections. In Lecocq *et al. (*2017), we reported that more than 350 events occurred during and after the injection tests. Those included very small events for which only few, but certain features could be identified on the waveforms recorded by Dessel borehole and Mol Tunnel stations.

For this report, we define the "template" as the 18 December 2018 (12h40m04s UTC, M_L = 1.2; Figure 14) for which the Dessel borehole and surface stations (DSLB, DSLS) worked at the same time as the Mol Tunnel station (MOLT). This way, the template could be used even when one of the stations failed, which is the case for DSLB during some period of time between 2016 and 2020. After defining the template, the algorithm was run on all continuous seismic data of the three stations DSLS, DSLB and MOLT.

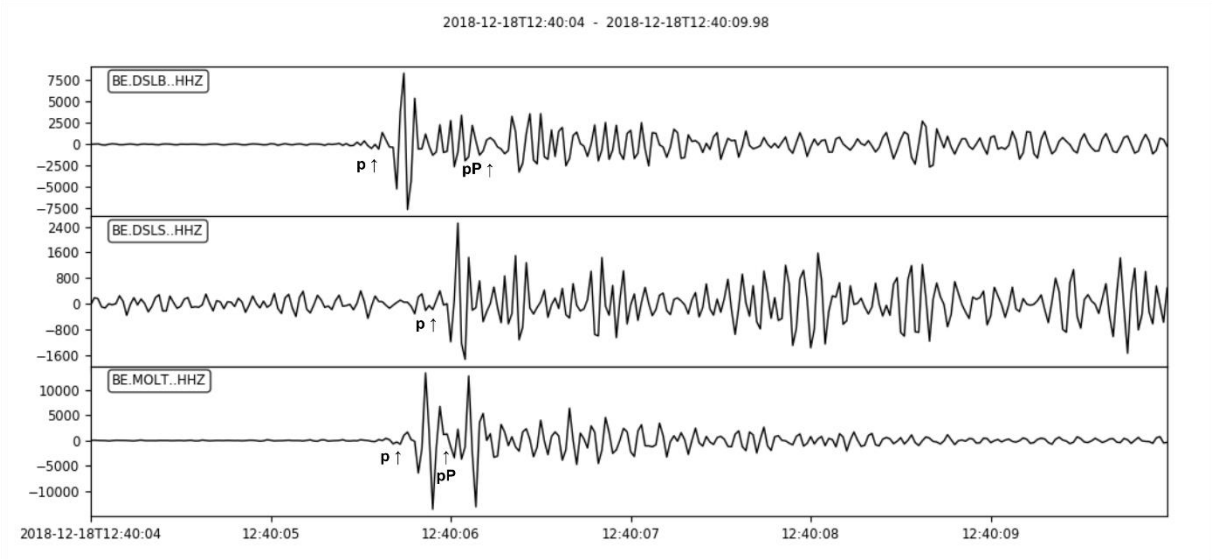

Figure 14: *Template used for the Template Matching technique, exhibiting clear signatures of wave propagation: First arrival at DSLB, then MOLT and finally DSLS. The double peak on MOLT and DSLB show the arrivals of an up-going P-wave (p) followed by the surface-reflected down-going P-wave (pP), with a longer time between the two peaks for DSLB, as the station is located deeper than MOLT.*

After a first pass, the algorithm identified 3392 detections between 1 January 2016 and 31 December 2019 on at least two (note that DSLB was sometimes out of service) of the three stations (Figure 15). As stated above, not all detections are events. To provide a template matching detection list (see Annex A: Template matching event list), the waveforms of each detection have been exported and visually controlled. Only the clear, unambiguous waveforms are kept at this stage. The others, although maybe real and very small events, are discarded. The visual inspection has kept 171 events, ~5% (Figure 16). This number is smaller than in the Lecocq *et al. (*2017) report for the 2016 events because of a voluntarily high level of confidence required to keep only unambiguous events, which eliminates small and less clear events.

The induced seismic activity occurs in bursts for which some periods are known, like the September 2016 “injection tests” or the December 2018 “start of operations”. The other bursts of activity start around 16 January 2019, 17 February 2019, 20 May 2019 and 13 June 2019. Those sequences have to be linked to VITO Balmatt operations that we are not completely aware of (dates of start/end/changes of operations).

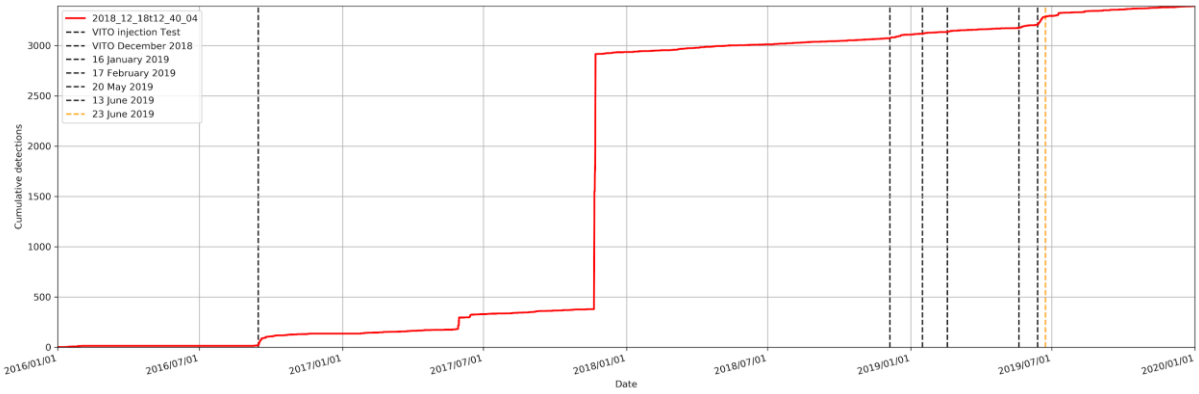

Figure 15: *Cumulative number of raw detections by the Template Matching algorithm applied on stations DSLB, DSLS and MOLT.*

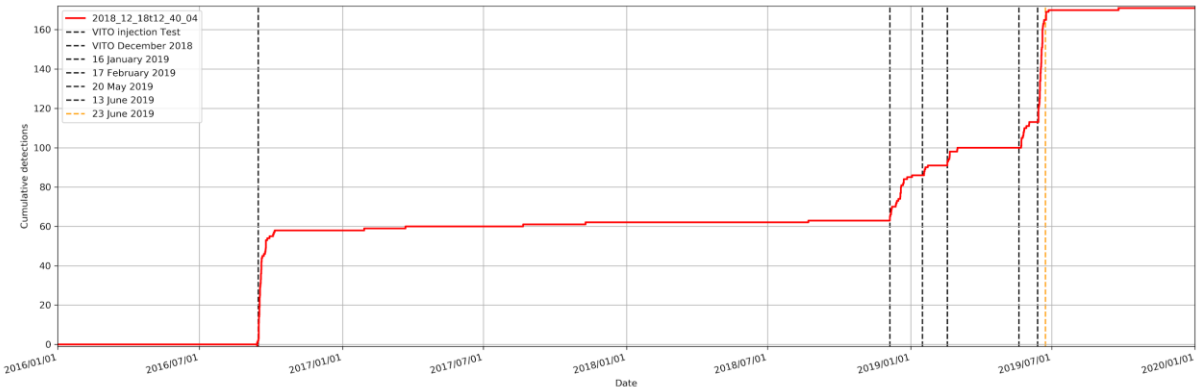

Figure 16: *Cumulative number of events, identified by the Template Matching algorithm and visually checked.*

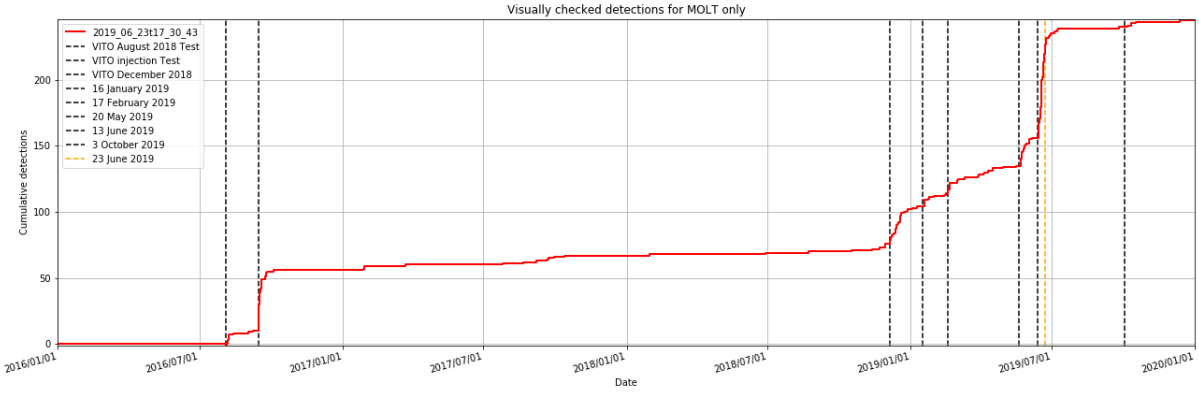

Figure 17: *Cumulative number of events, identified by the Template Matching algorithm on the MOLT (Mol Tunnel) station only and visually checked.*

Repeating the template matching computation for MOLT only, including its 3 components (vertical, north-south and east-west), between January 2016 and December 2019, leads to 5255 detections by the algorithm. 2000 false detections occurred on 4 days and can be linked to higher anthropogenic disturbances. The remaining 3255 detections have been visually checked and the most similar

detections were marked as true events. The final number of detected events on MOLT is 245 events (Figure 17). Interestingly, using MOLT only, we are able to see the activity triggered by the first borehole tests done by VITO in August 2016.

The template matching detection list (Annex A) contains 91 out of the 221 identified in the catalog provided by VITO on their seismic monitoring network website. A first reason for the lower number of detections is that seven events occur less than 30 seconds after one another. Only the first event was detected. The succeeding events were not detected because we defined in our algorithm a minimum separation time of 30 s to save computation time and avoid double-triggers for different seismic phases of the same earthquake. A second reason for the lower number of detections is that we manually checked events on a single station, which can sometimes have a higher noise level (MOLT is in the HADES tunnel), while the other stations from the VITO network, used all at once in the detection system run by DMT, could detect smaller events. Improvements could be made to the detection algorithm to make it more sensitive to small changes in the event locations and sources, which alter the recorded waveforms and lower the correlation coefficient with the template.

3. SEISMIC NETWORKS

3.1 EARTHQUAKE DETECTION CAPABILITY IN BELGIUM

The seismic instruments installed and operated by the Royal Observatory of Belgium are sensitive instruments capable of measuring very small ground motions, down to the nanometer. The quality of the records for a specific earthquake are dependent on the strength of the event, that is, its magnitude, the distance to the station, the anelastic attenuation of the Earth's crust (see Glossary for definition) and the local noise conditions. Two identical events, i.e., co-located with the same magnitude and mechanism, can have a very different signal to noise ratio (SNR) on the records if they occur at night or during the day, when the anthropogenic noise is the largest.

To investigate the earthquake detection capability in Belgium, we first computed the noise levels for all permanent ROB stations. The root mean square (RMS) of the signals, i.e., the mean noise level, was computed in one hour windows. The RMS defined two sets of noise levels which are different depending on the local hour of the day (day: from 4h to 21 h and night: from 21h to 4 h). If two stations are co-located (one surface and one borehole, for example), the station with the lowest noise level is kept for the computation. The noise levels exhibit large differences, up to a factor of 8, between the night and the day (Figure 18) in the frequency band of interest for the earthquakes (4-14 Hz).

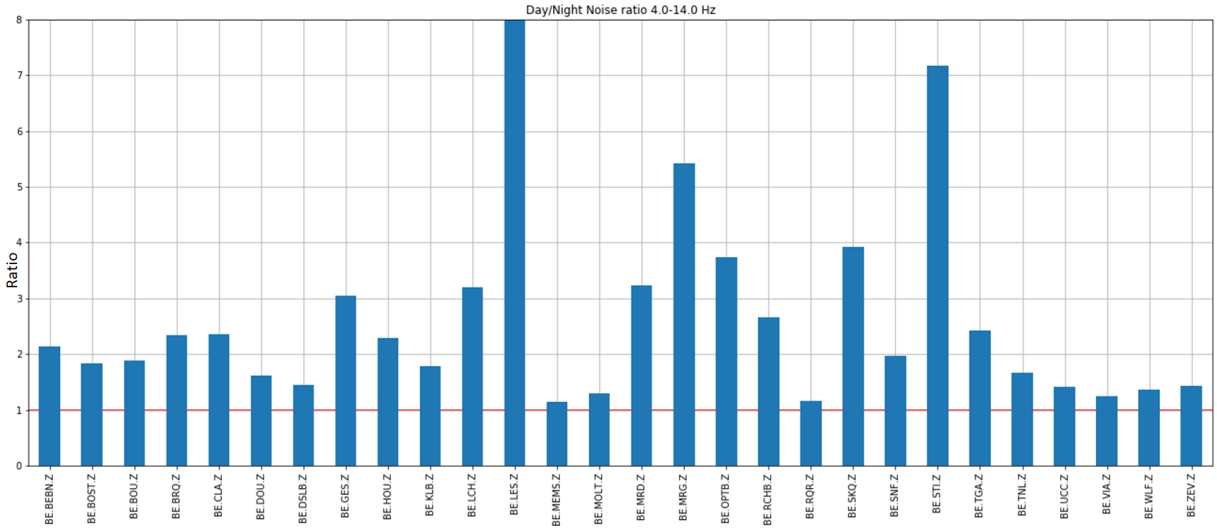

Figure 18: *Noise level ratio between day and night for each permanent ROB seismic station. UCC = UCCB.*

The RMS is input in the SENSI software (Orazi *et al.*, 2013) which simulates the ground motion generated by 10-km deep sources located on a regular grid. Table 6 shows the source parameters that are defined to match realistic values known for the Belgian crust:

Table 6: *Source parameters representative of the Belgian crust used in the SENSI software*

stress drop (bar)	100
medium density (g/cm3)	2.6
S-wave average velocity (km/s)	3.6
anelastic attenuation factor	200
earthquake depth (km asl)	-10

SENSI works by computing synthetic source time functions for different magnitudes and comparing the attenuated ground motion with the noise level of each seismic station. If the SNR is larger than 1.2 (20% larger than the noise level), the station is marked as "able" to measure the event. For each source location on the grid, the minimum magnitude is defined from the smallest magnitude event that either one (for "detection") or four (for "location") stations are able to measure. SENSI simulates the P-wave only and therefore only uses vertical ground motions and noise levels.

Disclaimers

The simulations are theoretical and the maps presented in the following sections must not be taken as absolute values but rather as a guide for estimating the relative capacity of the Belgian seismic network for detecting and locating an earthquake in different zones of the country. The absolute values could most probably vary by ± 0.2 magnitude points. The simulations are computed using the stations of the permanent seismic network as of January 2019, without the inclusion of stations operated by neighboring countries. For the ROB automatic detection (see section below), four stations in The Netherlands (Oploo-OPLO, Valkenburg-VKB, Heimansgroeve-HGN and Herkenbosch-HRKB), two in Germany (Ahrweiler-AHRW and Bochum-BUG), two in Luxemburg (Wilwerwiltz-WILW and Gaichel-KIND) and one in the United Kingdom (Elham-ELSH) are real time stations closest to the Belgian borders used too (Figure 19). Adding those to the simulations has no significant impact on the detection maps produced.

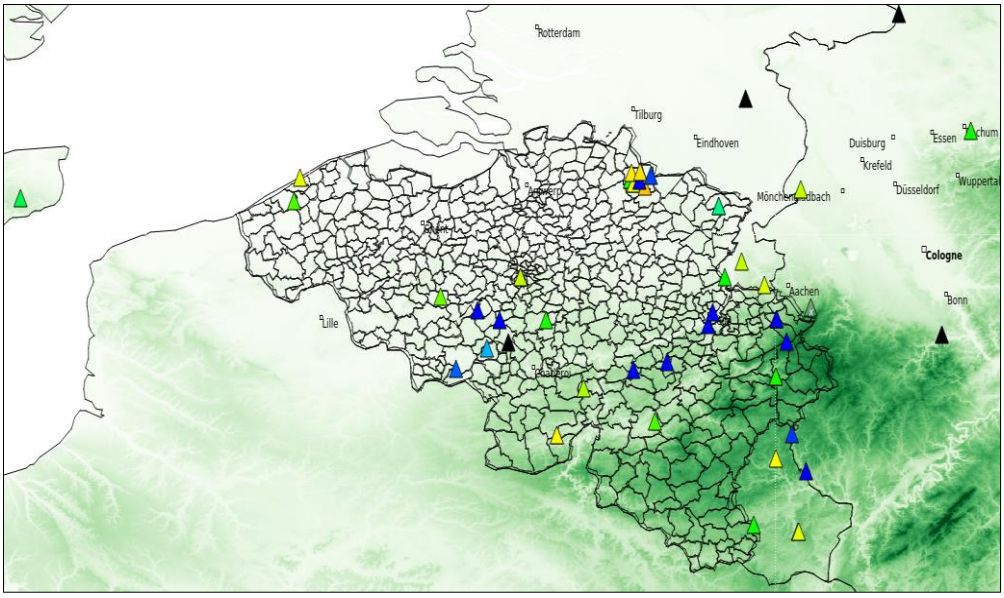

Figure 19: *Snapshot of the real-time earthquake detection system "SeisComP3" running at the ROB. Triangles indicate seismic stations used for real-time monitoring. Triangles are coloured as a function of the station noise level in real time.*

Location

Theoretically, four stations are required to solve the four unknowns of the earthquake location problem properly: its hypocenter (x, y, z) and its origin time (t_0). The minimum magnitude of an event measurable on four stations depends on their noise level. For the majority of the station locations in Belgium, the minimum magnitude is 0.2 points higher during the day (Figure 20) than during the night (Figure 21). Adding or removing one station can have a strong influence on the location capability. First, the earthquake detection capability for the current status of the Belgian seismic network is computed. Second, we simulate the detection map with the addition of one future borehole station installed in the Merksplas borehole (KB160) with noise parameters set as similar to DSLB (Figure 22).

Adding this station would result in lowering the minimum magnitude by 0.2 points in most of the province of Antwerp.

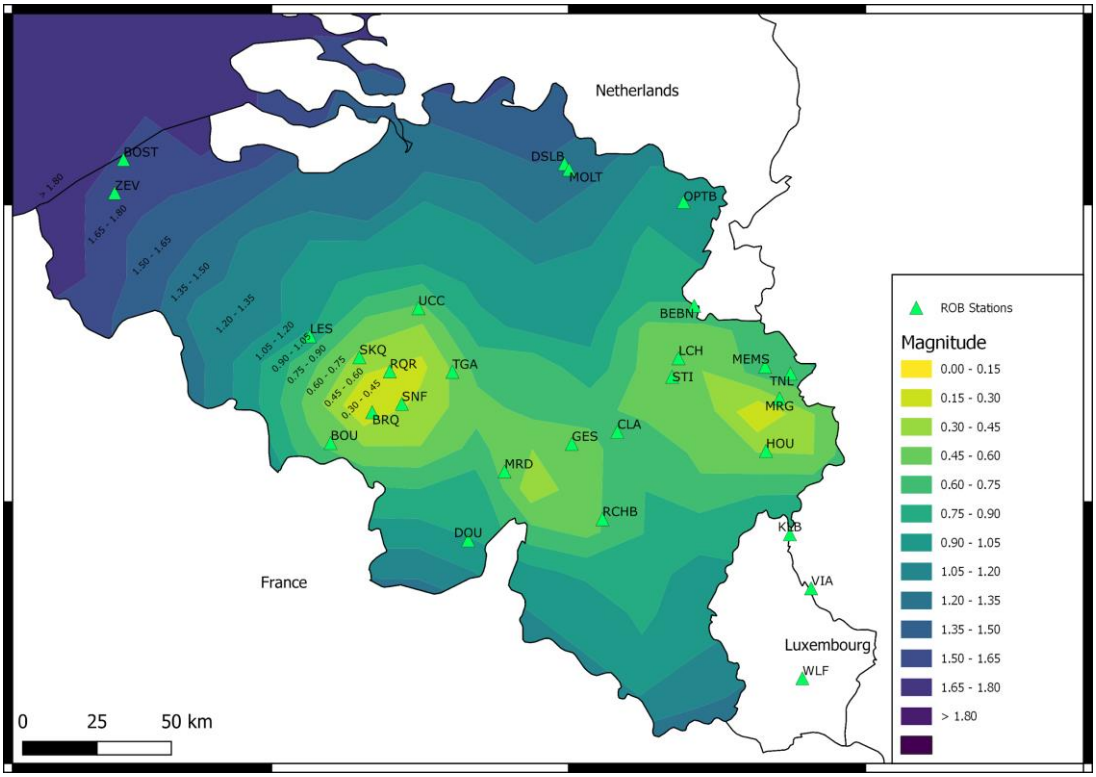

Figure 20: *Minimum magnitude of an event that could be measured on 4 stations of the ROB network, during the day, when anthropogenic noise is the largest.*

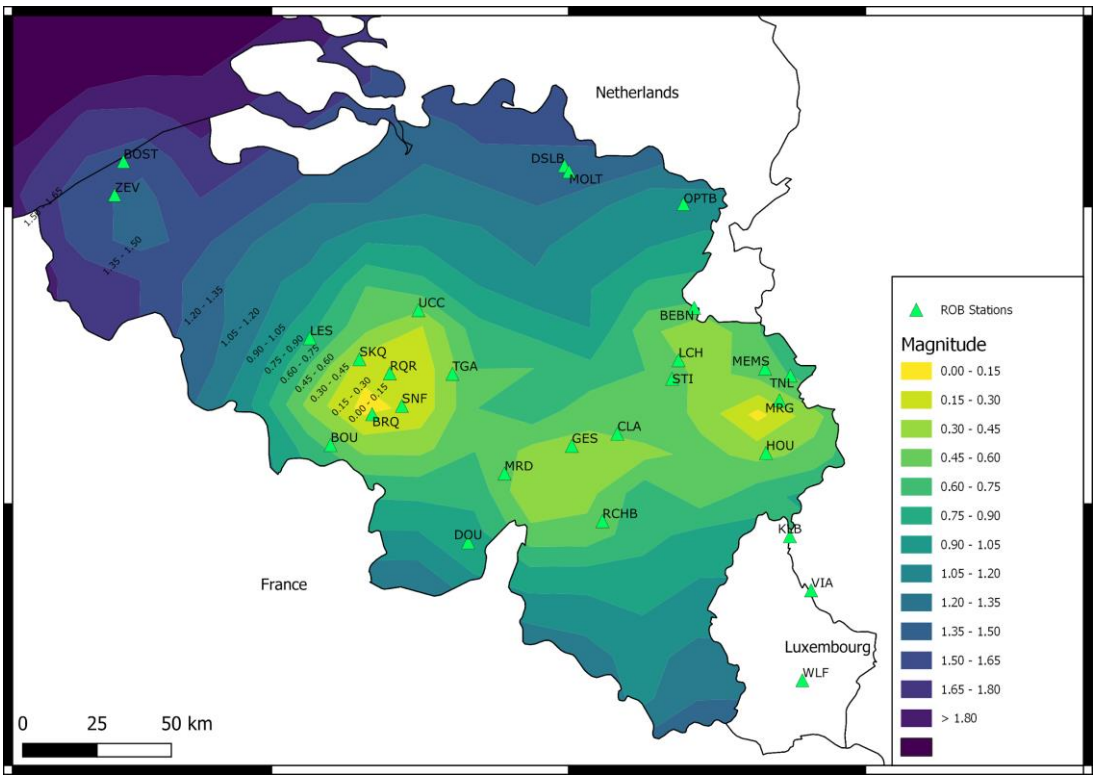

Figure 21: *Minimum magnitude of an event that could be measured on 4 stations of the ROB network, during the night, when anthropogenic noise is the smallest.*

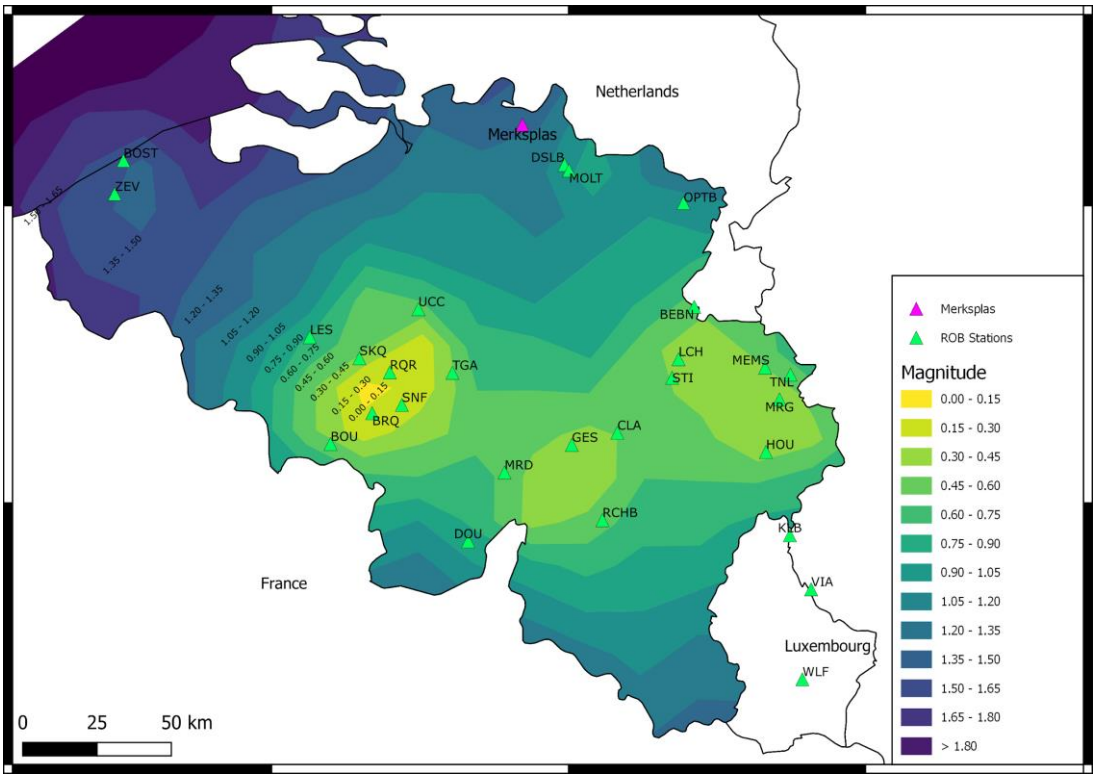

***Figure 22*:** *Minimum magnitude of an event that could be measured on 4 stations of the ROB network, during the night, when anthropogenic noise is the smallest but with testing the impact of adding a borehole seismic station in the Merksplas borehole (KB160). Small differences in the Hainaut or Ardennes are due to changes in the grid used for the computation, not to the addition of the Merksplas station.*

Location by 6 stations - Automatic detection

Although 4 stations are theoretically enough to locate an earthquake, the automatic seismic alert system "SeisComP3" running at the ROB requires the detection on 6 different seismic stations to emit an alert. This requirement smoothes the detection capability map (Figure 23) and highlights two zones with higher detection sensitivity, i.e., the Hainaut and the Ardennes, where the station density is the largest.

Detectability

The detectability is defined as the capability of one single station of measuring a seismic event with enough signal to noise ratio on a filtered waveform. The rationale is that the data from this unique station could be processed with the template matching technique to produce a catalog of events recorded at this location, provided a proper template would be available beforehand (see section 2.4). In the direct vicinity of each station, very small magnitudes (M_L smaller than 0.0) are detectable (Figure 24). For example, events with magnitude M_L = -0.5 could be detected on the Rochefort (RCHB) station at a distance up to 10 km. The importance of borehole stations can be exemplified by the Oostende borehole station (BOST): it has a much lower noise level than Zevekote (ZEV; surface station) and is even more sensitive to events occurring below ZEV than ZEV itself.

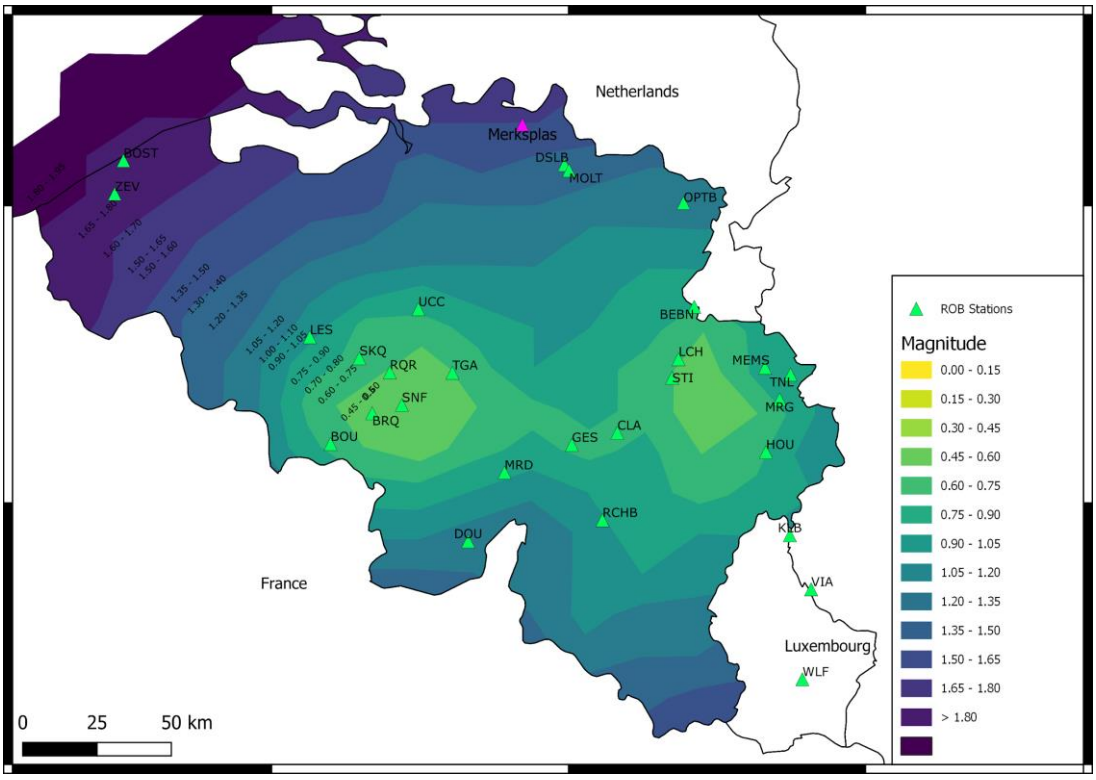

Figure 23: *The minimum magnitude of an event that could be measured on 6 stations of the ROB network, during the night, and could, therefore, be detected by the automatic earthquake alert system.*

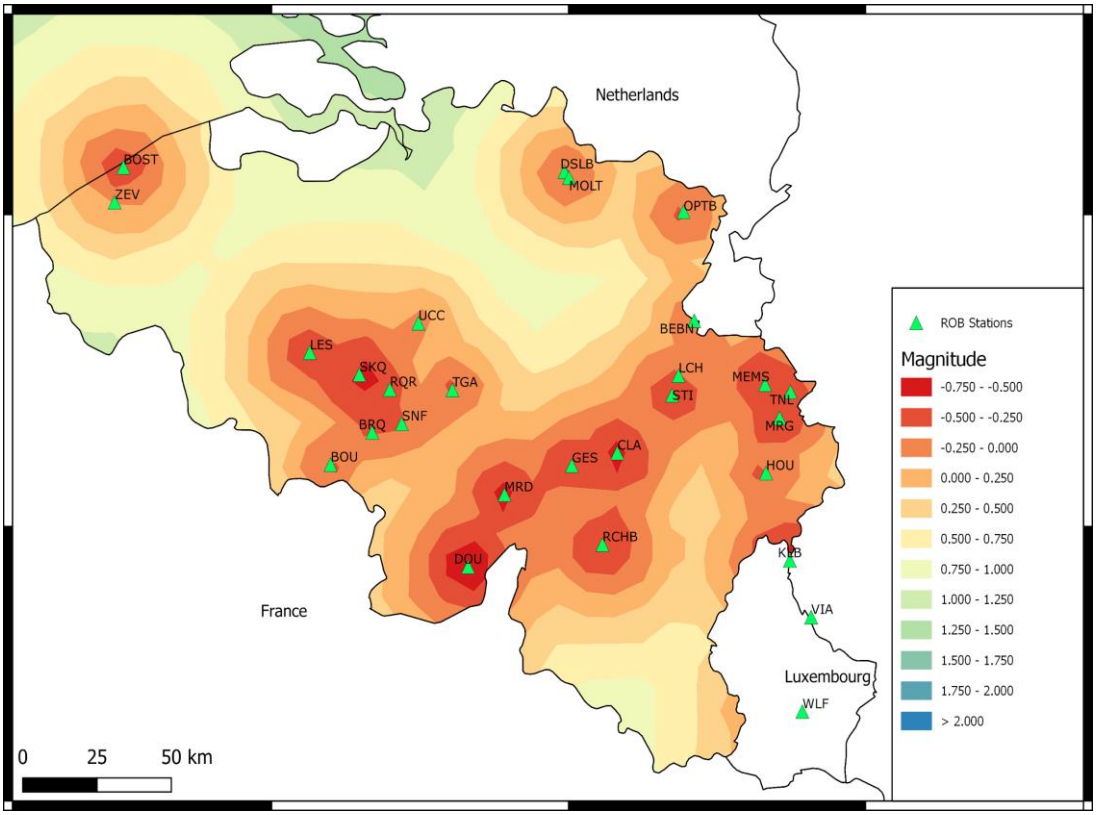

Figure 24: *Single station detectability for the permanent ROB seismic network during the night. Warm colours correspond to smaller magnitudes.*

3.2 RECOMMENDATIONS FOR BOREHOLE SEISMOMETERS

Borehole seismometers usually exhibit better performance than co-located surface stations. This can be verified within the ROB permanent seismic network, where co-located surface and borehole equipment is available (Figure 25). The borehole equipment in Ukkel-Uccle (UCC) outperforms the surface sensor (UCCS) by 25 dB in the frequency band of interest for earthquakes. This results in a ratio of noise levels (for velocity time series) of almost 20 times less noise for the borehole station in this band. This improvement is between 30 and 40 dB for Dessel, 25 to 30 dB for Opitter and 35 to 30 dB for Ostend (note that Zevekote used here for comparison is not directly close to BOST, but scales are within the expected range).

Installing new sensors in quiet areas, and if possible in boreholes would therefore definitely enhance the detection capacity of the Belgian seismic network. This was shown in the previous section with the addition of a station in Merksplas, using the noise level determined for the DSLB station. New locations could be tested using the same methodology. In terms of station coverage, we suggest the installation of new borehole seismometers in Kortrijk (bedrock of the Brabant Massif (BM) at -100 to -140 m), between Gent (BM at -180 m to -230 m) and Lokeren (BM at -275 m to -300 m) and between Tienen (BM at -60 m to -70 m) and Diest (top Cretaceous at -200 m) to increase the minimum magnitude detection in Flanders.

The advantage of using two co-located sensors (borehole and surface seismometer) is that the transfer function between the instruments can be determined, using noise or seismic events (e.g., Verbeeck, 2019). This allows simulating the ground motion at the surface from the probabilistic ground motion computation done for the bedrock.

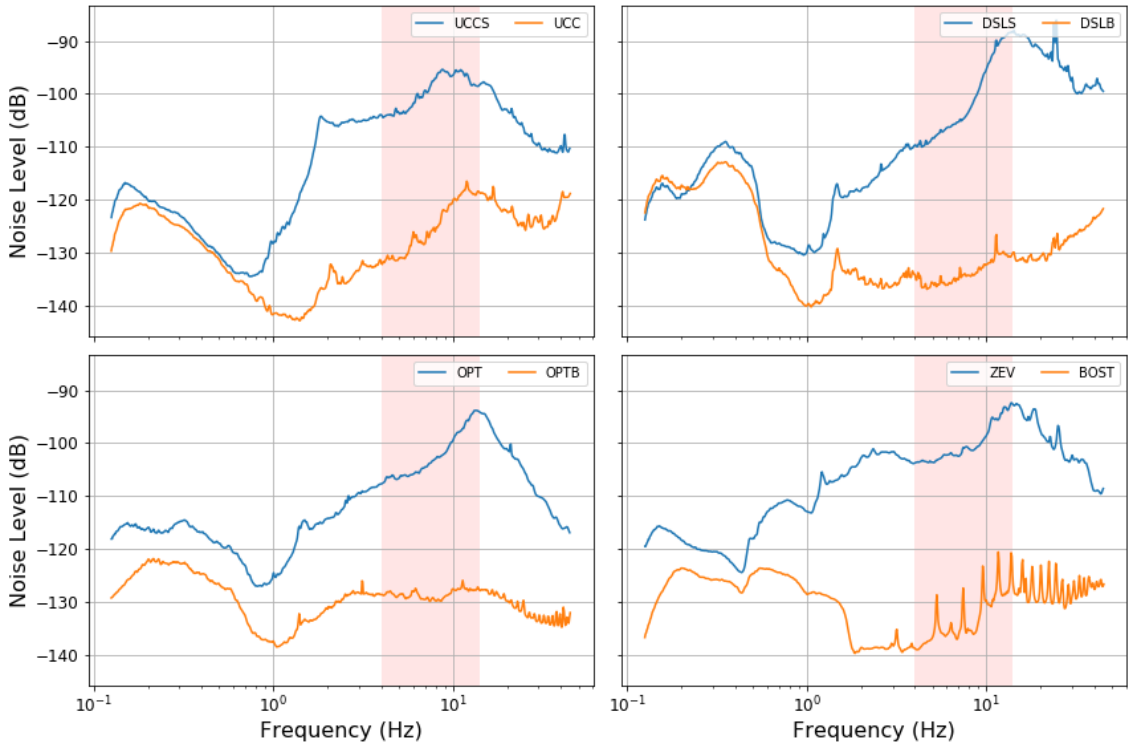

Figure 25: *Seismic noise levels difference as a function of the frequency between co-located seismic stations but installed at different depths (blue: surface station and orange: borehole). The red area represents the 4-14 Hz frequency band used for the noise map computations in the previous chapter. UCC = Ukkel-Uccle; OPT = Opitter; OST = Oostende; DSL = Dessel. The noise level in dB units are $(m/s^2)^2$ / Hz.*

3.3 OVERVIEW OF MAGNITUDE SCALES

In science, there is probably no parameter as earthquake magnitude that is so poorly constrained on the metrological point of view. Magnitudes are surprisingly difficult to estimate accurately. Uncertainties are created by a range of issues including which magnitude scale is used; what type of instrument records the earthquake; how are the instruments deployed and their calibration controlled; and the heterogeneity of the Earth between the source and the receivers. Errors can be up to one magnitude unit largerin scale.

Before the advent of seismometers during the second half of the XIXth century, the only information available about earthquakes was how the vibrations caused damage or were felt by the population. The magnitude and depth of historical earthquakes are estimated based on the distribution of felt and damage reports. Based on these observations, a scale of intensity was created at the end of the 19th century, the best known of which is the Mercalli scale. The methodologies to assess the intensities have been considerably improved ever since: nowadays, in Europe, the EMS98 scale rules and, for example, takes into account the vulnerability of buildings (Grünthal, 1998). Of course, magnitude estimations based on macroseismic data are only possible in populated areas and do not necessarily reflect the actual size of the seismic source as many other effects play a role on the intensity distribution such as site effect, bedrock depth, or radiation pattern.

Nowadays, seismograms recorded by seismometer networks are used to calculate earthquake magnitude, a single value characterizing the size of an earthquake, according to different magnitude scales. To discuss these different magnitude scales, we will focus on the most common local magnitude scale M_L and the moment magnitude scale M_W.

Local Magnitude M_L

Originally, Charles Richter's local magnitude concept of 1935 was quite empirical. He sought to classify the many earthquakes measured in southern California. He noted that the logarithm of maximum ground displacements (seismic wave amplitude) decreased with distance along parallel curves, for many earthquakes. This ground motion decrease (illustrated as an amplitude decrease on a seismogram) is further referred to as distance attenuation. Richter's magnitude concept was thus based on the measurement of the maximum displacement of the ground measured on the seismograms of different stations that had recorded the earthquake. However, to accurately measure the size of the earthquake, the amplitude of the largest wave can only be measured after correcting the amplitude for the distance attenuation (geometrical spreading, scattering, multipathing and anelastic effects) (Figure 26).

The local magnitude M_L, relevant for earthquakes no more distant than 1000 km, is defined by:

$$M_L = A(\Delta) - A_0(\Delta)$$

where :

- $A(\Delta)$ is the maximum displacement of the ground measured at the station located at a distance Δ from the epicentre;
- $A_0(\Delta)$ is the predetermined maximum displacement for an earthquake of zero magnitude, and depends on the region considered. This term makes it possible to consider the attenuation with the distance and is determined by a statistical study. In Richter's time, an earthquake of zero magnitude corresponded to a displacement of 1 µm at 100 km from the epicentre. On a paper seismogram, this displacement was still readable because the reference seismometer, the Wood-Anderson seismograph, amplified the ground motion 2800 times.

In practice, the Richter local magnitude scale is calculated on seismic waves of period close to one second (= one wavelength per second). Because the natural frequency of a building with 10 floors[1] corresponds approximately to this 1 s period, the calculation of the local magnitude remains interesting to evaluate the structural damage an earthquake can cause.

Over time, magnitude estimation based on amplitudes directly measured on the seismograms has changed. For global-scale studies, the body wave magnitude m_b and the surface wave magnitude M_S have been introduced, the former being based on the amplitude of the first arrivals, usually the P wave, and the latter based on the largest amplitude of surface waves, usually Rayleigh waves at 20 s period.

These magnitude procedures are nevertheless appreciated because they are relatively easy to measure and one unit of magnitude increase corresponds to a factor 10 in the amplitude of the displacement of the ground. Practically, the size of the largest wave (often the zero-to-peak value of the S-wave) is measured and corrected for the distance between the event and the station. Based on the amplitude measurement of the largest displacement, a magnitude can be calculated.

However, there are serious limitations: the magnitude varies with azimuth, due the amplitude radiation pattern: for example, a rupture propagating towards the observer will provide displacements higher in amplitude and shorter in time, than a rupture moving away from the observer. The magnitude depends also on the site effects. This difficulty can be smoothed by sufficient station coverage, in azimuth and number, and averaging the results. Each individual result can easily differ by one degree above or underneath the average. The more stations can be used, the more accurate the magnitude and the less influence of local site effects at specific stations on the overall outcome.

Finally, these magnitude scales also depend on the periods of the waves measured: as the rupture size grows, the source emits more and more energy at longer and longer periods and, consequently, these scales eventually saturate. Hence, m_b, which is computed by looking at the amplitude at the period of 1 s, saturates above 6 and for M_S, using waves with a period of 20 s, it is above 8 (Figure 27).

To measure the amplitude properly, traces on the vertical component of the seismometer are first converted from the velocity amplitude to a displacement amplitude (in μm) and afterwards, high-pass filtered at a 1 Hz frequency in order to reproduce the method of Richter, who used a short period instrument. With the measured amplitudes, M_L can be calculated. In Belgium, Camelbeeck (1994) established the distance attenuation correction factor (see

Table **7**) based on digital recordings made by the modern Belgian seismic network and which is nowadays still used. The magnitudes computed at the ROB agree with those provided by the University of Cologne (Bensberg BNS observatory) (Reamer and Hinzen 2004).

[1] As a first approximation, the free period of a building = number of floors /10 [s]

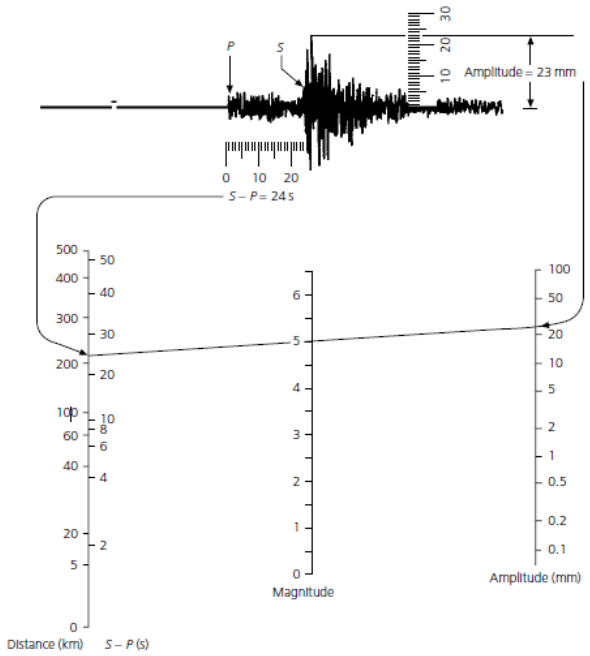

Figure 26: *Principle of measurement of the local magnitude M_L of Richter. The measurement is deduced from the highest amplitude observed on the vertical seismometer, and from the difference in arrival times of the P and S waves, which provides the distance, an essential parameter to take into account the attenuation effect. Here, an amplitude of 23 mm and an arrival time difference of 24 s are measured, giving a magnitude of 5.0 (Bolt, 1993).*

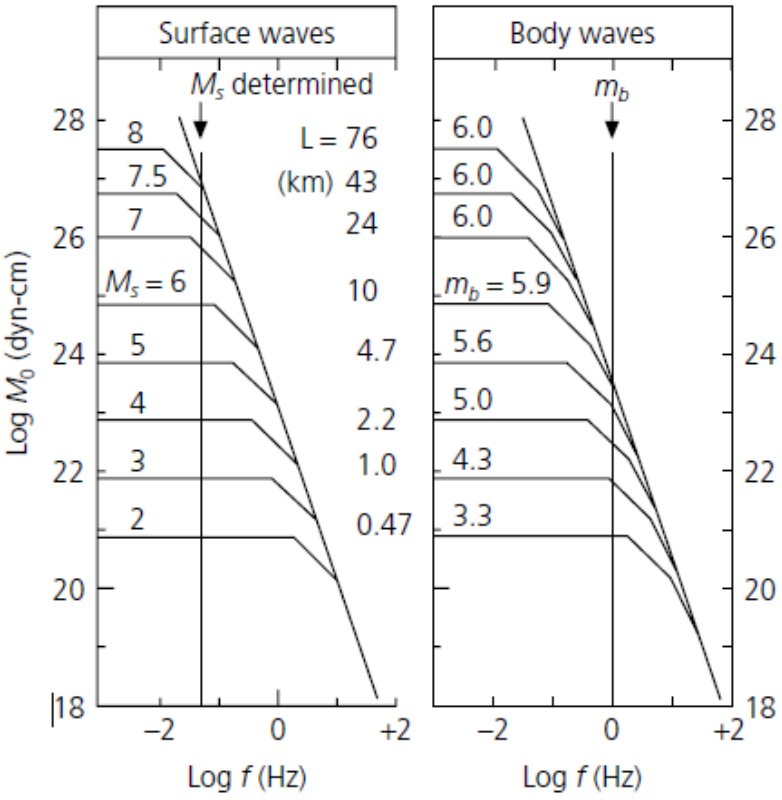

Figure 27: *Illustration of the saturation of scales of magnitudes: beyond a given frequency, the amplitude of the signal no longer increases. For example, at the frequency of 1 Hz, for volume waves amplitude does not increase significantly beyond magnitude m_b 5.6 (Geller, 1976).*

Table 7: *Amplitude - distance relation for a zero-magnitude earthquake used as reference in the local magnitude scale for Belgium.*

Δ (km)	–log A0 (μm)	Δ (km)	–log A0 (μm)
10	2.61	260	4.07
20	2.88	280	4.12
30	3.03	300	4.17
40	3.15	320	4.22
50	3.24	340	4.26
60	3.32	360	4.31
70	3.39	380	4.35
80	3.45	400	4.39
90	3.50	430	4.45
100	3.55	460	4.51
110	3.59	490	4.56
120	3.64	520	4.62
130	3.68	550	4.67
140	3.71	580	4.73
150	3.75	610	4.78
160	3.79	640	4.83
170	3.82	670	4.88
180	3.85	700	4.93
190	3.88	750	5.01
200	3.91	800	5.09
220	3.97	850	5.17
240	4.02	900	5.25

Moment Magnitude M_W

The most realistic measurement of an earthquake is to evaluate the seismic moment M_0. The seismic moment describes the faulting process in terms of the rigidity of the material and the total slip and fault area according to:

$$M_0 = \mu SD$$

With S, the rupture surface area[2], D, the average displacement after the rupture, and μ, the rigidity or shear modulus of the source medium.

By observing the seismic waves at wavelengths greater than the dimensions of the fault, the source of the earthquakes can be considered as punctual and represented by a double couple of forces, of moment resulting zero. The norm of the moment of one of the two pairs is the seismic moment M_0. For large earthquakes, magnitudes greater than 6.5-7.0, the moment is calculated based on seismometer recordings at very long periods (100 s, or even 1000 s for the 2004 Sumatra-Andaman earthquake).

The magnitude scale based on seismic moment, directly related to the size of the source, does not suffer from magnitude scaling problems. When Hiroo Kanamori introduced moment magnitude in 1979, for simplicity, the following scale was used:

$$M_W = \frac{2}{3}[(M_0) - 9.1\,]$$

This scale was established to keep numbers comparable to other scales of magnitudes where these are valid. This preserves the ease of the logarithmic scale. For about twenty years, automated algorithms have made it possible to calculate M_W of great earthquakes.

[2] A tectonic earthquake is caused by a sudden displacement releasing stresses when forces are enough to break the rock or overcome the friction along a pre-existing plane of weakness, i.e., a fault or fracture.

Unfortunately, as seismologists cannot directly measure the geometry of the fault and its displacement at depth, computing M_W is not straightforward. In case of large events, one uses the moment tensor, which is a mathematical representation of the magnitude and orientation of movement on a fault. This requires good seismic station coverage. A more common approach for small magnitude seismic events is to evaluate the seismic moment from the moment function in the time domain or frequency domain (e.g., Stork *et al.*, 2014). This signal is a product of the convolution of the fault rupture time and the rise time and its integral is equal to the moment of the earthquake rupture. The seismic moment, M_0, in the frequency domain at the null frequency, can be determined by measuring the displacement pulse of a P- or S-wave arrival, which can be expressed as:

$$M_0 = 4\pi\rho v^3 r\Omega_0 / R$$

where ρ is the density, v is the seismic velocity at the source (of the P- or S-wave, as appropriate), r is the source-receiver distance, and R is a radiation pattern correction. The term Ω_0 is the low-frequency level of the amplitude spectrum and is equal to the area under the displacement pulse. It is estimated from amplitude spectra that are corrected for attenuation effects.

Assessing M_0, or equivalently, its magnitude M_W is especially difficult for small earthquakes because this requires a good signal-to-noise ratio (i.e., the ground motion induced by an earthquake arrival needs to be higher than the natural or artificial noise continuously measured by a seismometer) in a sufficient number of stations providing good azimuthal coverage, and because part of the useful high-frequency content (say, higher than 10 Hz for $M_W = 2$, and even higher when magnitude further decreases; Hiramatsu *et al.*, (2002)) is already attenuated before the signal arrives at the seismic stations[3]. Borehole instruments (see section 3.2) can overcome this, by installing them on the bedrock (to avoid soft-sediment attenuation) in the close vicinity of the earthquakes, with high sampling rates (e.g., >1000 Hz if one wants to investigate events with negative magnitude)[4]. Computing the moment magnitude is time-consuming, which is difficult to implement when dozens, hundreds or thousands of events are induced. Hence, traffic light systems are rather based on local magnitude, directly inferred from the observed amplitude of the displacement recorded by the seismometers, without the need of computing M_W. Moreover, to automatically search for very small-magnitude events in the seismic data, this method allows comparing the amplitude of the seismic noise with a reference template (see template matching in section 2.4).

Whatever the magnitude, it is worth noting that the used instrument is not of concern, provided its calibration and transfer function are properly considered.

Computing the magnitude of a very small event with nearby stations/using a local network

As explained above, determining the magnitude is never straightforward, and this is even more so when evaluating small magnitude events. To measure small earthquakes, we face a dilemma: to be able to detect events smaller than $M_L \sim M_W \sim 1.5 - 2.0$, waveforms recorded by close-by seismic stations are required as, due to their proximity, they provide a signal-to-noise ratio making it possible to measure the seismic waves in a satisfactory way. However, local magnitude scales were calibrated based on seismic events with magnitudes larger than $M_L > 2.0$ recorded at stations with epicentral distances larger than 20 km (Luckett *et al.,* 2019). In these distant stations, the earthquake signal of small magnitude events is often too low and does not overcome the station's noise level and hence, accurate arrival time and amplitude cannot be measured. However, computing magnitudes using only

[3] For earthquakes of magnitude larger than about 6.0, geodetic measurements of the rupture reaching the surface provide useful information, which can better constrain the moment estimate.

[4] As many other seismic networks, the sampling rate at the ROB seismic stations is usually 100 Hz.

data from nearby stations leads to magnitude overestimation. These problems evidence the need for a calibration of the amplitude-magnitude relations at short distances. Luckett *et al. (*2019) investigate the different reasons for the difference in magnitude calibration:

1) The attenuation curve of seismic waves at short distances is not established:

The geometrical spreading, that is, the attenuation of the seismic signal with distance, cannot be used to explain the increase in amplitude. Geometrical spreading causes an amplitude decrease at a rate of $\frac{1}{r^{1.4}}\ with\ r < 20\ km$, whereas this rate is 1/r at larger distances. In other words, assuming a constant spreading of 1/r at all distances in the standard equation will cause an underestimate of magnitude at short distances. Hence, geometrical spreading cannot be taken into account for the magnitude overestimation. The precise knowledge of the local velocity and attenuation structures are required to properly compute the expected ground motions at the surface (Butcher *et al.*, 2017).

2) The site effects (i.e., local attenuation effects induced by e.g., soft sediment, topography,…) modify the amplitude and frequency content of the signal:

Similarly, magnitude overestimation cannot be explained by a lower attenuation, that is, the amplitude reduction due to local geology at near-source distances. The effect of attenuation is expected to be greater at seismometer sites close to shallow sources than at sites far from the earthquake source. This is related to the fact that part of the seismic ray path (see further Figure 38) is located in the low-velocity and highly-attenuating sediment or weathered bedrock, while usually the local magnitude scale is based on seismic waves that have travelled primarily through deeper and faster crustal rocks.

3) The phases used to compute the maximum displacement of the ground may be different from the ones traditionally used, which are Pg- and Sg-waves:

Using only stations at short distance leads to a systematic overestimation of M_L by 0.5-1.0, as the largest amplitude waveform now corresponds to a different phase than that one used to originally derive the scale. Hence, an explanation for observing amplitudes greater than those predicted by standard attenuation relationships is that a different phase is being measured at a close distance. M_L is usually measured on the S wave. There is evidence that high-frequency surface waves become an important part of the waveform at distances less than 20 km for shallow sources. At close distance, these surface waves have large amplitudes (and hence dominate the M_L scale at short distance) but they attenuate quickly with distance and become quickly less important. This high amplitude surface wave energy explanation, that is thus only present at short distances for shallow earthquakes, is a working hypothesis. This needs further investigation, according to Luckett *et al. (*2019) it is currently the only plausible reason of magnitude overestimation (Kendall *et al.*, 2019).

4) an error in the hypocentral depth estimated (Butcher et al., 2017)

Small depth changes have a strong effect in the path-length to local stations, while it is less significant for distant stations. For example changing hypocentral depth from 3 to 4 km increases the path length by 33% for a station situated directly above the hypocentre, but by only 3% for a station at an epicentral distance of 10 km.

Whatever the physical cause, a correction must be established to create a modified local magnitude scale applicable for small-magnitude events (Luckett *et al.*, 2019). In the UK, the addition of a distance-dependent exponential term to the M_L scale allows correcting for higher than expected amplitudes at small epicentral distances (<20 km). This exponential factor has no influence for magnitude computations at distant stations but starts to have an influence at local stations. To create a magnitude scale applicable for short distances for Belgium would however require a detailed study of small-magnitude events e.g., of seismic swarms.

4. DEFINING THE NEEDS FOR A MINIMAL MONITORING NETWORK

4.1 INTRODUCTION

An appropriate monitoring system must be able to provide the expected information. Monitoring the induced seismic activity is different from monitoring the industrial process to understand the physics of the induced seismicity. In this latter case, one needs to locate the earthquake with a precision of a dozen meters, in order to accurately monitor the way the system reacts to water injection and withdrawal, while usual monitoring of the seismic activity will be less sensitive and provide locations with a precision of a few hundreds of meters, both horizontally and vertically.

Monitoring the industrial process will allow better understanding of the reservoir and the way to exploit it. Such a monitoring requires to install a lot of instruments at the surface and in boreholes, e.g., as done in the Groningen gas field (Netherlands). After determining the purpose of the network, one should first perform a preliminary study to determine the best network geometry, to measure and analyse the seismic noise of the network and to gather local geological information to improve measuring earthquake arrival times. In this section, we explain the proposal and the actual installation of the local Balmatt seismic network, discuss the local geology below these stations and show how a noise analysis can improve the recordings of the local network.

4.2 DESIGNING A SEISMIC NETWORK

As an example of a seismic network installation, we provide here the advice provided by the ROB to VITO in 2017 (Lecocq and Camelbeeck, 2017), for the seismic monitoring at Balmatt site.

The ROB suggested the installation of 5 new three-component seismic stations above and around the production and injection wells of the Balmatt-site, complementary to the already existing NIRAS stations (DSLS, DSLB, MOLS, MOLT). The ROB proposed the installation of:

- 1 deep borehole station above the Injection Point, ideally in the bedrock, at 600 m depth;
- 1 shallow borehole station SE of the Injection Point, at 3600 to 4000 m horizontal distance;
- 1 shallow borehole station NE of the Injection Point, at 3600 to 4000 m horizontal distance;
- 1 shallow borehole station NW of the Injection Point, at 3000 to 3500 m horizontal distance;
- 1 shallow borehole station E of the Injection Point at 5250 m horizontal distance.

A shallow borehole is a station located at a depth of about 30 metres, in order to get rid of part of the free-surface noise and thus ensuring a better signal to noise (SNR) ratio for the measurements. The DSLB (4100 m) and MOLT (3600 m) NIRAS stations can be used as part of a local network, therefore covering the W and SW quadrants around the reservoir, respectively.

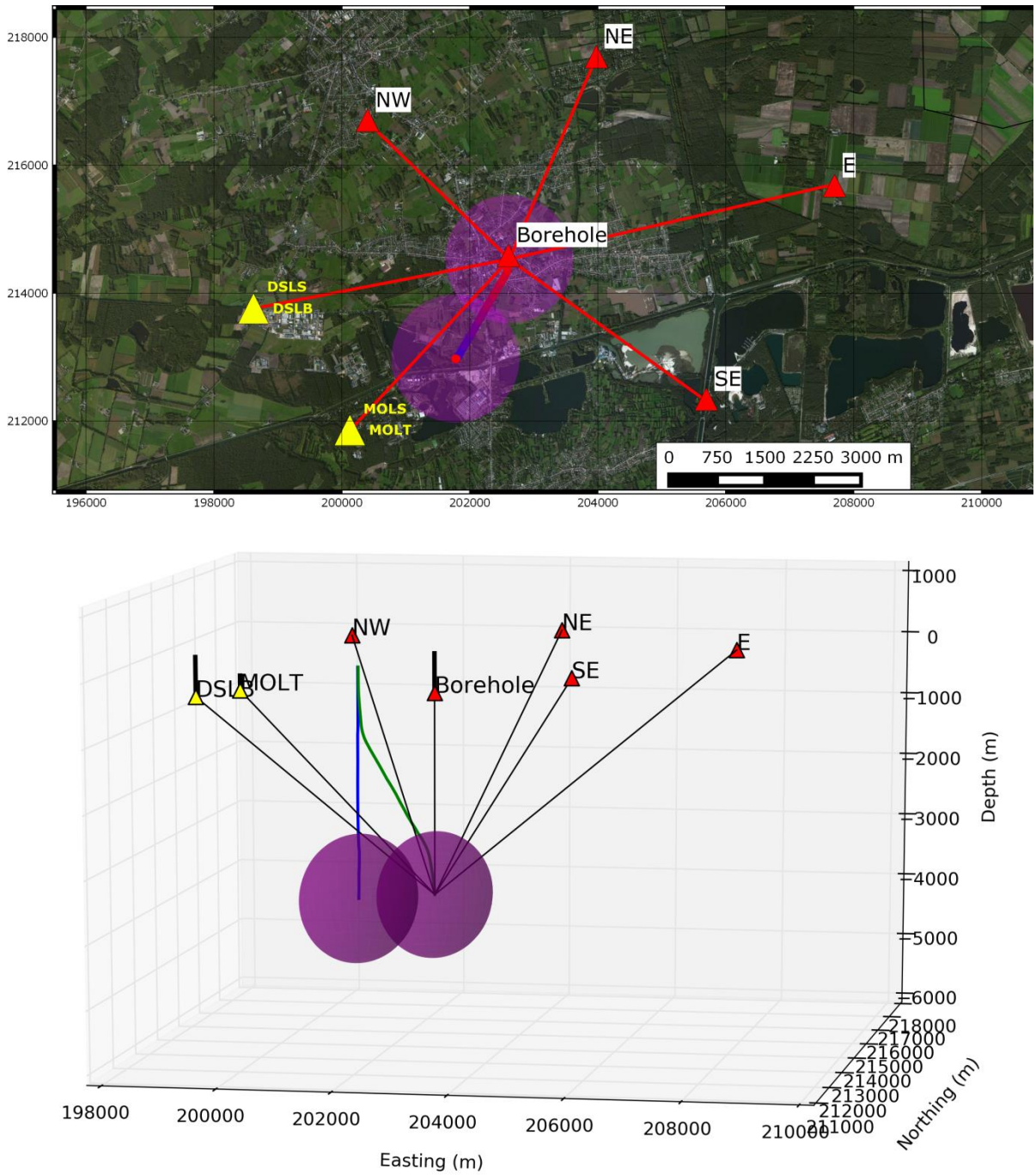

Figure 28: *Map and 3D view of the suggested network (red) including 4 new shallow borehole stations (NW, NE, E, SE) and one deep central borehole station. The NIRAS-ROB permanent seismic stations DSLB/S and MOLT/S are in yellow.* ***Top:*** *The surface projection of the two borehole paths is drawn and coloured from shallow (blue) to deep (red).* ***Bottom:*** *The boreholes are drawn in blue and green. The purple shades indicate a 1 km radius around the injection or the production wells. Source: Lecocq and Camelbeeck (2017).*

The most difficult feature to measure with a seismic network is the depth of the hypocenter. The proposed layout will ensure that there is at least one seismic station close to the injection borehole located at an epicentral distance smaller than the expected depth of the induced events (depth of the injection point), even if the seismic activity migrates up to +/- 1 km from the injection point. This is essential to provide a good determination of the source depth (Z). The furthest stations, will in turn allow a good determination of the epicentre (X and Y). The reasoning for centring on the injection borehole and not on the production borehole is that usually, induced seismicity occurs in large majority

around the injection point (e.g., Megies and Wassermann, 2014). Despite the installation of a seismic station near the injection, the proposed network should allow locating events around the production borehole accurately too.

After this seismic network proposal, VITO searched for potential available boreholes and found two: ON_MOL_2A (used as piezometer) and OMNICHEM_1 (used for groundwater pumping). None of those could actually be used as is, because of the current equipment present in the boreholes. The currently installed network is shown on Figure 28. To comply with the proposal of the network:

- VITO drilled 30 m shallow boreholes for stations RETVK, RETVG, MOLIO;
- VITO drilled a deep borehole for station MOL2A, which was placed at 332m depth (-295.2 m TAW);
- Close to the injection well, VITO drilled a deep borehole for the central DSLNZ seismometer installed at 604 m depth (-578.4 m TAW). VITO proposed this location because it is located on the Balmatt property and it is located in the middle of two (1 existing, 1 future) injection boreholes.

4.3 TESTING THE QUALITY OF THE LOCAL SEISMIC NETWORK

Probabilistic power spectral density

In 1985, before installing the first surface stations of the modern Belgian seismic network, the ROB performed a noise analysis at many sites in southern and central Belgium to search for locations with an acceptable noise level for the detection of low-magnitude events (Camelbeeck *et al.*, 1990). Choosing sites for a local geothermal borehole network based on preparatory surface records is however more challenging. Therefore, after geothermal network installation, evaluating the quality of borehole seismic network by analysing seismic noise levels is mandatory. The noise level at a seismic station can be evaluated using the probabilistic power spectral density (PPSD) of its records (McNamara and Buland, 2004). A PPSD illustrates the variation of noise levels, i.e., the signal's power at different frequencies for different channels for a certain time interval.

Lecocq (2019) calculated the seismic noise levels of the ROB-NIRAS stations (BE.DLSS, BE.DSLB, BE.MOLS, BE.MOLT; Figure 29) and the VITO seismic stations (ML.RETVK, ML.RETVK, ML.DSLNZ, ML.MOLIO, ML.MOL2A; Figure 30). Seismic noise is analysed in windows of 600 seconds to compute the power spectral densities, which are aggregated to obtain the PPSD. The period band of interest for the following figures is broad, from 10 s (0.1 Hz) to 0.01 s (100 Hz), but the most important part for the induced seismicity is above 1 Hz. Traditionally, seismic noise levels are compared to global Low and High Noise models (NLNM and NHNM, Peterson, 1993).

The ROB-NIRAS seismic stations in the Dessel borehole and tunnel exhibit a clear difference in the noise levels at frequencies above 1 Hz compared to the seismometers at the surface. At frequencies above 1 Hz, the noise is dominated by local, mostly anthropogenic sources. The difference in noise level between surface and depth and surface stations is the main reason why the ROB advised VITO to install seismometers at depth.

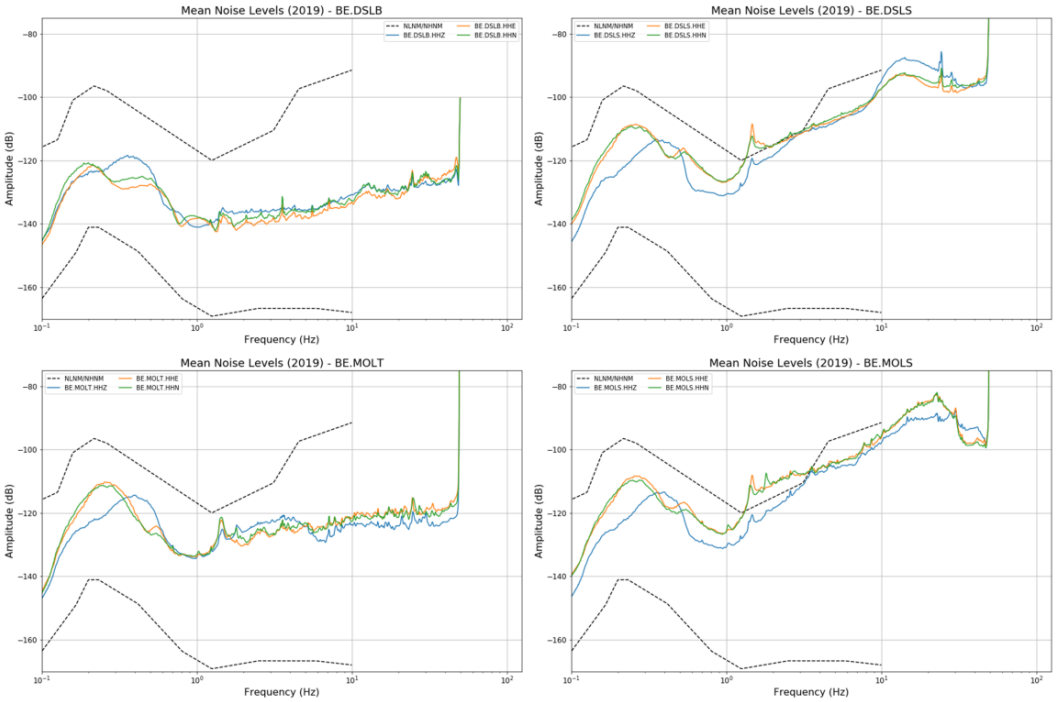

Figure 29: *Seismic Noise levels of the ROB-NIRAS Stations (left: borehole or at depth, right: surface).*

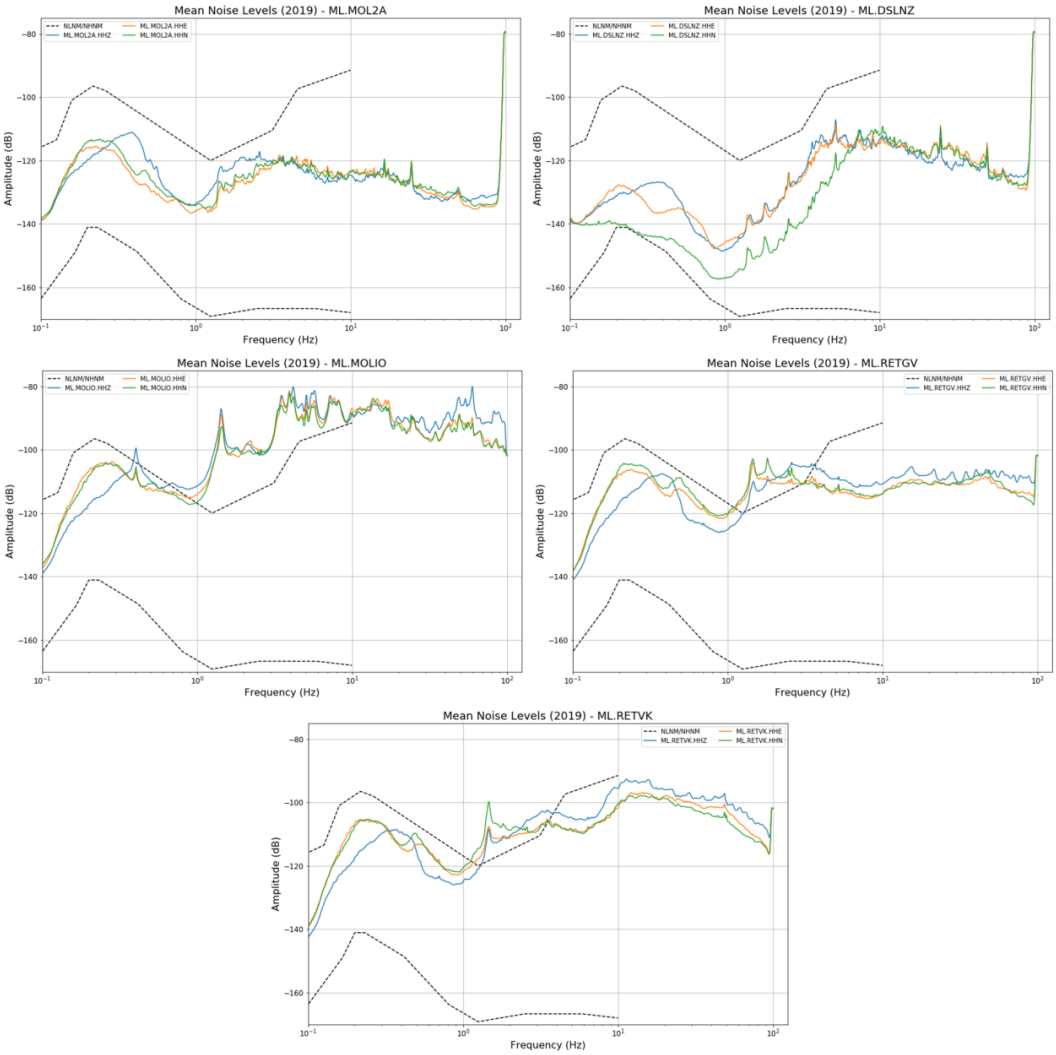

Figure 30: *Seismic Noise levels of the five VITO seismic Stations.*

The VITO seismic stations located at depth (ML.MOL2A at -332 m and ML.DSLNZ at -604 m) show better performances than the others (ML.MOLIO, ML.RETGV and ML.RETVK at -30 m). ML.MOL2A exhibit a higher noise level than BE.DSLB between 1 and 10 Hz and is comparable between 10 and 50 Hz. ML.DSLNZ has a lower noise level than BE.DSLB between 1 and 2 Hz, but has a much larger noise level between 2 and 50 Hz. This shows that, in the frequency band of interest for the induced seismic activity (above 1 Hz), the VITO stations in deep boreholes (ML.DSLNZ, ML.MOL2A) perform less good than the ROB-NIRAS borehole station BE.DSLB.

Among the VITO surface stations, ML.MOLIO has very high, above-reference, noise levels between 1 and 100 Hz. The sharp peaks in its mean spectrum are probably related to resonating structures, including a windmill at less than 50 m from the station. ML.RETGV and ML.RETVK have a relatively flat noise level between 5 and 50 Hz, with ML.RETGV performing as good as ML.DSLNZ between 8 and 50 Hz.

Vertical seismic ground motion polarity and amplitude

Another network test is to confirm if all stations have the same orientation and the right calibration. In order to compare waveforms and polarity of all stations simultaneously without any distortion of the local noise and site effects, the ground motion of a distant teleseismic earthquake is used as earthquake arrivals enter the network at the same time, in the same manner. Here, the 26 May 2019 Peru earthquake at 122 km depth (magnitude M_W=8.0) is used for the comparison (Figure 31). The time-series recorded by the ROB-NIRAS and VITO stations exhibit the same features and all arrivals are visually in phase (Figure 32).

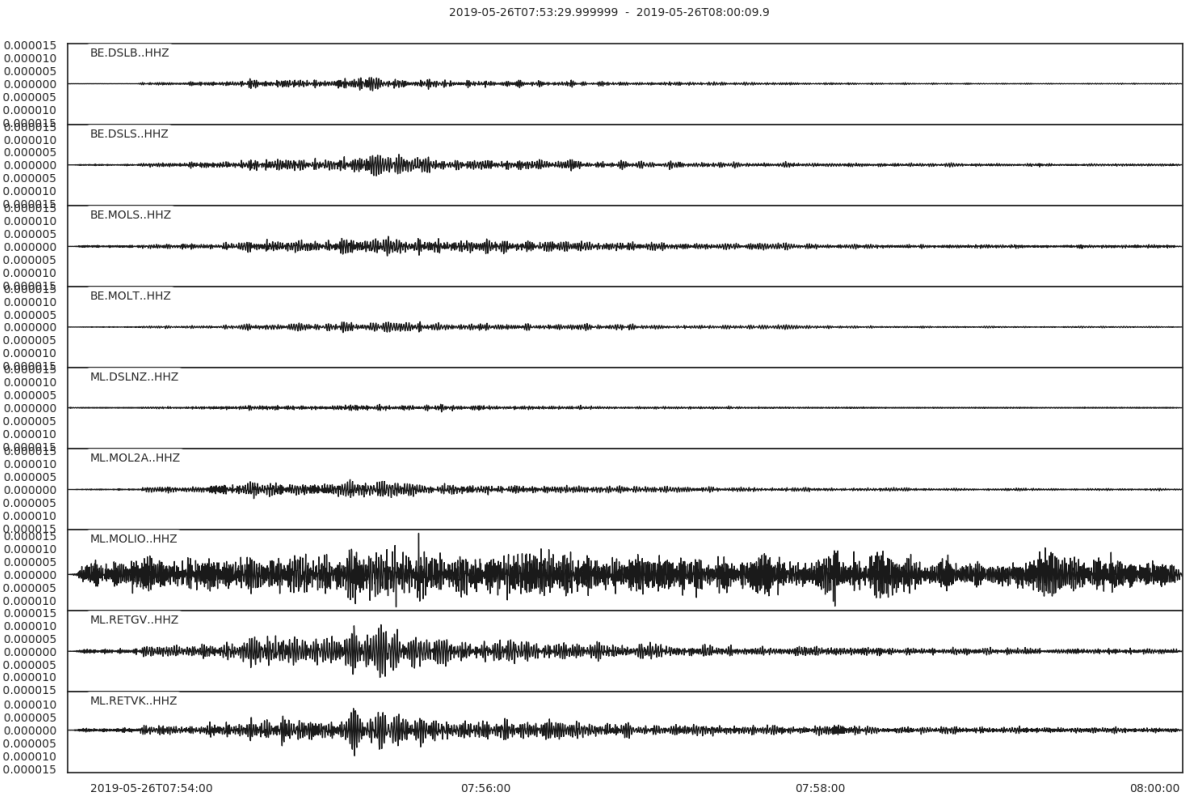

Figure 31: *Velocity (nm/s) seismograms of the ROB-NIRAS and VITO stations for the Peru earthquake on 26 May 2019. The amplitude scale (y-axis) is identical for all seismograms. Filtered data between 1 and 4 Hz. Source: https://earthquake.usgs.gov/earthquakes/eventpage/us60003sc0/executive*

Lecocq (2019) computed the instrument-corrected (*Disclaimer: the current computations have been done using the instrument responses provided by VITO/DMT, we assumed those to be correct*) velocities of all seismic stations between 0.05 and 0.2 Hz in order to compare their waveforms and polarity while minimising the site effects that would occur at higher frequency. The instrument response correction includes a scaling parameter to convert from counts of the digital record to meters/second. These parameters are summarised in Table 8 for the ROB-NIRAS and VITO stations and are identical to the ones computed by INERIS (2019), except for BE.DSLB but the difference is subtle.

Table 8: *Scaling parameters for all stations*

Station Code	ROB [m/s/count]	INERIS [m/s/count]	Station Code	ROB [m/s/count]	INERIS [m/s/count]
ML.DSLNZ..HHZ	1.08E-09	1.08E-09	BE.DSLB..HHZ	5.47E-10	5.34E-10
ML.MOL2A..HHZ	1.08E-09	1.08E-09	BE.DSLS..HHZ	4.27E-09	
ML.MOLIO..HHZ	1.22E-10	1.22E-10	BE.MOLT..HHZ	5.37E-10	
ML.RETGV..HHZ	1.22E-10	1.22E-10	BE.MOLS..HHZ	5.32E-10	
ML.RETVK..HHZ	1.22E-10	1.22E-10	BE.MOL4..HHZ	3.31E-09	3.31E-09

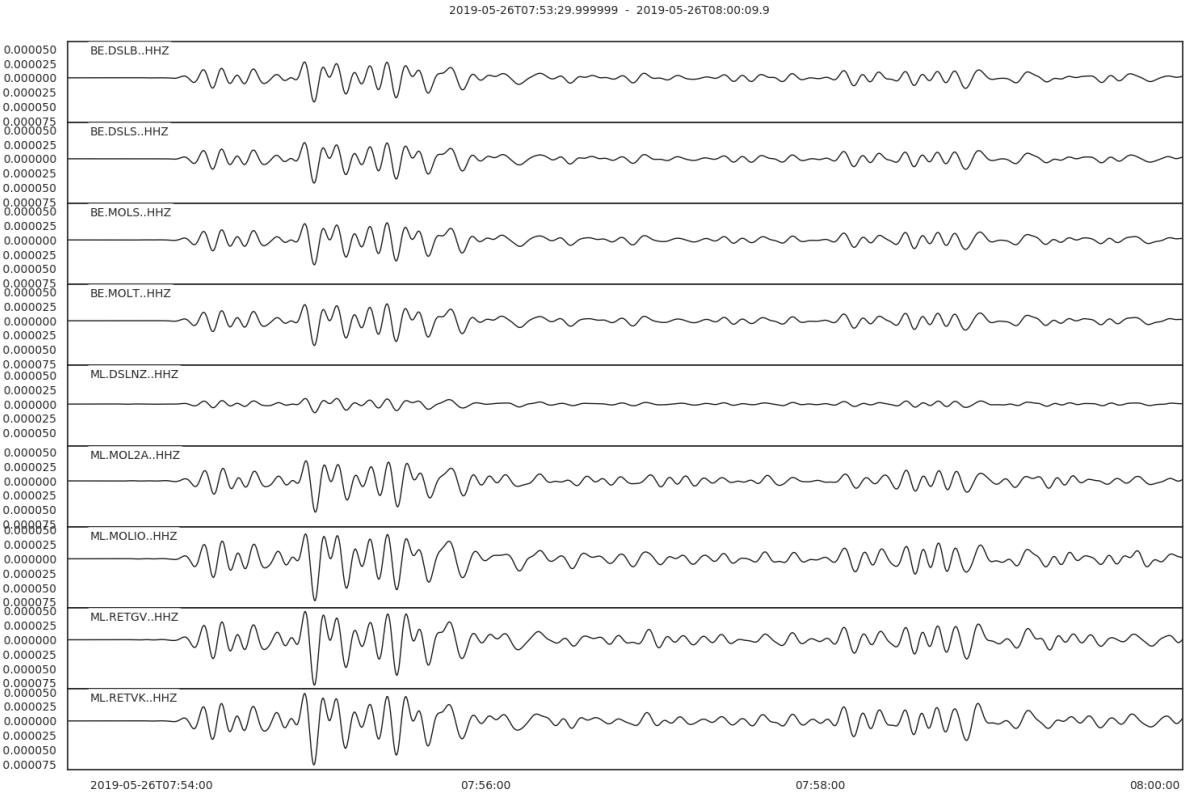

Figure 32: *Velocity (nm/s) seismograms of the vertical component of ROB-NIRAS and VITO stations for the Peru earthquake on 26 May 2019. The amplitude scale (y-axis) is identical for all seismograms. Filtered data between 0.05 and 0.2 Hz.*

Vertical component comparison

Comparing seismometers pairwise allows confirming if all vertical components have the same orientation (positive slope) and their relative amplification (slope diverging from 1:1). In the following, we use BE.MOLS as a reference to compare with all stations. BE.MOLS was chosen because it is a surface station, thus theoretically the most comparable to all other surface or shallow depth stations. The ROB-NIRAS stations behave very similarly, with correlation slopes between 0.95 and 0.99 and very little spread around the 1:1 line (Figure 33). The very small spread can be partly attributed to the distance between the stations and the reference BE.MOLS station (~2.39 km).

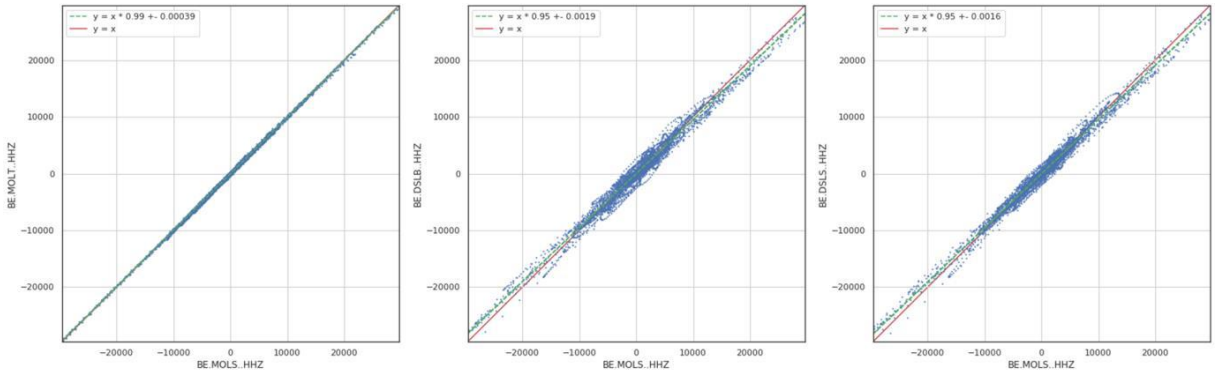

Figure 33: *Relative particle motion of the vertical component of each ROB-NIRAS station compared to BE.MOLS. This shows, for example, that when the waveform of BE.MOLS goes up in Figure 32, the waveform of BE.MOLT exhibit almost exactly the same change: their waveforms are highly correlated.*

The VITO stations exhibit a less good agreement in amplitudes (correlation spread) but the polarity is identical (positive slopes, Figure 34). Although far off its nominal frequency, ML.MOL2A shows a reasonably good agreement with BE.MOLS, probably thanks to its large installation depth. ML.DSLNZ, however, shows a big difference in amplitude (correlation slope=0.33), which is also visible on the seismograms (Figure 32). This difference can neither be attributed to the distance because BE.DSLB and ML.DSLNZ do show a better correlation and have a similar distance with the reference. Concurrently, the 0.33 amplification factor cannot be explained by the difference in depth between ML.DSLNZ and BE.MOLS because BE.DSLB, also installed at 600 m depth, exhibits a 0.95 correlation of its amplitude. As ML.MOL2A, ML.DSLNZ is a 2 Hz geophone and the computation done here is thus relatively far from their nominal frequencies. But, because they are the same type of instrument, it would be expected that they exhibit the same amplitude ratios. ML.RETVK, ML.RETGV and ML.MOLIO show similar behaviours, with amplification of 1.6 relative to BE.MOLS.

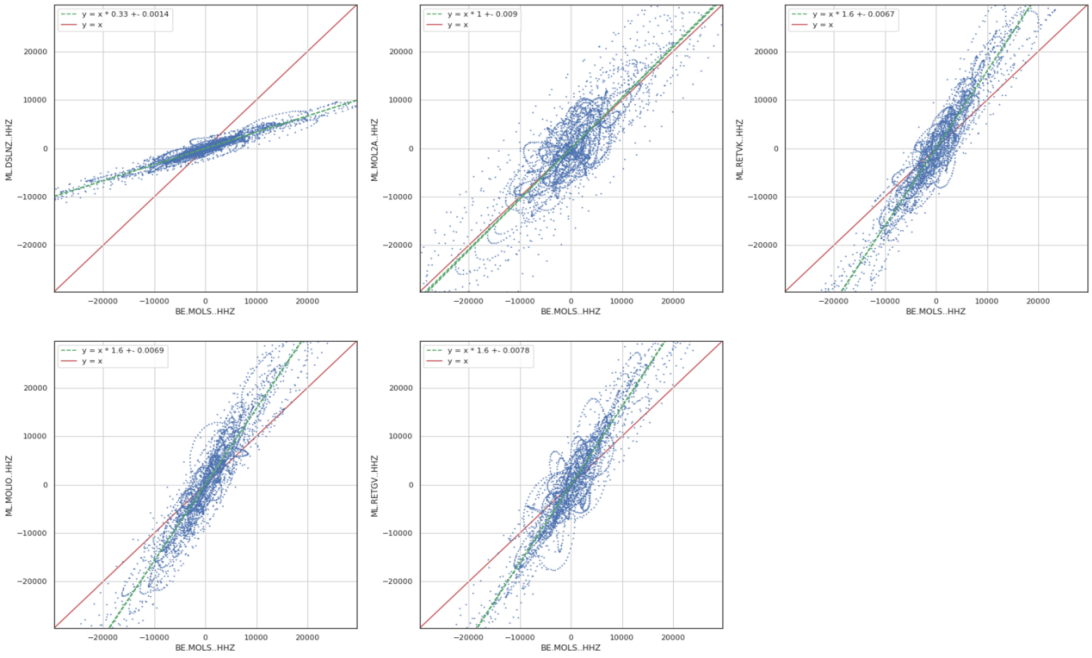

Figure 34: *Particle motion of the vertical component of each VITO station compared to BE.MOLS.*

Horizontal component comparison

Repeating the processing above for the horizontal components, we can evaluate the agreement between the E-W and N-S motions for all sensors.

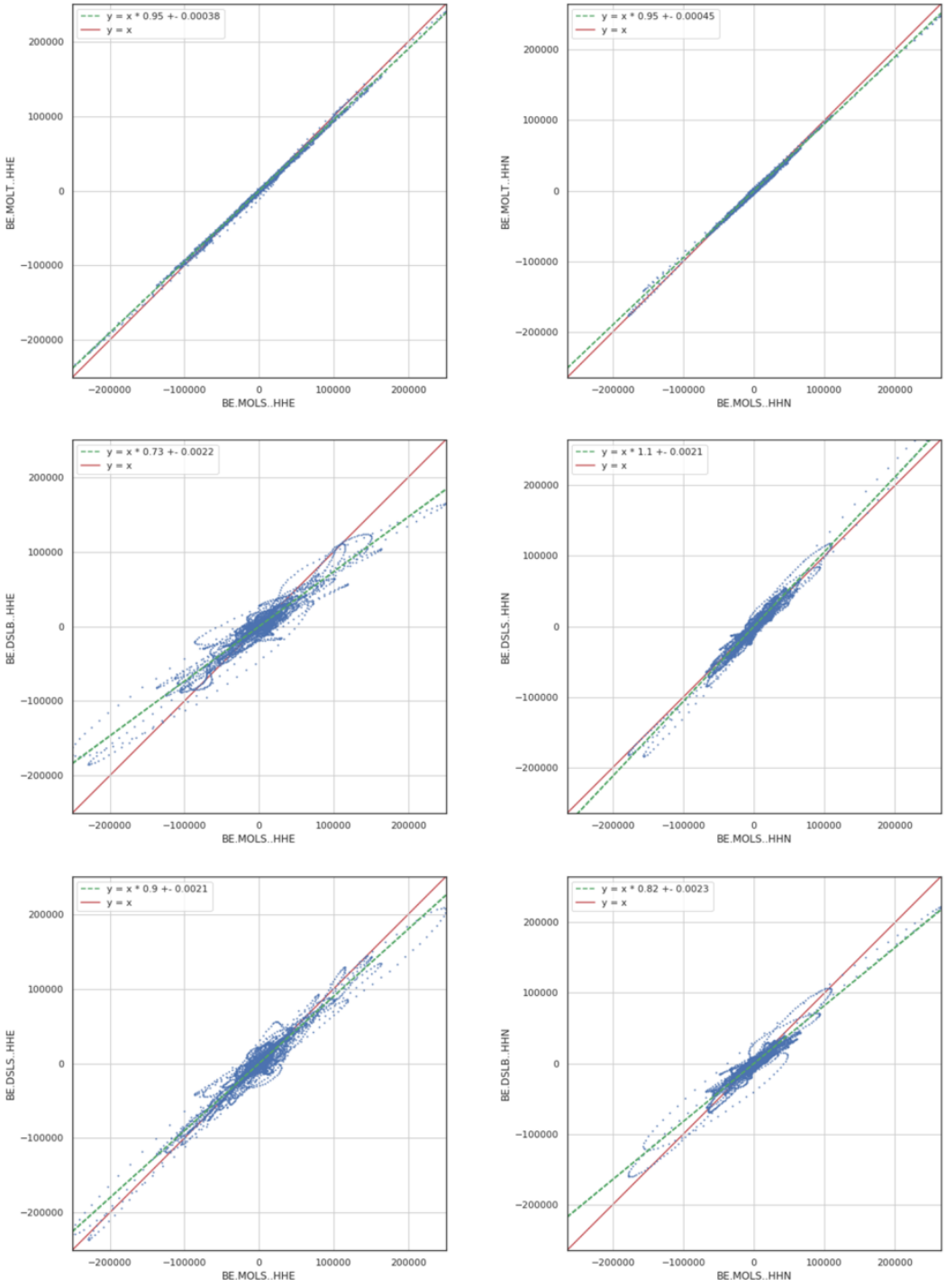

Figure 35: *Particle motion of the East-West (left) and North-South (right) components of each ROB-NIRAS station compared to BE.MOLS showing the good agreement between the recorded ground motions.*

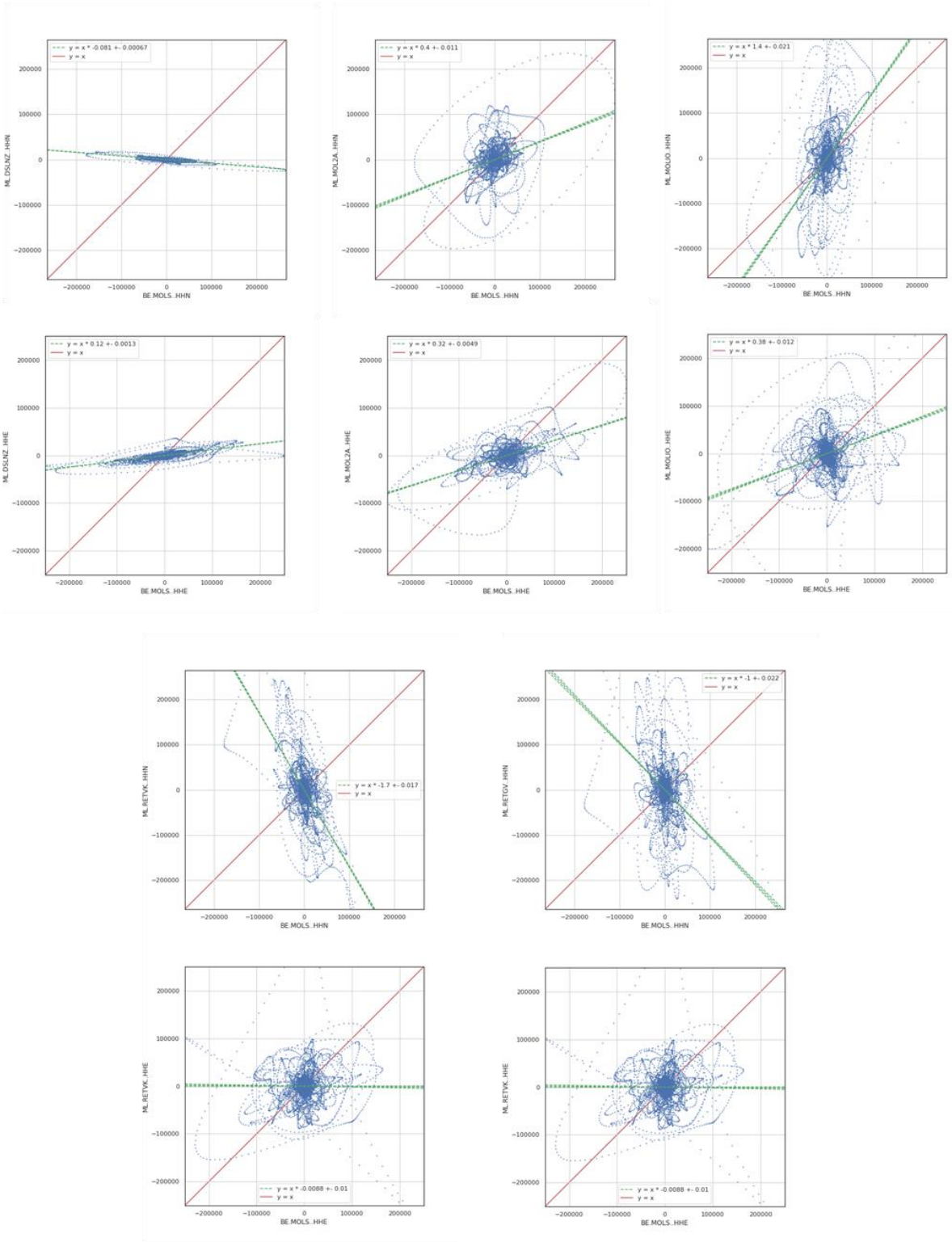

Figure 36: *Particle motion of the East-West (left) and North-South (right) components of each VITO station compared to BE.MOLS showing a disagreement between the recorded ground motions.*

Seismic stations installed at depth usually provide 3 component data in the form of "Z, 1, 2" or "1, 2, 3" because one doesn't know the final orientation of the instrument in its borehole. The data streams are then rotated to produce "Z, E, N" when the orientation of the instrument has been determined, usually by comparing the records of the natural microseismic energy radiated from the oceans or records of large events at teleseismic distances. The ROB-NIRAS stations are highly correlated

(waveforms are almost identical on all components, Figure 35) while the VITO stations are de-correlated (Figure 36). The origin of this de-correlation could be caused by a lack or improper rotation between the "Z,1,2" and "Z, N, E". This explanation was finally confirmed by DMT as they provided the “Z, 1, 2” data, but named “Z, E, N”, renaming 1 and 2 in E and N, respectively, without applying the correction.

Conclusion

The seismic noise levels of the ROB-NIRAS and VITO stations were computed and compared. The seismic stations located at depth have far better noise levels than the surface stations, as expected from the literature and ROB experience. Above a few Hz (the frequency band of interest for induced seismicity), the VITO stations perform relatively well, except ML.MOLIO which is highly impacted by resonating structures (likely the closely-located wind turbine).

By comparing the seismic amplitudes recorded at long period for a distant M_W 8.0 earthquake, thus avoiding the influence of site-effects at high frequencies, it is shown that the ROB-NIRAS stations behave coherently. ML.MOL2A exhibits a similar correlation, but with a larger spread, around the 1:1 amplitude. We identified a systematic 1.6 x calibration mismatch for three stations (ML.RETVK, ML.RETGV and ML.MOLIO), this factor being 0.33 for ML.DSLNZ. This large change is clearly visible on the low-frequency time-series of the event recorded (Figure 32), but also at higher frequencies (1-4 Hz) including the nominal response of the 2 Hz geophones installed at depth. All stations exhibit a positive slope of the amplitude correlation, meaning they share the same polarization of the vertical component. The horizontal components of the ROB-NIRAS stations are properly oriented and can be considered as real North-South and East-West components. This is not the case for the VITO stations, as we were not provided with the correct orientation of the instruments. Therefore, the data from the "North-South" and "East-West" components should be called "1" and "2" until the rotation information is applied to correct the waveforms.

General Advice

An operator should (i) design the network in a way that low-magnitude earthquakes in the expected source area can be located with adequate horizontal and vertical precision, (ii) perform a network performance noise, calibration and orientation tests after network installation and (iii) be ready to move a seismic station if a station’s noise level is above the expected value incapable to measure low-magnitude events. A preliminary survey of the noise levels at the surface, for example by deploying seismic nodes (standalone, self-contained stations) in and around the planned area could be suggested to prevent bad surprises. A preliminary calculation of the network performance can be done to obtain an estimate of the location errors in X, Y and Z that are associated with the network design, and with its noise estimates or the uncertainties (or approximations from 3D to) the 1D velocity model.

4.4 IMPORTANCE OF THE SEISMIC BEDROCK AND THE LOCAL GEOLOGICAL STRUCTURE

Shear-wave velocity (Vs) borehole measurements in the Dessel-1 and Mol-1 boreholes show that at the contact between the Paleocene Hannut (Hn) and Heers (Hs) Formations, Vs is in excess of 800 m/s (Verbeeck, 2019), a value that is considered as bedrock in EUROCODE 8 (Bureau voor Normalisatie, 2011). This particular formation contact is (in this context) therefore considered as the seismic bedrock. The G3Dv3 model of Databank Ondergrond Vlaanderen (DOV; Deckers *et al.,* 2019) allows to derive (Table 9) and image (Figure 37) the variation of the bedrock morphology below the seismic network by using the base of the Hannut Formation (DOV code name: 0318PA_Hn_b). Apart from the bedrock morphology, also the fault dip is illustrated on Figure 37 by using coloured traces that each represent the presence of a fault at different horizons.

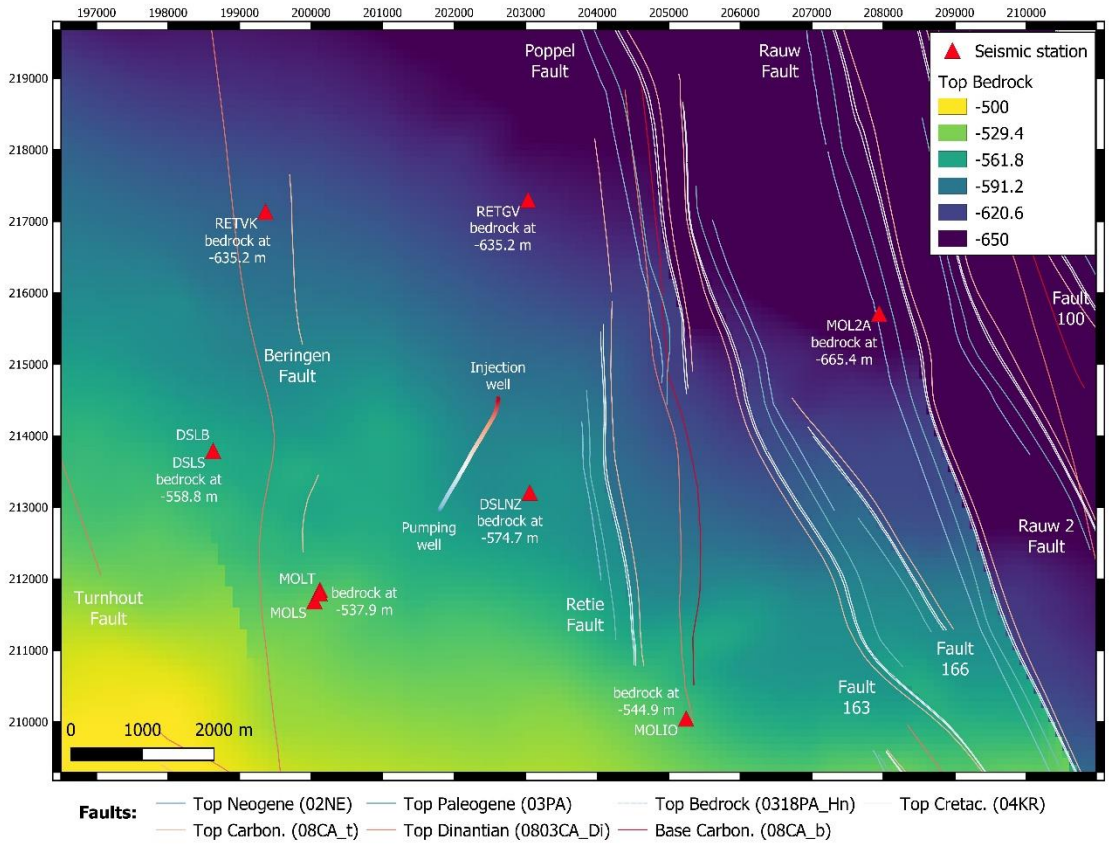

Figure 37: *Balmatt seismic network illustrated on a top of the bedrock (base of the Hannut Formation) depth map (DOV code name 0318PA_Hn_b, G3Dv3, Databank Ondergrond Vlaanderen). For each station, the altitude of the bedrock (in m TAW) is indicated. The colored trajectory shows the deviated injection borehole. Both at Mol and Dessel there is a surface station (MOLS, DSLS). DSLB is placed within a borehole at -578m. At Mol, several stations are present within the NIRAS gallery (MOLT and MOL1-5) at -198 m (see also Table 9). Fault lines and their G3Dv3 indications and codenames are shown as well with white lines being fault traces at the top of the bedrock (0318PA_Hn_b)*

For future seismic networks, evaluating the bedrock depth is important because (i) cover sediments modify the ray path propagation of seismic waves and cause ground-motion amplification/damping at the surface (site effects, see Chapter 5), and (ii) earthquake ray paths experience a strong refraction at the seismic bedrock interface (Figure 38). The larger the velocity contrast at the bedrock, the larger this refraction angle. Understanding the geological structure and the seismic bedrock depth below each station is of importance to (i) to improve the earthquake location using correct site conditions below the seismometers and (ii) compute the correct focal mechanism using first motion P-wave

arrivals or using the full waveform information on all components. Focal mechanisms describe the orientation of the fault plane that slipped and the slip vector at the earthquake source and are computed by plotting the first motion P-wave arrival on a lower-hemisphere stereographic projection, i.e., the focal sphere. The take-off angle at the source and the azimuth to the station are used to plot the position of the seismic station on the focal sphere. For closely-located seismic stations in a local network, slight differences of the seismic bedrock depth affect the estimation of the take-off angle and, hence, affect the final result of the focal mechanism computation.

Table 9: *Local seismometer network at Balmatt and indication of depth of installation (Seis. depth) and absolute position in m TAW (Seis. Abs.). Using G3Dv3, the absolute location (m TAW) of the top of the bedrock (0318PA_Hn b), top (0803CA_Di_t) and base (0803CA_Di_b) of the Dinantian reservoir of 'Kolenkalk' are given. Both DSLNZ and DSLB can be considered to be installed in the bedrock.*

Name	Northing	Easting	Z	Seism. depth	Seism. Abs.	Top Bedrock	Top Dinantian	Base Dinantian
RETVK	199363.4939	217136.8966	23.6	30	-6.4	-604.6	-3512.3	-4472.7
MOL2A	207941.6543	215712.1558	36.8	332	-295.2	-665.4	-4228.1	-5321.7
DSLNZ	203056.5166	213208.8388	25.6	604	-578.4	-574.7	-3258.3	-4270.3
MOLIO	205242.4479	210049.8494	30.1	30	0.1	-544.9	-3505.8	-4540.4
RETGV	203034.5043	217301.8153	36.8	30	6.8	-635.2	-3636.3	-4674.2
DSLB	198630.7897	213759	23.6	601.6	-578	-558.8	-3206.4	-4144.2
MOLT	200131	211748	25.4	223.4	-198	-537.9	-2984.9	-3945.8

Figure 38 illustrates the extreme difference for calculating the ray path trajectory of an induced earthquake at a fixed position using a bedrock velocity model (cf. Camelbeeck 1994, Cam93) or a layered velocity model (Dessel model). The Cam93 velocity model is used at the ROB for the location of natural earthquakes and is considered as bedrock velocity model because the majority of the ray propagation of natural earthquakes occurs within the bedrock. The Dessel model respects the local geological structure at Mol and Dessel and uses Vs and Vp determined from the Mol-1 and Dessel-1 boreholes and the seismic bedrock depth derived for stations DSLB, DSLS and DSLNZ (as indicated in Figure 38). Both velocity models are 1D models.

The goal of such an exercise is to calculate the correct take-off angle at the source and predicting a correct ray path using a local velocity model. Because of the large velocity changes in the Dessel model, strong refraction takes places at the specific horizons and as a result, the Dessel stations appear at a higher projection angle (i.e., closer to the centre, Figure 38) on the focal sphere than if the bedrock model is used. Hence, doing this exercise for all stations in a local network results in a different focal mechanism computation. This example is an explanation why different organisations may compute different first motion arrival focal mechanisms. Another explanation, when the focal mechanism is obtained through full waveform inversion, can be a wrong seismometer calibration, and more generally, the small SNR of the events recorded (such as in the Balmatt case).

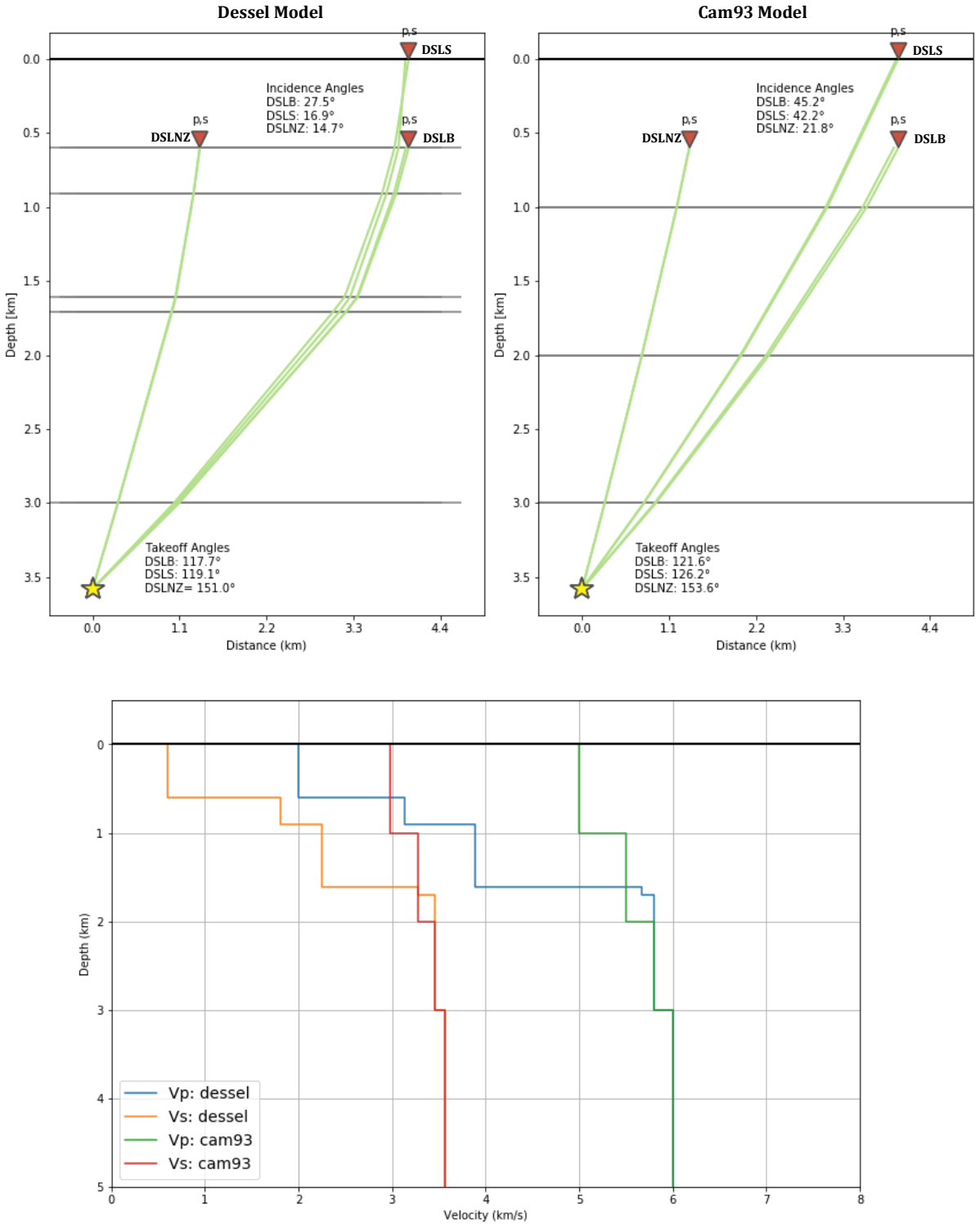

Figure 38: Above) *Two seismic wave trajectory scenarios of an induced earthquake at 3.6 km depth recorded by three stations (DSLS, DSBL and DSLNZ). The two ray trajectories, takeoff and incidence angles are different because of the usage of two different velocity models (**below**), i.e., the layered Dessel model (Vs and Vp from Verbeeck, 2019) respecting the local geological structure and the Cam93 bedrock model (Camelbeeck 1994), which is generally used at the ROB for the location of natural earthquakes. Because of velocity changes, ray path refraction occurs.*

5. CAN NATURAL AND INDUCED SEISMICITY UNAMBIGUOUSLY BE DISCRIMINATED ?

5.1 INTRODUCTION ON INDUCED EARTHQUAKES

A large part of this section summarizes Chapter 5 in *Induced Seismicity Potential in Energy Technologies* (Council, 2013).

It has long been understood that earthquakes can be induced by impoundment of reservoirs, surface and underground mining, withdrawal of fluids and gas from the subsurface, and injection of fluids into underground formations. In stable continental interiors, far from tectonic borders, the induced seismic hazard could become at least equally important as the natural seismicity, particularly in regions where there is a lack of previous seismic activity (Camelbeeck *et al.*, 2019).

The Earth's crust is crossed by a network of pre-existing fractures and faults of various sizes. Any of these faults could in principle be reactivated if the shear stress (τ) acting on the fault overcomes its resistance to slip or movement of the adjacent crustal blocks. In most cases, the shear resistance (or shear strength) is related to friction. In other words, the shear strength is proportional to the difference between the normal stress[5] (σ_n) acting on the fault and the pressure (Pf) of the fluid permeating the fault and the surrounding rock. The fault remains stable, i.e., does not slip, as long as:

$$\tau < \mu_s(\sigma_n - Pf) = \mu_s\sigma'_n$$

where τ is the shear stress and $\mu_s\sigma'_n$ is the frictional strength.

The conditions for slip are met when:

$$\tau = \mu_s(\sigma_n - Pf).$$

The term $(\sigma_n - Pf)$ is called the effective stress σ'_n. The symbol μ_s represents the dimensionless static friction coefficient, a parameter that varies only in a narrow range, typically between 0.6 and 0.8 for most rock types. However, μ_s is the most difficult parameter to determine adequately.

The key parameters controlling the initiation of slip are the normal (σ_n) and shear stresses (τ) acting on the fault and the pore fluid pressure (hereafter simply referred to as "pore pressure" or P_f). The normal and shear stresses on the fault depend on the orientation of the fault and on the stress state at depth (Figure 39). Due to the weight of the overburden and other processes in the Earth's crust, rocks are under compression. The compressive normal stress at depth varies with direction; this variation of the normal stress with direction is linked to the shear stresses that are responsible for slip along a fault if the frictional resistance of the fault is overcome. In contrast, for a fluid at rest, the state of stress is hydrostatic: the normal stress is the same in all directions, and it cannot transmit any shear stresses.

The effective stress state at a point in the Earth involves both the stress tensor and the pore pressure. The stress tensor is described by the vertical stress (σ_v) and the minimum and maximum horizontal stresses (σ_h and σ_H) that act in two orthogonal directions. The direction of σ_H, as well as the relative values of σ_v, σ_h, and σ_H, control the orientation of the fault most likely to slip. Three different fault regimes, that is, normal, thrust or strike-slip, are defined depending on the relative magnitude of σ_v, σ_h, and σ_H. Once the most critical fault orientation has been identified, the normal and shear stresses acting on the fault can in principle be computed from the effective stress state.

[5] This normal stress comprises the lithostatic effect and the tectonic load.

Determination of the in-situ stress state is complex and often expensive. Consequently, the information on the in-situ stress in the Earth is usually too fragmentary to allow confident estimates of the actual stresses acting on a fault. In most cases, the only reliable information available is the magnitude of the vertical stress, as it can be calculated from the average density of the overlying (water-saturated) rock column and the depth. Estimating the general fault types and configurations as well as the broad orientation of the maximum and minimum horizontal stresses at a scale of tens or hundreds of kilometres is also sometimes possible, based on a variety of stress indicators.

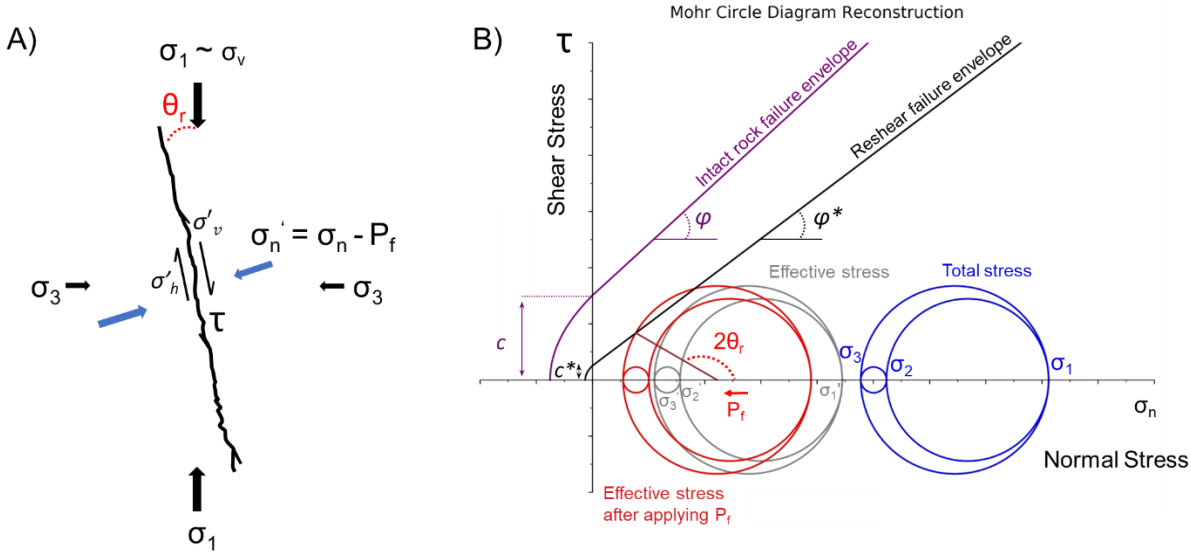

Figure 39: A) *Cross-section overview of parameters playing a role on fault reactivation. Pf: Fluid pressure; σ_n: normal stress; σ_n': effective normal stress.* θ_r*: angle between the maximal principal stress (σ_1) and the fault plane.* ***B)*** *Mohr circle diagram reconstruction of an existing fracture plane (brown line) that is brought to failure because of an applied Pf. c (c*): cohesion along a new (pre-existing) fracture. φ (φ*): angle of internal friction for a new fracture (or along a pre-existing plane).*

In contrast to the difficulty of determining σ_h and σ_H and their orientations, the undisturbed initial pressure of the fluid permeating the rock and fractures or faults can usually be reliably estimated from the depth of the rocks, under normally pressurized conditions. Techniques also exist for direct measurement of the pore pressure from a well.

However, physics-based models require detailed information about subsurface fluid flow and geomechanical properties (Verdon *et al.*, 2019). The development of physics-based models can be time-consuming, meaning that results are not available in a time frame that is relevant to operators, regulators, or the concerned public. Moreover, the results of geomechanical models can be very dependent on a selection of model input parameters, which may not be well constrained. Consequently, user-defined choices of input parameters may introduce biases into the physics-based modelling approach that are difficult to quantify. Indeed, given that it is common practice to "tune" the input parameters of geomechanical models such that they reproduce geophysical observations including induced seismicity (e.g., Verdon *et al.*, 2015, 2011), it is arguable whether a geomechanical model can ever be entirely free from biases introduced by user-input choices.

Although the conditions for initiating slip on a pre-existing fault are well understood, the difficulty remains to make reliable estimates of the various quantities in the Mohr-Coulomb failure criterion. This criterion represents the linear envelope that is obtained from a plot of the shear strength of a material versus the applied normal stress (see Figure 39). Lacking these estimates, predicting how close or how far the fault system is from instability remains difficult, even if the orientation of the fault is known. This implies that the magnitude of the increase in pore pressure that will cause a known fault

to slip cannot generally be calculated. Based on geomechanical parameters estimated for rock laboratory tests and drilling test, the stress state and its changes due to fluid pressure increase can at best be visualised in a Mohr Circle diagram (see Figure 39). Using Mohr Circles, one can theoretically calculate the necessary fluid pressure to bring a fault to failure. However, as stated in Section 3.1, even if this fluid pressure estimate is correct, it only indicates that a rupture is possible at one point. It does not tell anything about the way the rupture may propagate. It remains a quite challenging question in seismology to understand why ruptures propagate or not, and how far. This depends on fault geometry, friction, the stress state, or the presence of asperities and roughness of the pre-existing fault. In other words, it seems that there is presently no way to distinguish the initiation processes of small and large earthquakes (Kanamori, 1996; Meier *et al.*, 2016).

Nonetheless, understanding how different factors contribute to slip initiation is valuable because it provides insight about whether fluid injection or withdrawal may be a stabilizing or a destabilizing factor for a fault; in other words, whether fluid injection or withdrawal causes the difference between the driving shear stress and the shear strength to increase or decrease. Any perturbation in the stress or pore pressure that is associated with an increase of the shear stress magnitude and/or a decrease of the normal stress and/or an increase of the pore pressure could be a destabilizing factor; such a perturbation brings the system closer to critical conditions for failure. A large body of evidence suggests that the state of stress and pore pressure are often not far from the critical conditions where a small destabilizing perturbation of the stress and/or of the pore pressure could cause a critically oriented fault to slip (Zoback and Zoback, 1980, 1989).

Note that the common concept that *"injected fluids cause earthquakes by lubricating underground faults"* is not accurate because fluids do not decrease the coefficient of friction. Rather, injected fluids or extracted fluids cause earthquakes by changing the stress conditions at faults, bringing these stresses into a condition where driving stresses equal or exceed resistive stresses, thereby promoting slip on the fault (Induced Seismicity Potential in Energy Technologies, 2013).

Unfortunately, despite our understanding of the factors affecting the initiation and the magnitude of a seismic event, the values of the process parameters, such as the injection rate or the volume of fluids injected, that will trigger the seismic event and what magnitude the event will be are generally not possible to quantify. The inability to make these kinds of predictions is due to several factors:

1. Fragmentary knowledge of the state of stress in the Earth;
2. Lack of knowledge about the faults themselves, including their existence if they have not yet been correctly mapped, their orientations and physical properties such as the stress state, or the presence of asperities;
3. Difficulty in collecting the basic data (hydraulic and mechanical parameters, the geometry of the geological structure, such as the reservoir) that are required to calculate the pore pressure and stress change induced by the fluid injection or withdrawal.

Nonetheless, the insights into the mechanisms causing seismic events allow us to make some broad conclusions. In processes involving fluid injection, the pore-fluid pressure increase is the dominant factor to be considered to change stress at the local level in the short duration of a geothermal project. Any increase of the pore pressure above historical undisturbed values may bring the system closer to critical conditions. The probability of triggering a significant seismic event increases with the volume of fluid injected: the larger the volume injected, the more likely a larger fault will be intersected. However, injection of fluid in depleted reservoirs (such as in secondary recovery stimulation—waterflooding) is unlikely to create an earthquake, irrespective of the volume of fluid injected, if the pore pressure remains below pre-production values.

For deep geothermal operation, three processes can trigger earthquakes:

1. Increase in pore pressure, which may fracture the bedrock (this is the case when stimulation is being performed), or weaken the shear (the pore pressure is the pressure at which the fluid contained within the pore space of rock is maintained at depth. In the absence of any other processes, the pore pressure is simply equal to the weight of the overlying fluid, in the same way that the total vertical stress is equal to the weight of the overlying fluid and rock. This pressure is often referred to as the "hydrostatic pressure.").
2. Rock cooling: thermomechanical stress may trigger earthquakes. This may occur in case of thermic stimulation, in order to favour fluid circulation.
3. Fast pressure drop, this could happen if no fluid is re-injected into the reservoir.

It is not easy to assess the overpressure that should not be overpassed. It is site-dependent. Evans *et al. (*2012) investigated 41 geothermal sites in Europe and concluded that the most important seismicity was observed where the crust was critically stressed, given the local tectonic context. Hence, there might be a link between induced seismicity and tectonic context, but this hypothesis is debated (Giardini, 2009; Majer *et al.*, 2007; Rivas *et al.*, 2005; Ungemach *et al.*, 2005).

We must also keep in mind that earthquakes often strike a long time after the injection processes. In Basel (CH), the felt events occurred 0.2 to 56 days after the stimulation. This is also the case at the Balmatt site: 2.5 days to three weeks after injection stopped. A possible explanation would be the time necessary to diffuse the pore pressure from the injection point to existing, potentially unknown faults, further away (Bachmann, 2011).

General recommendations from the literature:

1. Keep the injected fluid pressure underneath a given threshold, which needs to be determined at each site and which can be preliminarily calculated using a Mohr Circle reconstruction. Distributing the injection throughout different boreholes may help (Gombert *et al.*, 2017);
2. Setting up a seismic monitoring network, allowing real-time monitoring;
3. Inform population and local authorities on the ongoing operation and possible related seismic hazard. Let us quote (Giardini, 2009): "***The public reacts with a vengeance if it perceives that a known problem has been hidden. More than this, earthquakes invariably raise primordial fears. Waking up the sleeping terror that lurks in the deep is the plot of numerous horror movies; here it has an all-too-real meaning***".

5.2 DISCRIMINATING INDUCED AND NATURAL EARTHQUAKES

To discriminate seismicity induced by industrial activities from natural earthquakes, Verdon *et al.* (2019) propose a framework to evaluate questions related to seismicity and the local geological conditions in which seismicity occurs. Based on the outcome, a matrix score is calculated allowing evaluating the origin of seismicity. The authors describe the limitation of previous frameworks, and propose an improved way to assess induced seismicity, taking into account uncertainties, allowing some questions to remain unanswered in the matrix, and easier to interpret by the public and stakeholders. The new scheme allows distinguishing between a case in which the outcome of the assessment is neutral because of a lack of reliable evidence and a second case for which data are available but nonetheless the conclusion is ambiguous. These two cases are quite distinct from operational and regulatory perspectives, especially because the conclusion in the former case may change as data become available.

The authors propose assigning numerical scores to questions, with positive values for answers that support induced seismicity. The score values available for each question reflect the relative importance

of the different questions, and for each question, the absolute value of the score is modulated according to the degree of uncertainty, which may be difficult to assess. The outcome is a score, the induced assessment ratio (IAR), either positive, negative or zero, that reflects whether events were induced or natural. A second score, the evidence strength ratio (ESR), is assigned that characterizes the strength of the available evidence, expressed as the ratio of the maximum score possible with the available evidence relative to the maximum score that could be obtained if all desired data were available at a site. The assessment framework also allows incorporating easily new knowledge, noting that today, the science around induced seismicity is a highly active one.

We detail here the framework, and apply it to the Balmatt case, as an example.

The **evidence strength ratio (ESR)** describes the quality and quantity of information used in the assessment. ESR is the ratio of the maximum score that can be assigned with the available data to the maximum score that would be available in an ideal case with all desirable data fully available:

$$ESR = \frac{(|Maximum\ neg.points\ given\ available\ data| + |Maximum\ pos.points\ given\ available\ data|)}{Total\ number\ of\ positive\ and\ negative\ points\ that\ can\ be\ scored\ in\ the\ framework} \times 100$$

$$= \frac{(|Maximum\ neg.points\ given\ available\ data| + |Maximum\ pos.points\ given\ available\ data|)}{96} \times 100$$

The number 96 in the denominator is the total number of positive and negative points that can be scored in the framework. The ESR can be revised when more data are available.

The **induced assessment ratio (IAR)** categorizes the conclusion regarding the origin of the seismicity inferred from the available data. If the judgment of the assessor is that there is ambiguity or uncertainty in the available information (e.g., poorly constrained focal depths), then this judgment may be expressed as a percentage and then applied to the available scores.

The IAR quantifies whether the overall assessment indicates a natural or an induced cause. The total number of points scored across each criterion, combining both positive and negative values, is divided by the maximum points that could have been scored if all answers were positive (if the summed score is positive) or negative (if the summed score is negative):

$$IAR = \frac{Summed\ score}{Maximum\ points\ given\ the\ sign\ of\ the\ score\ and\ given\ available\ data} \times 100$$

Hence, a negative IAR supports a natural origin, and a positive score an induced origin. An IAR close to zero should be interpreted as an ambiguous assessment, and a low ESR indicates that the IAR is based on insufficient data. A low IAR score with an ESR of 80% would suggest that we are unlikely to be able to know whether a particular seismic sequence was due to an industrial process or not. Of course, during the industrial activity, additional observations and data can change the outcome and the exercise should be re-evaluated during the course of an industrial project or after recurrent seismicity.

Question list based on Verdon *et al.* (2019):

1) Has there been previous (either historical or instrumental) seismicity at the same site, or within the same regional setting?
   a) Earthquakes have previously occurred in the vicinity to the site, with similar rates and magnitudes: **–5**.
   b) Earthquakes have previously occurred within the same regional setting, with similar rates and magnitudes: **–2**.
   c) Earthquakes have not occurred at similar rates or magnitudes within the regional setting: **+5**.
   d) Past earthquakes occurred at similar depths within the regional setting: **–3**.

   e) Earthquakes are significantly shallower than any past events that have been observed within the regional setting: **+3**.
2) Is there a temporal coincidence between the onset of events and industrial activities?
   a) The earthquake sequence began prior to the commencement of industrial activity: **−15**.
   b) The earthquake sequence did not begin until a significant period of time after the cessation of industrial activity: **−5**.
   c) The earthquake sequence began while the industrial activity was ongoing: **+5**.
3) Are the observed seismic events temporally correlated with the injection or extraction activities?
   a) The earthquakes are coincident with the industrial activity, but there is a minimal correlation: **−4**.
   b) There is some temporal correlation between the seismicity and the industrial activity: **+4**.
   c) There is a strong temporal correlation between the seismicity and the industrial activity (e.g., between rates of injection and rates of seismicity): **+15**.
4) Do the events occur at similar depths to the activities?
   a) Earthquakes do not occur at the same depth, and there is no plausible mechanism by which stress or pressure changes could be transferred to these depths: **−4**.
   b) Earthquakes do not occur at the same depth, but plausible mechanisms exist by which stress or pressure changes could be transferred to these depths: **+2**.
   c) Earthquakes occur at similar depths to the industrial activity: **+3**.
5) Is there spatial collocation between events and the activities?
   a) Earthquakes are distant to the activities, given the putative causative mechanism: **−10**.
   b) Earthquakes are sufficiently close to the activities, given the putative causative mechanism: **+5**.
   c) If earthquake loci change with time, this change is consistent with the industrial activity, for example, growing radially from a well or shifting in response to the start of a new well: **+10**.
6) Is there a plausible mechanism to have caused the events?
   a) No significant pore-pressure increase or decrease occurred that can be linked in a plausible manner to the event hypocentral[6] position: **−5**.
   b) Moderate pore-pressure or poroelastic stress change occurred that can be linked in a plausible manner to the event hypocentral position: **+2**.
   c) A large pore-pressure or poroelastic stress change occurred that can be linked in a plausible manner to the event hypocentral position: **+5**.
7) Do the source mechanisms indicate an induced event mechanism?
   a) The source mechanisms are consistent with the regional stress conditions: **0**.
   b) Source mechanisms are not consistent with the regional stress conditions but are consistent with a putative causative mechanism (e.g., thrust faults above a subsiding reservoir): **+4**.

The total scores range -46/+50, that is, the smallest or largest possible values in the denominator of IAR.

5.3 Application on the Balmatt case

In this section the different questions are described in more detail and are afterwards applied to the Balmatt case (in blue) using available evidence and information.

[6] The hypocentre, or focus, is the point of origin of the earthquake. The epicentre is its projection at the Earth surface.

Disclaimer: This exercise is performed to our best knowledge of current data and should not be considered as final. It would benefit from a more comprehensive analysis.

(1) Previous seismicity

The quality of past monitoring arrays deployed in the area must be taken into account when performing this assessment (see Section 3.1). Improved seismic network coverage may produce an illusion of an increased seismicity rate that is in fact simply the product of improved detection threshold. The lack of sufficient network coverage to adequately characterize the baseline seismicity is a key reason why this question may not be answerable with sufficient certainty. The definition of the area of interest, both laterally and in-depth is also not trivial. For obvious reasons, past seismicity in the same location is a strong indication that seismicity is natural. However, the area that should be considered relevant in such an assessment is somewhat subjective (does the activity belong to the same tectonic setting or play?), and so there is no definition of a radius of consideration based on distance.

Given that most industrial activities take place at relatively shallow depths, most cases of induced seismicity occur at relatively shallow depths when compared to the overall seismogenic thickness of the crust, which typically extends 20-25 km in depth in Flanders. Therefore, the occurrence of seismicity at relatively shallow depths, if past natural seismicity has not previously occurred at such depths, may be taken as an indicator that events are induced. However, in many cases it is not possible to make this assessment because event depths for past seismicity are very poorly constrained and in some cases, the depths of the candidate events are also poorly constrained. In that case, this element of the question cannot be answered.

A score of −2 may be awarded if the response is that there are epicentres of natural earthquakes in the same regional tectonic setting, −5 if previous natural events occurred relatively nearby to the site in question, but +5 if there have not been previous earthquakes of similar magnitude or rate. An additional -3 or +3 points can be added if previous event depths are well constrained.

Evidence assessment

Table 10 provides the magnitudes, depths and precision of the horizontal and vertical location of the 4 largest events that were recorded less than 3 km from the Balmatt injection well, and are supposedly induced. The location precision increases with magnitude, as the signal to noise ratio increases, making the signal easier to measure, also revealing it in more stations. For the M_L 2.1 event, including the network of VITO (RETVK, RETVG, MOL2A, DSLNZ stations) does not improve significantly the precision, as shown by the values in brackets in the table below.

Table 10: *Date, magnitude, depth and precision on the horizontal and vertical position of the hypocentre of the largest Balmatt events. The values in brackets provide the precision when the 5 stations of the local VITO network are included in the computation.*

Date	ROB M_L	Depth	Horizontal precision	Vertical precision
2016-10-03	0.9	6.4 km	2.8 km	1.9 km
2018-12-18	1.2	4.9 km	2.0 km	1.5 km
2019-01-18	1.5	5.9 km	1.8 km	1.2 km
2019-06-23	2.1	4.0 km	0.8 km (0.7)	0.4 km (0.4)

According to the seismotectonic model of Belgium, the Balmatt site is situated in the Eastern Campine Zone (ECZ, see chapter 4 in VLA07-4.2 report), a narrow NW-SE oriented zone in between the Anglo-Brabant Massif to the west and the Roer Valley Graben to the east. The three largest events near

Balmatt had magnitudes between M_L=1.2 and M_L=2.1. Earthquakes similar in size or larger are not uncommon in this zone. However, the rate of $M_L \geq 1.2$ earthquakes in the entire zone is ~0.57/yr since 1985, whereas there were 3 events of that size around Balmatt in only half a year (and the geothermal plant was not operational the whole year). In addition, most earthquakes in the ECZ are situated in the southern part of the zone. If we consider all seismicity in a radius around Balmatt (Table 11), only 3 tectonic earthquakes occurred in a radius of 30 km. The nearest of those is situated at a distance of 24.7 km and had a magnitude M_L=1.2 and all three are associated with the Roer Valley Graben.

Table 11: *Parameters of tectonic earthquakes that are situated closest to Balmatt.*

Date	Locality	M_L	Lon (° E)	Lat (° N)	Depth (km)	Vertical precision (km)	Distance (km)
1986-11-28	PEER	1.2	5.441	51.140	11.8	2.7	24.7
1990-07-18	HILVARENBEEK (NL)	2.5	5.228	51.493	10.0	2.82	29.3
1990-08-12	HAMONT	2.6	5.526	51.219	4.2	4.28	28.2

Although the completeness magnitude of the ROB catalog is relatively high (M_W=1.8, see Section 2.2), it should be noted that the nearest stations of the Belgian seismic network are located in Mol (MOLT, MOLS) and in Dessel (DSLS, DSLB). These stations are only ~4 km away from the injection point and have been recording for about ten years. Between June 2008 (installation of the seismometers) and September 2016 (first injection), no events comparable to the 3 largest ones in Table 10 were monitored. According to our analysis of the detection capability (see Section 3.1), any earthquake with M_L larger than the range 1.2 to 1.5 should have been detected by routine monitoring with these stations.

The ROB catalog also allows assessing whether the Balmatt seismicity is more shallow than the natural seismicity. Although most natural seismicity is concentrated between 5 and 20 km depth, the ROB catalog does contain earthquakes with depth shallower than 5 km (Figure 40, left). However, these are mostly limited to areas of known shallow seismicity (possibly related to past mining activity) such as the Hainaut and Liège zones. If we consider only earthquakes that are situated in the Eastern Campine Zone and have a well-constrained focal depth (vertical precision better than 2.5 km), zero events out of 10 ($M_L \geqslant 1.5$) are shallower than 5 km, while some events originate even deeper than 20 km (Figure 40, right). It thus appears that Balmatt seismicity is rather shallow compared to past events in the same regional setting. However, the number of observations is relatively low.

In summary, earthquakes have previously occurred within the same regional setting, but likely with a lower rate. The Balmatt events appear to be shallower than past events observed in the regional setting. Therefore, we can compare not only magnitude and rates but also depths of past events. The answer rating, i.e., the degree of certainty, is 100%. The maximum points scorable for ESR are −8 or +8.

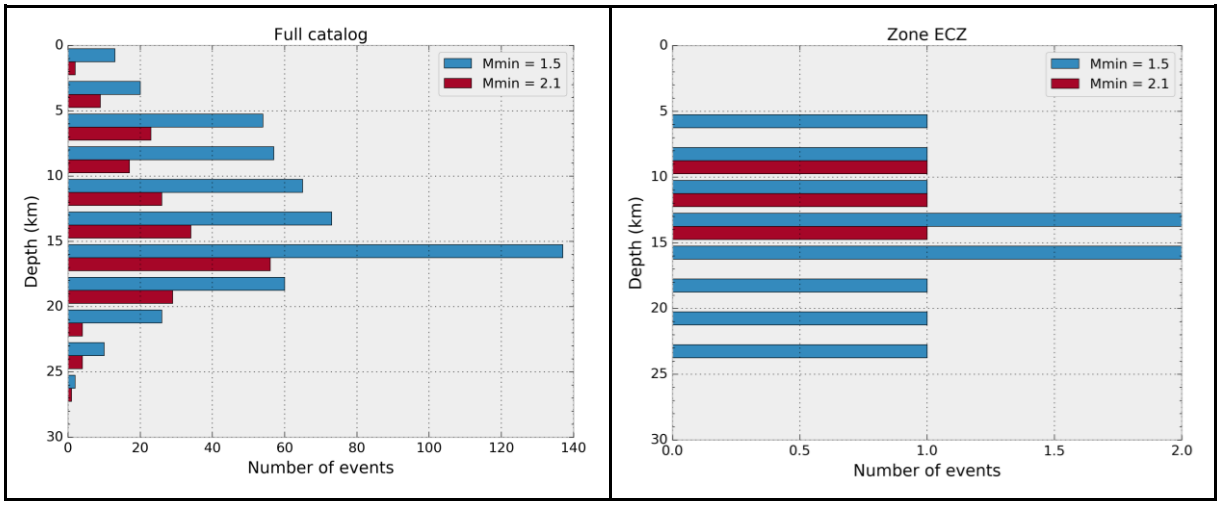

Figure 40: *Depth histograms of well located (depth uncertainty < 2.5 km) tectonic earthquakes with different minimum magnitudes.* ***Left:*** *full ROB catalog;* ***Right:*** *Earthquakes in the same seismotectonic zone (ECZ = Eastern Campine Zone) as Balmatt.*

Answer: Earthquakes have not previously occurred at this site. However, earthquakes with similar magnitudes have occurred in the same seismotectonic zone. Although these likely occurred with lower rates, some uncertainty remains due to the relatively high completeness magnitude of the earthquake catalog. Hence, as a conservative assessment, we attribute a score of -2, which could increase to +5 in the future if the seismicity rates can be calculated more robustly. The events also seem to occur significantly shallower than other earthquakes in the same zone: +3. Total: +1.

(2) Temporal coincidence between the onset of events and industrial activities?

This question is usually answerable with relatively high certainty because it requires knowledge only of the dates when the industrial site was operating and the dates of the seismic events. Verdon *et al.* (2019) are not aware of any cases of induced seismicity where no events occurred during activities but began after they stopped.

A negative answer provides the largest weight favouring natural seismicity: -15.

Evidence assessment: Application of the template matching technique to station MOLT, DSLS, DSLB (see Figure 17, Section 2.4) did not detect any event weakly similar to the reference template near the Balmatt location in the eight months preceding the first injection. we know exactly when the operator started injecting water. The first earthquakes around Balmatt started after the first injection tests in September 2016, and again after the start of operation in December 2018. The answer rating is 100%. The maximum points scorable are -15 or +5.

Answer: Our analysis in Section 2.4 clearly demonstrates that the onset of events was temporally coincident with the industrial activity: +5.

(3) Temporal correlation between seismicity and the ongoing industrial activities?

A positive answer to this question provides the largest weight favouring the induced seismicity: +15. By correlation, we do not just mean that the occurrence of events overlaps with the industrial activity (see question 2), but that changes in the rate of seismicity are temporally correlated with changes in the rate of industrial activity (e.g., the rate of fluid injection or removal). This correlation may be expressed quantitatively as a correlation coefficient between the two rates (e.g., Oprsal and Eisner, 2014), but may in some cases be examined qualitatively, for example, that events occur when injection starts and stop when injection stops.

Evidence assessment: With detailed pumping data provided by the operator, and an improved catalog provided by the matched-filter detection method, it should be possible to assess the correlation between the induced events and the activity in detail. The ROB does not have the pressure/temperature/volume data of the injection, but according to VITO (slides shown during the VITO meeting with VPO, FANC and ROB on 2019-02-08 in Berchem), there is a "strong correlation between seismicity and operational conditions (injection pressure and temperature)". Answer rating is 100% taking the VITO information as granted. The maximum points scorable are −4 or +15.

Answer: The analysis in Section 2.4 suggests a good correlation between seismicity and industrial activities, but considering that the ROB does not have access to all the operational data, we currently assign a score of +4. This could increase to +15 in the case those data are correlated with the bursts of activity identified in Section 2.4.

Remark: let us quote Hicks *et al. (*2019): "*as operations continue in the long term, we recommend seismic monitoring close to hydrocarbon development and production sites, and high-resolution reporting of operational activities (e.g., well shut-in periods, production volumes, and rates) that is visible to the public*".

(4) Do the events occur at similar depths to the activities?

This assessment can be complicated by the fact that many cases of induced seismicity have in fact occurred several kilometres deeper than the industrial activity (e.g., Verdon, 2014). These observations are explained by the presence of hydraulic or geomechanical connections, usually faults, from shallow to deeper layers (e.g., Ellsworth, 2013). If events occur at the same depth as the industrial activity, then we consider this to be evidence that they are induced.

Balmatt Case: In the Balmatt case, we, fortunately, benefit from seismic stations that are sufficiently close to the injection point. This was already the case before VITO installed the monitoring network, as we already benefited from the seismic stations in Mol (MOLS, MOLT) and Dessel (DSLS, DSLB), 4 km away from the injection point.

Evidence assessment: With an uncertainty smaller than 2 km (0.4 km for the largest event; see Table 10), we can confidently assess the events are at a similar depth to the operations. Answer rating is 100%. The maximum points scorable are -4 or +3.

Answer: The determined hypocentral depths (see Table 10) confirm that the events occur at similar depths to the industrial activity: +3.

(5) Spatial collocation between events and the activities?

The spatial collocation between industrial activities and seismic events is of obvious significance. The distances at which events might be considered to be induced will vary depending on the type of industrial activity under consideration. Seismicity associated with hydraulic fracturing typically occurs within 1 km of the well. Seismicity associated with fluid extraction and subsidence typically occurs within, or at the edge of, the footprint of the depleting reservoir. Larger distances between events and high-volume injection wells (e.g., >10 km) are indicative of a natural cause unless there is also some seismicity located in closer proximity to the well. Changes in location with time may also be a useful indication that events are induced. For example, events might be expected to migrate radially from an injection well with time (e.g., Shapiro, 2008) or along a line following a fault. If the locus of operations changes (e.g., new wells are drilled), then corresponding changes in the loci of seismicity would provide strong evidence that events are induced. The largest source of uncertainty that affects this question is with respect to event locations. In Belgium, most events since 1985 with magnitude larger than M_L = 1.5 are located with an average horizontal precision of 1.7 km (Figure 41). To provide an accurate event

depth determination, a good velocity model is required and at least one seismometer should be installed at a distance smaller than twice the depth of the hypocentre. At Balmatt, this means 7 km.

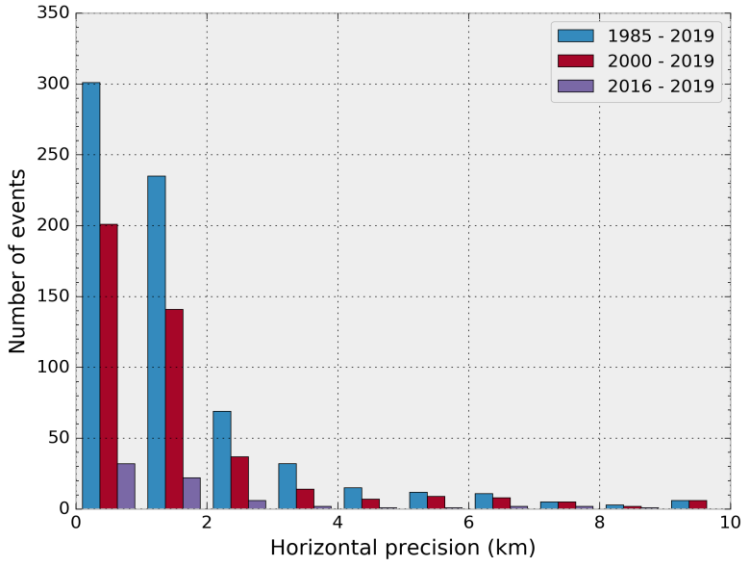

Figure 41: *Histogram showing horizontal precision of tectonic earthquakes in Belgium for different time periods*

Evidence assessment: Based on the location provided on the seismometer network website of VITO, the hypocenters are located along a 1 km long line from the injection point. These events are the only seismicity near Balmatt. The local monitoring network allows for a precise relative location between events. The absolute location is not better than a few hundreds of meters, but this can be improved if one considers that the first induced 2018 event is located at the injection point. This is the strong hypothesis used for the absolute locations listed on the website of VITO.

Migration due to changes in the response to the start of a new well has not been observed so far, because there is only one injection well at present. This could change in the future, e.g., with the tests planned at MOL-GT3.

Answer rating is 100%. The maximum points scorable are −10 or +10.

Answer: Earthquakes occurred at 1-3 km from the injection well (absolute location): +5 (if VITO confirms a migration consistent with the injection, then the score increases to +10).

(6) Is there a plausible mechanism?

Mechanisms of induced events typically invoke three phenomena:

a. An increasing pore pressure reducing the normal stress acting on a fault, thereby enabling slip (see Figure 39 in Chapter 6);
b. A decreasing pore pressure causing reservoir compaction and geomechanical deformation in the surrounding rocks (e.g., Segall, 1989);
c. Poroelastic stress transfer causing an increase in the Mohr-Coulomb rock failure criteria (CFS; e.g., Deng *et al.*, 2016).

There are asymmetries between these mechanisms: small increases in pore pressure (e.g., Cesca *et al.*, 2014) or small positive increases in CFS (Deng *et al.*, 2016) have been observed to be sufficient to induce seismicity, whereas comparatively large pore-pressure decreases are required before compaction-induced seismicity occurs (e.g., Bourne *et al.*, 2014).

Verdon *et al.* (2019) propose 3 cases:

1. There is no pore-pressure or a positive CFS change;

2. There is a moderate pore-pressure or a positive CFS change;

3. There is a pore-pressure or a positive CFS change.

To reflect the asymmetry, Verdon *et al.* (2019) suggest that a one considers a large pore-pressure change if one observes an increase in pore pressure or a positive CFS change > 1 MPa, or a decrease in pore pressure of > 5 MPa. A pore-pressure change is moderate for an increase of > 0.1 MPa or a decrease of > 1 MPa. Additionally, it is required that a plausible mechanism exists capable of transferring pore-pressure changes to the hypocentral locations.

This plausible mechanism question may often be difficult to answer because it requires that the pressure changes and poroelastic effects caused by the industrial activity are known or can be modelled. Borehole pressures are often not publicly available (such data are often commercially sensitive), and accurate models require detailed subsurface characterization. To determine whether it is plausible that pressure changes reached the hypocentral locations, these locations must be well constrained both laterally and in-depth, which also may not be the case. The above mentioned pore-fluid pressures are pressures at depth within the reservoir. Measuring the fracture pressure at depth is an extremely challenging technical task. Without active pressure measurements, fracture pressure can be estimated by calculating the pore-fluid pressure using available geological, depth and reservoir data and reconstruct it in a Mohr Circle diagram. Once the reservoir's fluid pressure is calculated, one can discuss the maximum allowed fluid overpressure invoked by fluid injection. However, the fluid pressure injected at the surface at the wellhead increases at depth due to several factors that need to be taken into account to properly evaluate potential fault reactivation. New initiatives should always try to present arguments to justify the injection pressure they are going to initially use.

Evidence assessment: The example below uses available data applicable for the Balmatt site and shows the different conditions to reactivate a structure at depth. These Mohr circle reconstructions result from collaboration with H. Van Baelen (ONDRAF-NIRAS; Van Baelen *et al.*, 2019) and differ from the initial Mohr-Circle analysis performed by Broothaers and Laenen (2012).

σ_V and σ_V' are calculated based on the depth and on average rock and water densities as indicated in Table 13. The water column is considered to be as high as the injection depth and is added to the computation. The effective horizontal stress σ_H' is calculated using the Earth pressure coefficient and K_0. K_0 is difficult to measure, but it can be estimated based (i) on the Poisson's ratio, (ii) on the angle of friction using values in Table 13, or (iii) using a fixed value (here 0.35). To construct a failure envelope, two cases can be considered: one for intact rock and another for reshear (i.e., shear on an existing fault; Figure 42). Given that Balmatt is situated in a tectonic area where normal faults are present in the reservoir, the reshear failure envelope is plausible to represent rock failure for normal faults. To plot the failure envelopes, a theoretical nominative friction angle of 32.5° and cohesion of 2.5 MPa was used for the Coulomb (compressive) and Griffith (extension) criteria. For the effective stresses reduced by injection pressure (σ_V'' and σ_H''), a brine fluid density of 1.15 g/cm³ is used.

The Mohr circle reconstruction shows that for a perfectly favourably oriented fault (i.e., $\theta = 90° - \varphi^*$, see red line in Figure 42) reactivation is met at an injected wellhead fluid pressure of 3.1 MPa (Pf_i) which increases up to 7.1 MPa at depth (Pf_d). It should be noted that this is a simplistic 2D situation with σ_V larger than $\sigma_{H,h}$ but without any difference between horizontal stress so that $\sigma_H = \sigma_h$. A more careful evaluation should be performed to investigate the actual 3D situation with $\sigma_1 \sim \sigma_V$, $\sigma_2 \sim \sigma_H$ and $\sigma_3 \sim \sigma_h$ and in which a specific fault plane can be investigated (e.g., a fault plane resulting from the focal mechanism analysis). However, such a 3D situation cannot be investigated beforehand.

Table 12: *Parameters, and their abbreviation, necessary to estimate pore-fluid pressure.*

d	depth of injection well	[m]
h	in situ hydraulic head of target (ref. ground level)	[m]
A	reference surface (1 m^2)	[m^2]
g	gravitational acceleration (9,81 m/s^2)	[m/s^2]
σ_h / σ_v	total horizontal / vertical stress, in situ	[MPa]
σ'_h / σ'_v	effective horizontal / vertical stress, in situ	[MPa]
σ''_v	effective vertical stress during injection	[MPa]
$\sigma''_{h:}$	effective horizontal stress during injection	[MPa]
$\overline{\rho_{bulk\ dry\ rock}}$	average dry bulk density of rock	[kg/m^3]
$\overline{\rho_{water}}$	average water density over saturated thickness	[kg/m^3]
ρ_{brine}	density of reinjected brine	[kg/m^3]
K_0	lateral earth pressure coefficient at rest	[-]
ν	Poisson's ratio – material constant	[-]
φ	angle of internal friction, intact material	[°]
Pf_i	injection pressure at the well-head	[MPa]
T	tensile strength of intact material	[MPa]
c, c*	cohesion of intact material / pre-existing fracture	[MPa]
φ*	angle of internal friction along an existing plane	[°]

Table 13: *Range of parameter values and nominative values used for the Mohr circle reconstruction. Source: Van Baelen et al. (2019).*

Parameter	Range	Nominative Value	Argumentation
D	3000 - 4500 m	3600 m	Depth range of injection (source: VITO)
H	-20m - +100m	0 m	Hydraulic head
$\overline{\rho_{bulk\ dry\ rock}}$	2200 – 2600 kg/m³	2300 kg/m³	Estimated rock density, eq. Porosity 5-20%
$\overline{\rho_{water}}$	1000 – 1080 kg/m³	1040 kg/m³	Maximal density based on a linear diffusive profile
ρ_{brine}	1050 - 1200 kg/m³	1150 kg/m³	Water density at 18 MPa (mean pressure in a water column) at 60°C (= injection T; VITO) and with ~165g salt /l (Bos and Laenen, 2017)
K_0	0.2 – 0.5	0.35	Poisson's ratio and internal friction angle
ν	0.15 – 0.35	0.26	Limestone/Shale values from literature; input for K_0
φ	35° - 50°	42.5°	Limestone/Shale values from literature
c, c*	10 – 20 MPa	15 MPa	Based on tension strength of sedimentary rock
φ*	25° – 40°	32.5°	Not much info in literature; chosen arbitrarily at 10° less than intact rock
c*	0 – 5 MPa	2.5 MPa	Not much info in literature; chosen arbitrarily at half the value of intact rock
Pf_i	0-15 MPa	Value to decide	Deriving Pf_i Is the goal of this exercise

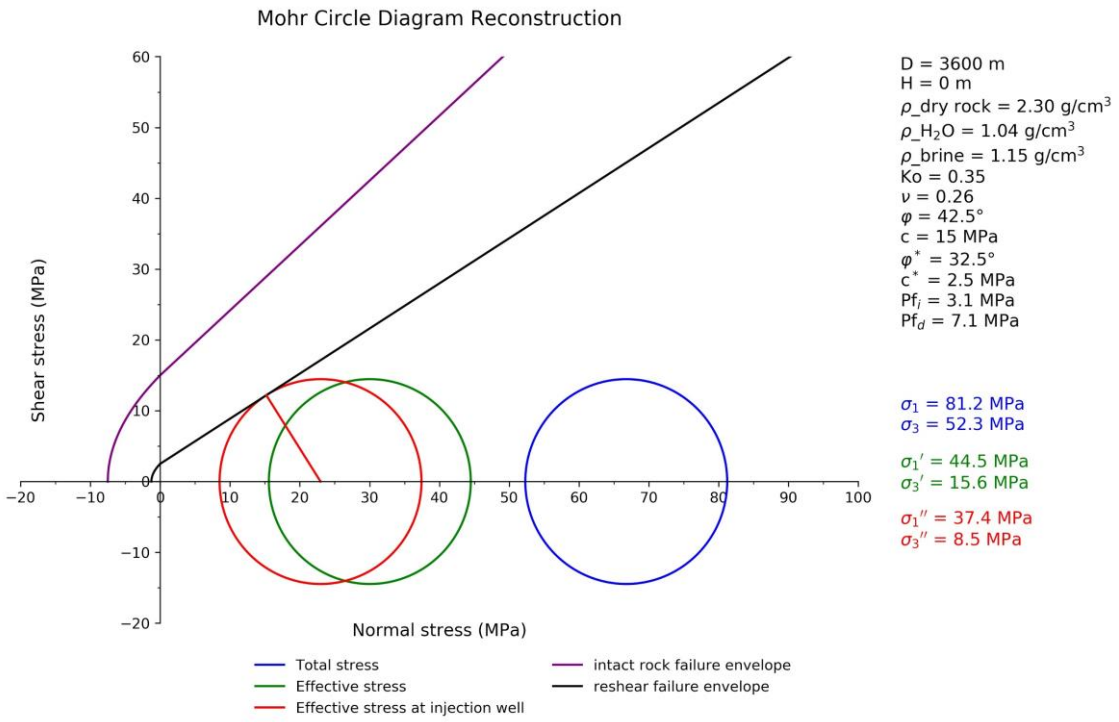

Figure 42: *Mohr circle reconstruction of stress conditions to reactivate an optimally oriented fault (red line) with the given parameters. Pf_i = injected fluid pressure at the wellhead. Pf_d = calculated fluid pressure at the injection point at depth.*

Information from VITO, however, showed that the injected pressure was above 7 MPa and sometimes even reached 11 MPa. According to the Mohr Circle reconstruction above, the Mohr-Coulomb failure criterion can already be reached for an induced pressure at 3.1 MPa for a favourably oriented fault or e.g., can go up to 4.3 MPa for less favourably oriented fault at 50° with respect to σ_1. We also have to note that a fluid-pressure reduction occurs within the borehole due to borehole friction. Hence, answer rating to this question is 25% given the uncertainties in rock physics at the injection point at depth. The maximum points scorable then become −1.25 or +1.25.

Answer: Mohr-Coulomb failure criterion is overpassed: +1.25

Remarks about this Mohr-Coulomb criterion (see also Section 5.1):

1. *The values are computed based on average rock mechanical parameters applicable for the Balmatt case of which the actual values, difficult to measure or even estimate, can differ significantly;*
2. *Even if the Mohr-Coulomb failure criterion estimate is correct, it indicates that a rupture is possible at one point. It does not tell anything about the way the rupture may propagate. It remains a quite challenging question in seismology to understand why ruptures propagate or not, and how far. This depends on fault geometry, friction, the state of stress, or the presence of asperities. In other words, it seems that there is presently no way to distinguish between the initiation processes of small and large earthquakes (Kanamori, 1996; Meier et al., 2016).*

(7) Do the Focal Mechanisms Indicate an Induced Event?

In some cases of induced seismicity, the putative causative mechanism for induced events implies a particular focal mechanism (*e.g.,* Cesca *et al.*, 2013). Typically, this is the case when seismicity is induced by depletion and compaction of reservoirs (*e.g.,* Ottemöller, 2005; Willacy *et al.*, 2019), where the source mechanism will be determined by the position of the event relative to the compacting zone (Segall, 1989). In contrast, for many cases of induced seismicity the focal mechanisms are consistent

with the regional stress conditions (e.g., Clarke *et al.*, 2014; Eaton & Mahani, 2015; McNamara *et al.*, 2015; McNamara *et al.*, 2015). Therefore, focal mechanisms that are consistent with the regional stress field do not point toward either a natural or induced cause, because this is observed in both induced and natural cases. However, focal mechanisms that are not consistent with the regional stress, but are consistent with the proposed causative mechanism, can be used as evidence that events are induced. Robust determination of focal mechanisms requires good signal-to-noise ratios and good coverage of the focal sphere.

Evidence assessment:

There is currently no robust conclusion on the focal mechanisms, even for the largest event. For example, the focal mechanisms provided by INERIS and DMT do not include the distant stations of the ROB, and are sensitive to the velocity models.

The answer rating is 0%. Maximum points scorable: 0

Answer: It is presently not possible to show whether or not the source mechanism is consistent with the regional stress field: NA.

5.4 Conclusion

The IAR is positive – all answers are ≥ 0 –, indicating that the available evidence points to an induced cause. The IAR becomes 92% if we can confirm the burst of activity in light of the industrial process (Q3, +15) and the migration (Q5c, +10). The ESR is high, indicating that this judgment is robust, and that most of the desired evidence is available.

Table 14: *Balmatt case: final results. Values in brackets indicate a potential maximum score that can be assigned.*

Questions	Answer Rating	Min score	Max score	Actual score
Q1	100 %	-8	8	**1**
Q2	100 %	-15	5	**5**
Q3	100 %	-4	15	**4 [15]**
Q4	100 %	-4	3	**3**
Q5	100 %	-10	10	**5 [10]**
Q6	25 %	-1.25	1.25	**1.25**
Q7	0 %	0	0	**NA**
Total	NA	-42.25	42.25	19.25 [35.25]

$$ESR = \frac{42.25 + 42.25}{96} \Leftrightarrow 88\% \qquad IAR = \frac{19.25}{42.25} \Leftrightarrow 46\%$$

6. DISCUSSION OF CRITICAL PARAMETERS AND PROTOCOLS

6.1 GRID APPROACH BEFORE STARTING GEOTHERMAL OPERATIONS

Fully open or partly open geothermal systems can induce potentially damaging seismicity. However, not all geothermal systems need the same level of attention to induced seismicity. The seismic hazard depends on the local geological conditions and the geothermal reservoir. The seismic risk depends on the hazard level, the site amplification, the exposed buildings and infrastructure and their vulnerability, population and the social concern. Several frameworks and recommendations for assessment and managing induced seismicity exist (summarised in Trutnevyte and Wiemer, 2017). However, none of these examples provides clear guidance to licensing authorities or regulators to pre-assess whether the project will be prone to seismicity and how the concern about induced seismicity of the local population may increase. To cover this gap, Trutnevyte and Wiemer (2017) developed a screening tool, called **Geothermal Risk of Induced seismicity Diagnosis** or GRID, to get a sense to what extent potential induced seismicity is of concern for a specific project. It is recommended to apply GRID early in the planning stage, before a well is drilled, and it can be revisited throughout the project as new knowledge emerges.

GRID has been customised to Switzerland but could be transferred to other countries with similar geological context (e.g., Carboniferous limestones in the Alpine foreland is somewhat similar to the Campine Basin). Ideally, Trutnevyte and Wiemer (2017) recommend that at least three parties, i.e., operator, authority/regulator and independent expert, should be involved to maximise the available information. Some scores, especially social concern, are susceptible to subjectivity and should be assessed by each partner independently to show the divergence in opinion and to promote discussion. Subsequently, GRID scores can be reviewed by a professional.

GRID is based on the following indicators subdivided into three concern groups.:

- **Seismic hazard concern:** depth, cumulative injection volume during stimulation[7], daily injection or extraction volume during operation, rock type, the separation between background and induced seismicity, fluid injection pressure, distance to known and potentially active faults with lengths greater than 3 km.
- **Concern about exposure, vulnerability, and secondary hazards:** Local site amplification, exposed population, industrial and commercial activity, importance of buildings and infrastructure, infrastructure with considerable environmental risk, unreinforced cultural heritage, and susceptibility to secondary hazards.
- **Social concern:** Potential for concern in the general population, vulnerable or strongly opposing stakeholders, negative experience with similar projects, lack of trust in the project operator or authorities, and benefits to the local community.

Each indicator in the three concern groups needs to be assessed to evaluate GRID. To every indicator a value is assigned with following values: 0 (little concern), 1 (medium concern) or 2 (high concern) (see Trutnevyte and Wiemer, 2017). Summing the scores within each group allows plotting the decision on the GRID graph (Figure 43) which eventually allows categorizing the evaluated project. In the GRID graph, the sum of the seismic hazard concern is plotted along the x-axis. The sum of the exposure,

[7] The authors mention 'stimulation'. But we think that this remains true for injection without stimulation.

vulnerability and secondary hazard is plotted on the y-axis. A project without social concern (i.e., sum = 0) is plotted as a black dot in Figure 43. A project with a high social concern (e.g., sum = 8; maximum score possible = 10) is plotted as a black square in Figure 43. Social concern is assumed to diagonally increase the GRID score by adding 0.5 on both axes.

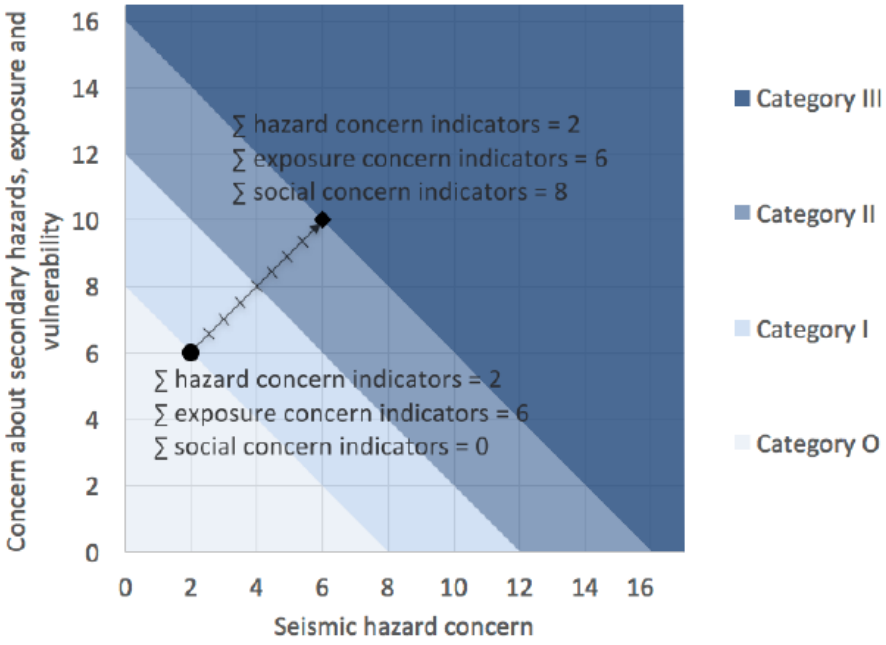

Figure 43: *GRID graph illustrating how each group contributes to the project category decision. The position of the black dot is determined by the hazard concern (x-axis) and exposure, vulnerability and secondary hazard concern (y-axis). Maximum possible score along the x-axis or y-axis is 14. Maximum possible score for the social concern is 10. The GRID score increases when social concern increases (illustrated by the diagonal repositioning of the black dot towards the black square). The example is theoretical illustrating the applicability of the GRID method. Source: Trutnevyte and Wiemer (2017).*

Based on the obtained scores and as illustrated in the graph, a decision can be made in which category the project scores. Four different categories are defined:

- Category 0: hazard and risk very low
- Category I: stress perturbations possible, no significant social concern
- Category II and III: induced seismicity is likely, damaging events and social concerns are possible.

For each category, actions are proposed for mitigation (i.e., insurance, structural retrofitting, information and outreach, design of the TLS or ATLS, hazard and risk assessment). We further refer to Trutnevyte and Wiemer (2017) for a detailed description of indicators, concern groups and actions to undertake within each category.

In this report, we deliberately do not perform the GRID exercise on the Balmatt or Janssen geothermal projects. We lack certain hazard concern indicators (e.g., injection volumes, rate, …) and our view on the social concern as a federal governmental institution is different than those of an operator or a regulator. Nevertheless, we encourage each party to perform the GRID exercise both before the start of operations and during the activities to stimulate discussion and decision making.

6.2 THE TRAFFIC LIGHT SYSTEM

6.2.1 Overview of TLSs from literature

Traffic light systems (TLSs) have been implemented for limiting the strength of induced seismicity. The concept that induced earthquakes might be controllable by operational measures goes back to fluid-injection experiments conducted in the 1960s by the US army in Denver, Colorado, for the disposal of chemical fluid wastes (Council, 2013). Based on the temporal correlation between induced earthquake activity and fluid injection or withdrawal, it was concluded that the number of induced earthquakes can be controlled by the fluid pressure in a fault zone (Baisch *et al.*, 2019).

Several regulatory authorities defined TLSs, in which injection operations are reduced or suspended when the induced seismicity exceeds predefined magnitude threshold values. Baisch *et al. (*2019) review the fundamental assumptions regarding the controllability of induced seismicity. The definition of TLS as a measure to prevent the occurrence of operation-related earthquakes exceeding a critical strength rests on several assumptions regarding the process of earthquake evolution with time:

- Assumption 1: The maximum strength (magnitude) of induced earthquakes increases gradually with the duration of the subsurface operations. This allows identifying the point in time when the magnitude of the earthquakes approaches a critical limit;
- Assumption 2: Each earthquake exceeding a critical strength is accompanied by precursory, smaller magnitude earthquakes;
- Assumption 3: Operational measures for limiting the strength of induced earthquakes exist.
- Assumption 4: The time delay between stoplight and the mitigation measure becoming effective is sufficiently small to prevent magnitude escalation into the undesired range (trailing effects).

With such assumptions, TLSs are based on an ad hoc definition of an acceptable level of earthquake strength and respond to earthquakes exceeding these levels, for example, by reducing flow rates, shutting down operations, or flowing back. To what extent the earthquake activity is operationally controllable is usually not considered.

In all the 12 cases reviewed by Baisch *et al. (*2019), seismicity starts at a low-magnitude level and earthquake magnitude gradually increases with the duration of the injection. An important observation is the occurrence of post-injection seismicity with comparatively large magnitudes. This is also the case at the Balmatt site, where the largest seismic moment release in October 2016 and June 2019 occurred after the injection was terminated, that is, at zero flow rate. Although seismic moment release tends to increase with the injection rate in some experiments, a general correlation between these parameters is not observed.

A characteristic observation in the context of fluid injection-induced seismicity is the systematic spatiotemporal pattern of hypocentre locations. Seismicity starts near the injection point and migrates away in the course of the injection operation. Based on the geomechanical processes discussed previously, the spatiotemporal seismicity evolution can be explained by the process of hydraulic pressure diffusion. Induced seismicity approximately follows a hydraulic triggering front and ceases because of stress relaxation, referred to as the Kaiser effect (Kaiser, 1950) or the hydraulic backfront (Shapiro and Dinske, 2009). Noting that the size of an earthquake scales with the slip area and that the size of the pressurized reservoir and hence a potential slip area increases with the duration of the injection, the observed gradual increase of earthquake magnitude can be interpreted in terms of a simple geometrical effect. In this interpretation, the fundamental TLS requirements of a gradual magnitude increase, and the occurrence of precursory seismicity to strong events are valid.

Another characteristic observation is the occurrence of post-injection seismicity of comparatively large magnitude. This can be interpreted as a consequence of hydraulic pressure diffusion, which is an ongoing process if nonstationary conditions prevail at the end of the injection (Baisch *et al.*, 2006; Hsieh and Bredehoeft, 1981). Trailing effects, that is, the post-operational magnitude increase, clearly limit the performance of a TLS (compare with Bommer *et al.*, 2015) because post-injection seismicity is beyond operational control. Therefore, the TLS performance is critically dependent on a forecast model that accounts for post-injection seismicity based on which TLS thresholds need to be designed. For example, geomechanical models can be used to characterize post-injection pressure diffusion and to estimate the maximum earthquake for the post-injection period (e.g., Király *et al.*, 2014). The accuracy of such forecasts typically decreases with the duration of the trailing effect, implying that trailing effects following short-term injections can be better assessed than those following long-term injections.

An example of a TLS failure, in the sense that a damaging earthquake was not prevented, is the stimulation of a geothermal reservoir underneath the city of Basel, Switzerland. Here, the trailing effect was not properly accounted for in the design of the TLS. The fluid injection was stopped after an M_L 2.6 earthquake was induced. This triggered the orange alarm level so that the injection pressure was reduced around 2006 December 8, 4:00, and fully stopped on the same day at 11:33. However, 5 hr later, a magnitude M_L 3.4 earthquake occurred, causing insurance claims in the order of $7 million U.S. (Baisch, *et al.*, 2009).

The injection rate and/or pressure are the only operational parameters considered to be relevant for mitigating induced seismicity. In principle, other operational parameters such as cyclic injection and the composition and temperature of the injected fluid could also influence the occurrence of induced seismicity.

The occurrence of induced seismicity is a multiparameter phenomenon, depending on details of subsurface structures as well as on the complete history of operational measures. Correlating the injection rate with induced seismicity observations only captures a part of this multiparameter interaction.

By analysing four different geothermal locations with 12 injection experiments conducted at various stages of reservoir development, Baisch *et al. (*2019) seek to identify general characteristics, but could not claim their general validity. The degree to which an earthquake of a given strength can be prevented by a TLS is limited and the rules remain heuristic. TLSs are best suited for short-term fluid injections, in which trailing effects, caused by pressure diffusion continuing to progress within the formation after shut-in, can be accounted for by a priori assumptions (and hence, it is actually a trial-and-error method!) in the TLS design. It is currently discussed if the M_W 5.4 earthquake at Pohang (Kim *et al.*, 2018) was triggered by geothermal stimulations, implying a possible trailing effect in the order of 2 magnitude units.

The authors recommend investigating the expected efficiency of a TLS as part of the TLS design process. Geomechanical models can be used to study stress changes caused by anthropogenic activities. Although knowledge of subsurface conditions is usually not sufficient for making reasonable seismicity forecasts, the general characteristics of stress changes such as the spatial extension of positive Coulomb stress changes, i.e. the spatial region over which faults are brought closer to stress criticality, build-up time, and trailing effects can be indicators for the robustness of a TLS.

6.2.2 Relevant parameters for a Traffic Light System (TLS)

We saw in Section 3.3 that the magnitude is a parameter that is difficult to assess, and does not really account for the actual ground motion. The actual ground displacements will of course, depend on the energy released by the earthquake, and hence, depend on the magnitude, but it will also be strongly dependent on:

1. The location and depth of the hypocentre (or focus): the deeper the earthquake, the weaker the surface ground motion, because of the distance attenuation, which is site-dependent;
2. The focal mechanism and directivity: for example, a rupture propagating towards the observer will provide displacements higher in amplitude and shorter in time, than a rupture moving away from the observer;
3. The stress drop (i.e., the difference in shear stress on a fault surface before and after an earthquake; related to the energy release induced by an earthquake): a noteworthy point about earthquakes is that stress drops range 1-200 MPa, whatever the magnitude (Allmann and Shearer, 2009; Onwuemeka *et al.*, 2018). Another point is that the stress drop is usually higher by a factor of 2 in intraplate zones (in average, 6 MPa) than in interplate ones (in average, 3 MPa) (Allmann and Shearer, 2009). Presently, no significant difference between induced and natural events could be found (Fischer and Hainzl, 2017; Huang *et al.*, 2017, 2016; Wu *et al.*, 2018). The evolution of the stress-drop with time and distance from the injection point may inform on the physical processes of induced earthquakes (Goertz-Allmann *et al.*, 2011). A higher stress drop enhances the high frequencies in the signal. This also implies that intraplate faults are stronger in some sense than interplate faults and have smaller fault dimensions for the same moment release;
4. The site effects that can amplify dramatically the ground motion, at given frequencies (resonance), both in amplitude and duration. Site effects depend on the stiffness of the ground, and on geometrical features (e.g., a basin will react differently from a ridge).

Hence, relevant parameters that should be studied and taken into account in a TLS are:

1. The locations of the events and their uncertainties;
2. The actual ground motion, either velocities (industrial vibration norms are often given in terms of velocities), or accelerations (used for response spectra of critical industries), and the frequency content of the signal;
3. The seismicity rate (number of events per hour, for example);
4. The migration of events;
5. The Gutenberg and Richter relationship, which relies on the number of earthquakes of given magnitudes, hence, the magnitude remains a quite relevant parameter.

Event location

The quality of a hypocentre location is strongly dependent on the velocity model used, the station sensitivity and noise level, seismometer sampling rate, manual versus automatic earthquake arrival picking, etc. To locate earthquake hypocenters accurately, the following steps are usually taken into account:

1. Automatic screening of waveforms for earthquake detection. Algorithms screen the waveforms and apply signal autopicking based on a predefined signal-to-noise ratio. If autopicks align, an event will be detected, a preliminary solution is calculated and the operator is warned;
2. Improving consistency of P- and S-wave arrivals by manual repicking (= verification of the event by the seismologist; Figure 44);

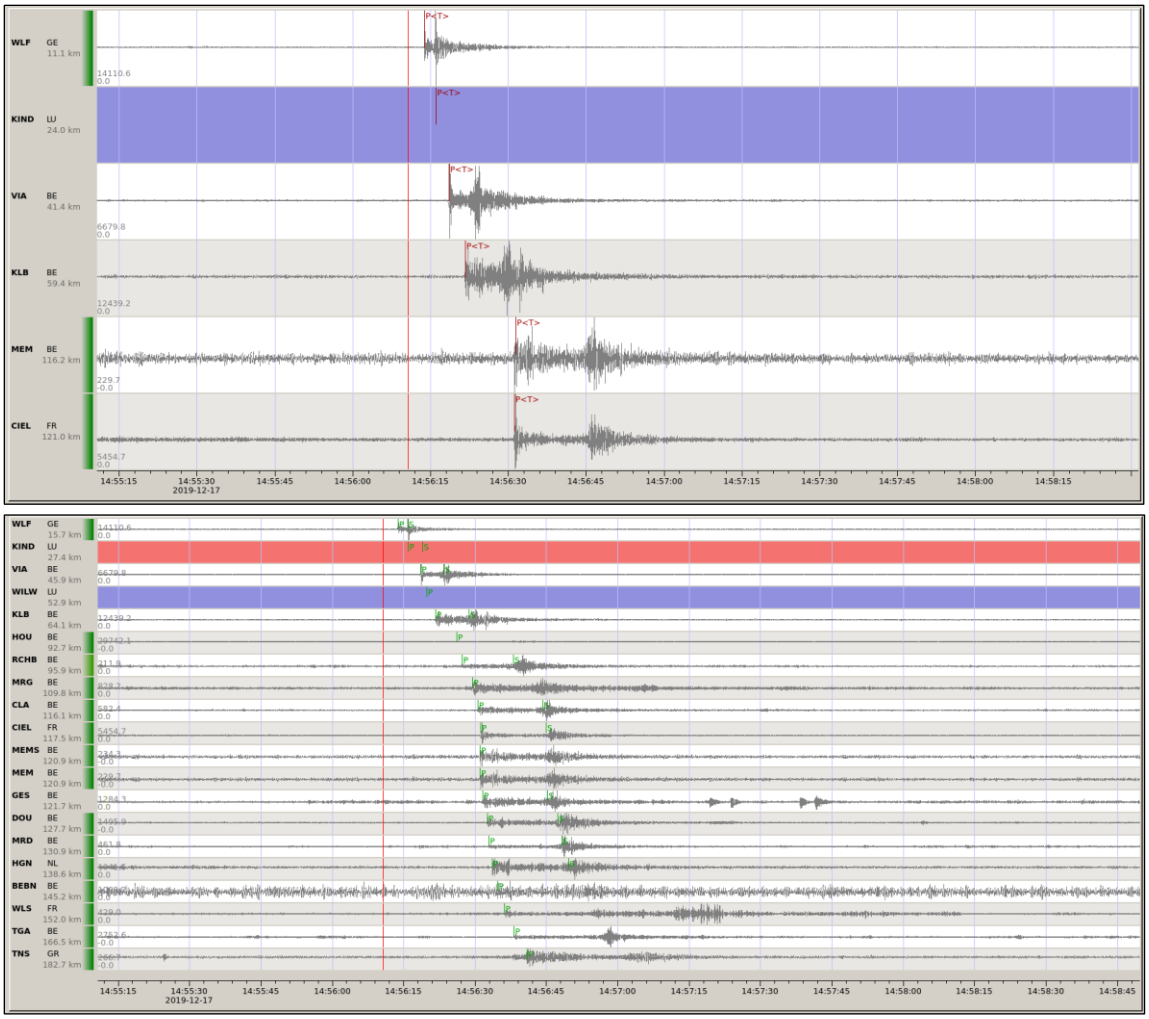

Figure 44: Above) *Autopicks (red vertical lines) of the 2019-12-17 M_L 2.2 Luxemburg (LU) earthquake in the SeiscomP3 software.* ***Below)*** *Verification and improvement of the earthquake arrivals (green lines) by the seismologist. The amount of stations increased because of the manual picking.*

3. First earthquake location and its uncertainty. Many software tools exist for locating earthquakes. The modified Hypo71 (Lee and Lahr, 1972) running at ROB, for instance, computes 500 locations for each event by adding or subtracting non-Gaussian noise to P- and S-wave measurements with maximum error of 0.05s or 0.10 s, respectively. The centroid of the generated cloud is then taken as final location. Such a procedure is more accurate than trusting only one location. Moreover, it provides an accurate overview of the uncertainty on each earthquake location and a correction of the exact onset of the event (t_0);
4. Induced events and events in natural earthquake swarms (e.g., Van Noten *et al.*, 2015) have very similar waveforms because their rays followed similar trajectories from source to detector and travelled through an almost identical medium. To improve the relative location between events, a cross-correlation technique can be used. In this technique, waveforms of closely located events are compared. This comparison allows to improve P- and S-wave arrival times. As result, cross-correlation, event relocation, and error estimation result in a better relative 3D event location. This technique is hard to perform in real-time but is essential in post-processing to link seismicity to faults.

The steps above provide a good methodology for precise event location but are still not a full guarantee for an accurate, absolute event location. Apart from the event picking task, the station quality and the

performance of the velocity model must be investigated as well. Following questions can be asked to critically assess the network performance:

- What is the sensitivity of the velocity model on the event location?
- What is the sensitivity on the location if one of the seismic stations is not working or has a too low signal-to-noise ratio?
- Is the sampling rate of the seismometer sufficient to distinguish between two co-located events (a too low sampling rate prohibits an accurate picking because one cannot differentiate between slightly different phase arrivals)?
- What is the completeness of the catalog? Seismic events may be overlooked at stations that have a significant different daily/nightly signal-to-noise ratio and hence events can be missed in the catalog. To account for this, a proper station noise analysis should be incorporated prior to operation.

Actual ground motion

There are well-established standards for ground vibrations caused by industrial processes such as railways, quarries, or civil engineering projects. For example, in Helsinki, for a 6.2 km deep geothermal project, the regulatory authority fixed the threshold based on such standards (Ader *et al.,* 2019):

- Green light: 0.3 mm/s, i.e., just above the noise level;
- Orange : 1 mm/s, limited perception;
- Red: 7.5 mm/s, i.e., half the threshold expected to cause minor damages (thin cracks in plaster, for example). Note that 7.5mm/s is much above the DIN4150 threshold for acceptable oscillation vibration for sensitive buildings and close to the ones for usual housing.

It remains a delicate choice to decide whether the orange colour should correspond to felt events or not. This must be discussed with local stakeholders, decision makers and the population.

Seismicity rate

Even if the earthquakes remain unfelt, an increase in the number of events per unit of time may indicate a destabilizing process. Note that, in order to calculate meaningful seismicity rates, only earthquakes with magnitude above a given minimum value (e.g., the completeness magnitude) should be counted.

Migration

To understand the mechanism behind induced earthquake triggering, the migration of seismicity in time can be a strong ally. The injected fluid perturbs local stress fields across a large area over time due to pore pressure diffusion and the poroelastic effect. The pore-pressure increase in the injection zone is expected to load the surrounding rock matrix and result in a fully coupled fluid-solid stress field. Examples show that different migration patterns may appear as a radial diffusion, or an alignment of seismicity may possibly reveal a previously unknown fault system. Elasticity is an effective means of transmitting forces to great distances, and therefore the fully coupled poroelastic stress field can extend well beyond the fluid pressure increase in the hydraulically connected region. Hence, the migration behavior of hypocenters, which is frequently seen in earthquake swarms, might provide valuable information on the mechanisms at play (Goebel and Brodsky, 2018; Kettlety *et al.*, 2020; Woo *et al.*, 2019).

However, before focussing the actions of a TLS on the seismicity migration, one has to provide high-precision earthquake hypocentre locations. Interpreting poorly-constrained earthquake locations has

not much sense if the uncertainty on individual events is e.g., larger than the width/length of a migration path (see section 5.2.2.1 above). Imperfect knowledge of the velocity structure can systematically over- or underestimate the focal depth and location of seismic events. Moreover, if subsurface fault structures at reservoir depths are only known from low-quality reflection seismic surveys, this uncertainty has to be incorporated in the TLS. Providing the authorities/regulator with a critical location procedure will facilitate acceptance of TLS migration decisions.

Magnitude-frequency distribution

The recurrence of earthquakes generated by a fault system or within an earthquake region is described by Gutenberg and Richter (1944) as the magnitude-frequency relationship. It is a measure for the relative occurrence of small and large earthquakes. For an earthquake population this relationship follows the power-law behaviour,

$$log(N) = a - bM$$

where N is the number of events with a magnitude larger than M (see also section 2.2). In this log-linear equation, the intercept a-value describes the overall seismic activity level within a region, and refers to the number of events with a magnitude > 0. The b-value defines the slope of the relationship. A b-value of 1 implies that if there is 1 magnitude >3 event, there will be 10 magnitude >2 events, 100 magnitude >1 events, and so on. In global tectonic earthquake populations, b values are commonly observed to be close to 1 (Figure 8). However, b-values can vary depending on the stress regime and the role of fluids. Often during hydraulic fracture stimulation, where fluids reduce the shear strength required to rupture the rock, b-values are much higher than unity (>2 is not uncommon, see e.g., Mousavi *et al.,* 2017).

Large b values are good news in seismic catalogs as it indicates a low probability of occurrence of large magnitude events. In the context of hydraulic fracture stimulation, high b-values indicate fluid-triggered development of a fracture network and low stress build-up. b-values near unity indicate higher stress build-up and possible fault reactivation. Determining robust b-values requires accurate measurements of magnitudes (i.e., all magnitude scales) and requires knowledge of the magnitude of completeness (Mc) of the catalog. Mc determines the threshold magnitude value below which no proper b-value can be calculated due to the incompleteness of the catalog (Figure 7). Temporal changes in the b-values reflect changes within the reservoir.

6.3 THE ADAPTIVE TLS (ATLS)

Assuming the location and magnitudes are correctly estimated, the TLS is simple, useful, but not very smart. This system is not based on any underlying physical reservoir model, it does not allow real-time optimisation, it does not benefit from better monitoring; the decisions are based on the extreme of a statistical distribution, not on a robust mean, it is not based on the integration of knowledge on geology, site response, ground motion prediction, building vulnerability or exposure. To take a weather analogue, a TLS means that you take an umbrella if you see black clouds. This is useful for the short term and simple, but not robust against surprises nor for longer forecast horizon. When using the adaptive TLS (ATLS), we do not really care about the rain itself, we rather care about the consequences of rain.

To overpass the limitations of the TLS heuristic methods, Mignan *et al.* (2017) proposed the adaptive traffic light system, which includes a linear relationship between seismicity rate and flow rate, as well as a normal diffusion process for post-injection. The goal of the ATLS is to forecast future seismicity and update a-priori risk study in near-real time, taking into account low-probability-high-consequence

events. The ATLS actuarial approach is superior to the so-called clinical approach of informal judgement, where magnitude thresholds vary significantly (between 0.5 and 4), with no clear link with the standard risk-based safety criteria used in other hazardous industries.

The magnitude m_{saf} at which the given safety limit is reached is fixed such that $Pr(m \geq m_{saf}) = Y$, with *Y*, the probability (Pr) of exceedance, which will ensure that the acceptable level of risk is preserved at all time. For example, it considers the probability that an earthquake is sufficiently strong to cause given degrees of damage, like building collapse, together with the probability that the collapsing buildings cause fatalities.

In the ATLS, the assignment of a magnitude threshold is based on a quantitative risk assessment, subject to a safety criterion imposed by the authorities (e.g., fixed probabilities of unaccepted nuisance, damage or fatalities). They propose as safety criterion an annual individual risk (IR) of 10^{-6}, which is a threshold commonly enforced for hazardous installations. This is the probability that a statistically representative individual dies for the introduced hazard. More generally, a safety criterion is a probability of exceedance that can be fixed with respect to different safety metrics, such as fatalities, economic loss, building damage or level of nuisance.

The method is based on injection flow rate, the linear relationship between flow rate and seismicity, and the exponential behaviour of the seismicity when injection ceases.

The ATLS proposed by Mignan *et al. (*2017) is a proof-of-concept of the actuarial approach. This model needs to be tested in different environments and acceptance levels of risk. For example, the post-injection models or the maximum possible magnitude, are not well known, and the safety threshold depends on hypotheses on the way buildings collapse (type of building, relationship between intensities and magnitude, which is far from trivial).

6.4 Conclusion

Clearly, we lack the required experience to set-up the best TLS or TLSA models. Interpreting the information of a TLS remains challenging. It is even more true if one does not dispose of detailed information on the reservoir and on the information if all the faults are accurately mapped. Questions should be asked if the events are located with sufficient horizontal and vertical precision, if the velocity model and the crustal attenuation model around the reservoir is sufficiently precise to locate the events and compute robust magnitudes. It is moreover also necessary to assess seismic hazard and further on, the risks.

As seen in the previous section, it is not only difficult to set-up a TLS, and even more an ATLS; it is also quite hazardous to assert that a TLS will prevent larger than expected earthquakes to occur. However, we can provide indications on the way the risk associated with induced seismicity can be assessed. The regulatory authority has to manage the risk as a function of risk acceptance criteria, as done e.g. for chemical facilities.

How the seismicity must be addressed depends not only on the geothermal system, but also on the existing infrastructure, populations, and social concern (Trutnevyte and Wiemer, 2017). As shown in section 5.2 an initial screening tool (Geothermal Risk of Induced Seismicity Diagnostic GRID) can be applied for estimating to what extent induced seismicity is of concern for a given project.

Finally, it is worth noting that, for example in Strasbourg (France), the Bureau Central Séismologique Français (BCSF), takes part in the discussions only on the increase of TLS level. The decision to lower the TLS level is taken by the regulator without their input (pers. comm.).

7. FUTURE INVESTIGATIONS

Based on this overview of induced earthquakes, we list a number of research questions that could be considered for more in-depth research in the longer term, both using existing data and by means of a theoretical study.

These research topics may be related to:

- The accurate localisation of earthquakes and the study of the spatial-temporal distribution of the epicentres;

- The precise mapping of faults using all available information and new geophysical methods;

- The b-value of the Gutenberg-Richter relationship and its variation;

- The determination of seismic source parameters: focal mechanism, stress drop;

- The relationship between injected pressure/volume and seismicity, including the elastic and diffuse processes;

- The better understanding of the mechanical state of the bedrock reservoir before, during and after fluid injection by various measuring tools;

- The modelling of ground motions, based on the observation of the induced events, the knowledge of the local geological conditions and ground-motion prediction equations;

- The evaluation of the impact of the seismic hazard on the seismic risk. The risk results from the combination of the natural hazard and the vulnerability of specific infrastructures.

8. GLOSSARY

Anelastic attenuation, or intrinsic attenuation: part of the energy of the seismic wave is converted to heat and lost. This is associated with small-scale crystal dislocations, friction, and movements of interstitial fluids. This intrinsic attenuation may be distinguished from scattering attenuation, in which amplitudes in the main seismic arrivals are reduced by scattering off small-scale heterogeneities, but the integrated energy in the total wavefield remains constant.

Geometric spreading: the energy of spherical wavefront emanating from a point source is distributed over a spherical surface of ever increasing radius r, this geometric spreading decreases the amplitude by a $1/r^2$ in order to ensure conservation of energy.

Ground motion acceleration: acceleration of the ground in m/s^2, as measured by an accelerometer or by taking the derivative of the signal from a seismometer. Strong, destructive ground motions are expressed in terms of acceleration, because (1) strong motion are easier to measure by using an accelerometer and (2), because the acceleration is directly related to the force that is acting against structures.

Ground motion velocity: in m/s, this is the value provided by modern seismographs, which are in turn velocity meters.

MFD: magnitude-frequency distribution.

MSC: magnitude scale conversion.

Pg: At short distances, either an upgoing P wave from a source in the upper crust or a P wave bottoming in the upper crust. At larger distances also arrivals caused by multiple P-wave reverberations inside the whole crust with a group velocity around 5.8 km/s.

Poisson process: stochastic process for modeling the times at which arrivals enter a system. In seismology, if one applies a Poisson process ones implicitely assume that the probability of occurence of an event is independent from a previous one. This contrasts with the non-Poissonian process.

Sampling rate: for a digital recorder, as modern seismographs or accelerographs, it is the number of samples recorded per second. In monitoring networks is usually 100-125 Hz for seismographs, and 200-250 Hz for accelerometers, but can be much higher for local investigations.

Sg: At short distances, either an upgoing S wave from a source in the upper crust or an S wave bottoming in the upper crust. At larger distances also arrivals caused by superposition of multiple S-wave reverberations and SV to P and/or P to SV conversions inside the whole crust.

Signal to noise ratio (SNR): compares the level of a desired signal to the level of background noise.

Site effects: local topographic and geological conditions can attenuate or amplify the seismic waves, in both duration and amplitudes, at given frequencies. A famous example is the alluvial deposit on which Mexico City has been founded, which amplified the seismic waves by a factor 10 during the 1985 earthquake, 430 km away from the epicenter.

ANNEX A: TEMPLATE MATCHING EVENT LIST – DSLS, DSLB, MOLT

Event Time	Similarity score	Channels
2016-09-13T06:53:25.66Z	0.7345981	[('DSLB', 'HHZ'), ('MOLT', 'HHZ')]
2016-09-14T06:20:32.14Z	0.734889984	[('DSLB', 'HHZ'), ('MOLT', 'HHZ')]
2016-09-15T03:17:09.96Z	0.806560874	[('DSLB', 'HHZ'), ('MOLT', 'HHZ')]
2016-09-15T04:10:11.74Z	1.18066287	[('DSLB', 'HHZ'), ('MOLT', 'HHZ')]
2016-09-15T04:30:16.56Z	1.406951308	[('DSLB', 'HHZ'), ('MOLT', 'HHZ')]
2016-09-15T05:43:15.06Z	1.323315501	[('DSLB', 'HHZ'), ('MOLT', 'HHZ')]
2016-09-15T05:57:24.88Z	-1.27912879	[('DSLB', 'HHZ'), ('MOLT', 'HHZ')]
2016-09-15T07:53:50.10Z	1.897539139	[('DSLB', 'HHZ'), ('MOLT', 'HHZ')]
2016-09-15T09:48:09.78Z	1.237572312	[('DSLB', 'HHZ'), ('MOLT', 'HHZ')]
2016-09-15T09:50:21.82Z	1.846939802	[('DSLB', 'HHZ'), ('MOLT', 'HHZ')]
2016-09-15T09:54:21.24Z	1.62180686	[('DSLB', 'HHZ'), ('MOLT', 'HHZ')]
2016-09-15T11:30:36.10Z	1.713713527	[('DSLB', 'HHZ'), ('MOLT', 'HHZ')]
2016-09-15T15:24:16.84Z	1.180575848	[('DSLB', 'HHZ'), ('MOLT', 'HHZ')]
2016-09-15T16:31:24.40Z	0.664506614	[('DSLB', 'HHZ'), ('MOLT', 'HHZ')]
2016-09-16T00:04:13.54Z	1.632491827	[('DSLB', 'HHZ'), ('MOLT', 'HHZ')]
2016-09-16T00:46:05.30Z	0.660871863	[('DSLB', 'HHZ'), ('MOLT', 'HHZ')]
2016-09-16T01:04:51.70Z	1.49362886	[('DSLB', 'HHZ'), ('MOLT', 'HHZ')]
2016-09-16T03:13:06.56Z	1.542536139	[('DSLB', 'HHZ'), ('MOLT', 'HHZ')]
2016-09-16T06:44:13.08Z	0.732507169	[('DSLB', 'HHZ'), ('MOLT', 'HHZ')]
2016-09-16T08:11:34.62Z	1.438076973	[('DSLB', 'HHZ'), ('MOLT', 'HHZ')]
2016-09-16T11:29:10.48Z	1.774230123	[('DSLB', 'HHZ'), ('MOLT', 'HHZ')]
2016-09-16T13:10:32.84Z	0.741805434	[('DSLB', 'HHZ'), ('MOLT', 'HHZ')]
2016-09-16T13:11:49.40Z	0.671806812	[('DSLB', 'HHZ'), ('MOLT', 'HHZ')]
2016-09-16T13:19:16.46Z	0.663382292	[('DSLB', 'HHZ'), ('MOLT', 'HHZ')]
2016-09-16T15:28:10.86Z	1.061198473	[('DSLB', 'HHZ'), ('MOLT', 'HHZ')]
2016-09-16T21:18:14.30Z	-0.68110621	[('DSLB', 'HHZ'), ('MOLT', 'HHZ')]
2016-09-16T21:43:20.12Z	-0.681520343	[('DSLB', 'HHZ'), ('MOLT', 'HHZ')]
2016-09-17T01:51:43.54Z	0.75511539	[('DSLB', 'HHZ'), ('MOLT', 'HHZ')]
2016-09-17T03:22:55.52Z	-0.739611924	[('DSLB', 'HHZ'), ('MOLT', 'HHZ')]
2016-09-17T04:39:40.74Z	0.724678934	[('DSLB', 'HHZ'), ('MOLT', 'HHZ')]
2016-09-17T16:22:51.16Z	0.978519917	[('DSLB', 'HHZ'), ('MOLT', 'HHZ')]
2016-09-17T19:30:08.46Z	0.748590946	[('DSLB', 'HHZ'), ('MOLT', 'HHZ')]
2016-09-18T00:27:08.10Z	-0.71511507	[('DSLB', 'HHZ'), ('MOLT', 'HHZ')]
2016-09-18T02:08:08.94Z	1.530709982	[('DSLB', 'HHZ'), ('MOLT', 'HHZ')]
2016-09-18T05:36:52.00Z	1.079649925	[('DSLB', 'HHZ'), ('MOLT', 'HHZ')]
2016-09-18T06:19:03.92Z	1.054593086	[('DSLB', 'HHZ'), ('MOLT', 'HHZ')]
2016-09-18T08:08:29.48Z	-0.678496599	[('DSLB', 'HHZ'), ('MOLT', 'HHZ')]
2016-09-18T13:06:52.24Z	0.88765049	[('DSLB', 'HHZ'), ('MOLT', 'HHZ')]
2016-09-18T16:24:29.10Z	1.213906288	[('DSLB', 'HHZ'), ('MOLT', 'HHZ')]
2016-09-18T17:41:58.26Z	1.787130952	[('DSLB', 'HHZ'), ('MOLT', 'HHZ')]
2016-09-18T19:04:01.12Z	-0.814542055	[('DSLB', 'HHZ'), ('MOLT', 'HHZ')]
2016-09-18T20:41:20.28Z	-0.892467976	[('DSLB', 'HHZ'), ('MOLT', 'HHZ')]
2016-09-18T22:11:13.84Z	1.015189648	[('DSLB', 'HHZ'), ('MOLT', 'HHZ')]
2016-09-18T22:56:19.94Z	1.229496121	[('DSLB', 'HHZ'), ('MOLT', 'HHZ')]
2016-09-19T22:49:55.54Z	0.764101565	[('DSLB', 'HHZ'), ('MOLT', 'HHZ')]
2016-09-21T19:43:14.66Z	1.037104368	[('DSLB', 'HHZ'), ('MOLT', 'HHZ')]
2016-09-23T08:56:49.06Z	0.725518465	[('DSLB', 'HHZ'), ('MOLT', 'HHZ')]
2016-09-24T02:02:43.16Z	1.088857174	[('DSLB', 'HHZ'), ('MOLT', 'HHZ')]
2016-09-24T09:10:29.08Z	0.828551054	[('DSLB', 'HHZ'), ('MOLT', 'HHZ')]
2016-09-24T09:18:19.34Z	1.395806074	[('DSLB', 'HHZ'), ('MOLT', 'HHZ')]
2016-09-24T09:25:28.14Z	1.318048358	[('DSLB', 'HHZ'), ('MOLT', 'HHZ')]
2016-09-24T09:26:15.38Z	0.772487104	[('DSLB', 'HHZ'), ('MOLT', 'HHZ')]
2016-09-24T09:32:00.00Z	0.738028288	[('DSLB', 'HHZ'), ('MOLT', 'HHZ')]
2016-09-26T04:59:24.32Z	1.181415081	[('DSLB', 'HHZ'), ('MOLT', 'HHZ')]
2016-09-28T23:54:38.44Z	0.897825956	[('DSLB', 'HHZ'), ('MOLT', 'HHZ')]
2016-10-03T19:50:20.08Z	1.715110302	[('DSLB', 'HHZ'), ('MOLT', 'HHZ')]
2016-10-04T13:01:04.98Z	0.809101939	[('DSLB', 'HHZ'), ('MOLT', 'HHZ')]

2016-10-05T16:28:03.46Z	0.744314849	[('DSLB', 'HHZ'), ('MOLT', 'HHZ')]
2017-01-28T17:16:12.62Z	1.214667201	[('DSLS', 'HHZ'), ('MOLT', 'HHZ')]
2017-03-22T20:25:34.42Z	0.937930286	[('DSLS', 'HHZ'), ('MOLT', 'HHZ')]
2017-08-21T01:58:30.60Z	1.587016344	[('DSLB', 'HHZ'), ('DSLS', 'HHZ'), ('MOLT', 'HHZ')]
2017-11-09T03:49:35.88Z	-0.89624685	[('DSLB', 'HHZ'), ('DSLS', 'HHZ'), ('MOLT', 'HHZ')]
2018-08-22T11:38:44.00Z	1.22018826	[('DSLB', 'HHZ'), ('DSLS', 'HHZ'), ('MOLT', 'HHZ')]
2018-12-05T03:50:21.08Z	1.036481977	[('DSLB', 'HHZ'), ('DSLS', 'HHZ'), ('MOLT', 'HHZ')]
2018-12-05T05:29:56.54Z	1.817221165	[('DSLB', 'HHZ'), ('DSLS', 'HHZ'), ('MOLT', 'HHZ')]
2018-12-05T15:37:33.38Z	1.746061087	[('DSLB', 'HHZ'), ('DSLS', 'HHZ'), ('MOLT', 'HHZ')]
2018-12-06T12:18:11.66Z	2.068803549	[('DSLB', 'HHZ'), ('DSLS', 'HHZ'), ('MOLT', 'HHZ')]
2018-12-06T21:12:29.32Z	1.20656836	[('DSLB', 'HHZ'), ('DSLS', 'HHZ'), ('MOLT', 'HHZ')]
2018-12-07T07:07:59.48Z	1.432439327	[('DSLB', 'HHZ'), ('DSLS', 'HHZ'), ('MOLT', 'HHZ')]
2018-12-07T16:06:46.58Z	0.902559042	[('DSLB', 'HHZ'), ('DSLS', 'HHZ'), ('MOLT', 'HHZ')]
2018-12-12T18:16:24.42Z	2.004826784	[('DSLB', 'HHZ'), ('DSLS', 'HHZ'), ('MOLT', 'HHZ')]
2018-12-13T02:55:02.00Z	1.294676781	[('DSLB', 'HHZ'), ('DSLS', 'HHZ'), ('MOLT', 'HHZ')]
2018-12-13T23:06:02.42Z	0.853416204	[('DSLB', 'HHZ'), ('DSLS', 'HHZ'), ('MOLT', 'HHZ')]
2018-12-15T23:43:06.28Z	1.340918064	[('DSLB', 'HHZ'), ('DSLS', 'HHZ'), ('MOLT', 'HHZ')]
2018-12-18T12:40:04.04Z	-2.041276455	[('DSLB', 'HHZ'), ('DSLS', 'HHZ'), ('MOLT', 'HHZ')]
2018-12-18T13:48:19.12Z	2.597296953	[('DSLB', 'HHZ'), ('DSLS', 'HHZ'), ('MOLT', 'HHZ')]
2018-12-18T14:05:27.72Z	1.606402874	[('DSLB', 'HHZ'), ('DSLS', 'HHZ'), ('MOLT', 'HHZ')]
2018-12-19T03:50:33.20Z	1.166576266	[('DSLB', 'HHZ'), ('DSLS', 'HHZ'), ('MOLT', 'HHZ')]
2018-12-19T05:49:06.82Z	-1.708529949	[('DSLB', 'HHZ'), ('DSLS', 'HHZ'), ('MOLT', 'HHZ')]
2018-12-19T06:53:21.82Z	0.809255481	[('DSLB', 'HHZ'), ('DSLS', 'HHZ'), ('MOLT', 'HHZ')]
2018-12-19T23:32:59.40Z	0.793758988	[('DSLB', 'HHZ'), ('DSLS', 'HHZ'), ('MOLT', 'HHZ')]
2018-12-22T06:32:35.92Z	1.304442883	[('DSLB', 'HHZ'), ('DSLS', 'HHZ'), ('MOLT', 'HHZ')]
2018-12-22T21:55:02.26Z	1.855081916	[('DSLB', 'HHZ'), ('DSLS', 'HHZ'), ('MOLT', 'HHZ')]
2018-12-22T22:01:08.36Z	1.343615055	[('DSLB', 'HHZ'), ('DSLS', 'HHZ'), ('MOLT', 'HHZ')]
2018-12-27T04:48:01.38Z	1.09869206	[('DSLB', 'HHZ'), ('DSLS', 'HHZ'), ('MOLT', 'HHZ')]
2019-01-02T17:03:33.72Z	1.211387992	[('DSLB', 'HHZ'), ('DSLS', 'HHZ'), ('MOLT', 'HHZ')]
2019-01-17T23:21:35.26Z	2.492512941	[('DSLB', 'HHZ'), ('DSLS', 'HHZ'), ('MOLT', 'HHZ')]
2019-01-18T08:25:06.42Z	1.85752058	[('DSLB', 'HHZ'), ('DSLS', 'HHZ'), ('MOLT', 'HHZ')]
2019-01-18T18:39:41.26Z	1.087453604	[('DSLB', 'HHZ'), ('DSLS', 'HHZ'), ('MOLT', 'HHZ')]
2019-01-19T19:23:56.88Z	-0.814803958	[('DSLB', 'HHZ'), ('DSLS', 'HHZ'), ('MOLT', 'HHZ')]
2019-01-22T23:53:01.70Z	1.644114137	[('DSLB', 'HHZ'), ('DSLS', 'HHZ'), ('MOLT', 'HHZ')]
2019-02-16T23:55:57.06Z	1.415293932	[('DSLB', 'HHZ'), ('DSLS', 'HHZ'), ('MOLT', 'HHZ')]
2019-02-17T01:25:16.84Z	1.825362206	[('DSLB', 'HHZ'), ('DSLS', 'HHZ'), ('MOLT', 'HHZ')]
2019-02-18T04:08:15.80Z	1.210394144	[('DSLB', 'HHZ'), ('DSLS', 'HHZ'), ('MOLT', 'HHZ')]
2019-02-19T12:56:55.08Z	1.716036916	[('DSLB', 'HHZ'), ('DSLS', 'HHZ'), ('MOLT', 'HHZ')]
2019-02-19T20:31:44.72Z	1.449189305	[('DSLB', 'HHZ'), ('DSLS', 'HHZ'), ('MOLT', 'HHZ')]
2019-02-20T01:20:45.40Z	1.277225137	[('DSLB', 'HHZ'), ('DSLS', 'HHZ'), ('MOLT', 'HHZ')]
2019-02-20T03:44:20.58Z	1.384079218	[('DSLB', 'HHZ'), ('DSLS', 'HHZ'), ('MOLT', 'HHZ')]
2019-03-01T13:28:25.68Z	-1.168899894	[('DSLB', 'HHZ'), ('DSLS', 'HHZ'), ('MOLT', 'HHZ')]
2019-03-02T01:19:50.96Z	1.325295329	[('DSLB', 'HHZ'), ('DSLS', 'HHZ'), ('MOLT', 'HHZ')]
2019-05-22T18:27:51.74Z	1.278605223	[('DSLB', 'HHZ'), ('DSLS', 'HHZ'), ('MOLT', 'HHZ')]
2019-05-23T01:12:09.38Z	1.328789353	[('DSLB', 'HHZ'), ('DSLS', 'HHZ'), ('MOLT', 'HHZ')]
2019-05-23T01:14:26.90Z	1.596517563	[('DSLB', 'HHZ'), ('DSLS', 'HHZ'), ('MOLT', 'HHZ')]
2019-05-23T02:50:44.54Z	1.91589427	[('DSLB', 'HHZ'), ('DSLS', 'HHZ'), ('MOLT', 'HHZ')]
2019-05-23T06:37:25.56Z	2.002918243	[('DSLB', 'HHZ'), ('DSLS', 'HHZ'), ('MOLT', 'HHZ')]
2019-05-24T17:01:39.62Z	1.072527289	[('DSLB', 'HHZ'), ('DSLS', 'HHZ'), ('MOLT', 'HHZ')]
2019-05-25T14:46:21.92Z	1.196778297	[('DSLB', 'HHZ'), ('DSLS', 'HHZ'), ('MOLT', 'HHZ')]
2019-05-26T00:29:12.66Z	1.132593274	[('DSLB', 'HHZ'), ('DSLS', 'HHZ'), ('MOLT', 'HHZ')]
2019-05-26T16:42:57.02Z	1.224669576	[('DSLB', 'HHZ'), ('DSLS', 'HHZ'), ('MOLT', 'HHZ')]
2019-05-26T23:19:28.80Z	1.261649847	[('DSLB', 'HHZ'), ('DSLS', 'HHZ'), ('MOLT', 'HHZ')]
2019-05-29T08:26:42.66Z	1.307206631	[('DSLB', 'HHZ'), ('DSLS', 'HHZ'), ('MOLT', 'HHZ')]
2019-06-02T00:08:29.30Z	1.087281227	[('DSLB', 'HHZ'), ('DSLS', 'HHZ'), ('MOLT', 'HHZ')]
2019-06-02T07:23:13.22Z	-1.485366344	[('DSLB', 'HHZ'), ('DSLS', 'HHZ'), ('MOLT', 'HHZ')]
2019-06-13T22:07:34.88Z	0.707446992	[('DSLS', 'HHZ'), ('MOLT', 'HHZ')]
2019-06-13T22:20:55.26Z	0.833278418	[('DSLS', 'HHZ'), ('MOLT', 'HHZ')]
2019-06-13T23:56:43.20Z	0.910770893	[('DSLS', 'HHZ'), ('MOLT', 'HHZ')]
2019-06-14T00:33:12.44Z	1.012508988	[('DSLS', 'HHZ'), ('MOLT', 'HHZ')]
2019-06-14T02:47:14.50Z	0.902266026	[('DSLS', 'HHZ'), ('MOLT', 'HHZ')]
2019-06-14T02:56:38.38Z	0.753030479	[('DSLS', 'HHZ'), ('MOLT', 'HHZ')]
2019-06-14T02:58:51.66Z	0.6690045	[('DSLS', 'HHZ'), ('MOLT', 'HHZ')]

2019-06-14T05:37:23.56Z	-1.102574468	[('DSLS', 'HHZ'), ('MOLT', 'HHZ')]
2019-06-14T18:41:52.46Z	0.732191443	[('DSLS', 'HHZ'), ('MOLT', 'HHZ')]
2019-06-15T02:15:42.54Z	0.859149456	[('DSLS', 'HHZ'), ('MOLT', 'HHZ')]
2019-06-15T11:40:04.64Z	0.68910861	[('DSLS', 'HHZ'), ('MOLT', 'HHZ')]
2019-06-15T13:49:52.20Z	0.799087405	[('DSLS', 'HHZ'), ('MOLT', 'HHZ')]
2019-06-15T15:04:28.44Z	0.636469066	[('DSLS', 'HHZ'), ('MOLT', 'HHZ')]
2019-06-15T18:08:06.90Z	0.641908228	[('DSLS', 'HHZ'), ('MOLT', 'HHZ')]
2019-06-15T20:29:33.34Z	-0.739806175	[('DSLS', 'HHZ'), ('MOLT', 'HHZ')]
2019-06-15T21:21:44.58Z	-0.787812173	[('DSLS', 'HHZ'), ('MOLT', 'HHZ')]
2019-06-15T23:11:46.52Z	1.159604669	[('DSLS', 'HHZ'), ('MOLT', 'HHZ')]
2019-06-15T23:57:37.70Z	1.027805567	[('DSLS', 'HHZ'), ('MOLT', 'HHZ')]
2019-06-16T01:14:33.94Z	0.682650864	[('DSLS', 'HHZ'), ('MOLT', 'HHZ')]
2019-06-16T02:09:39.78Z	0.770922363	[('DSLS', 'HHZ'), ('MOLT', 'HHZ')]
2019-06-16T03:27:13.48Z	1.102148414	[('DSLS', 'HHZ'), ('MOLT', 'HHZ')]
2019-06-16T13:45:57.06Z	0.696030498	[('DSLS', 'HHZ'), ('MOLT', 'HHZ')]
2019-06-16T14:04:01.16Z	0.789323986	[('DSLS', 'HHZ'), ('MOLT', 'HHZ')]
2019-06-16T17:11:20.12Z	0.709927499	[('DSLS', 'HHZ'), ('MOLT', 'HHZ')]
2019-06-16T17:38:46.40Z	0.682995617	[('DSLS', 'HHZ'), ('MOLT', 'HHZ')]
2019-06-16T18:50:32.62Z	0.683015883	[('DSLS', 'HHZ'), ('MOLT', 'HHZ')]
2019-06-16T23:27:49.78Z	0.628886342	[('DSLS', 'HHZ'), ('MOLT', 'HHZ')]
2019-06-17T02:13:38.52Z	0.705628216	[('DSLS', 'HHZ'), ('MOLT', 'HHZ')]
2019-06-17T10:17:06.08Z	1.170125604	[('DSLS', 'HHZ'), ('MOLT', 'HHZ')]
2019-06-17T13:19:45.24Z	0.756315172	[('DSLS', 'HHZ'), ('MOLT', 'HHZ')]
2019-06-17T19:20:35.98Z	0.714781106	[('DSLS', 'HHZ'), ('MOLT', 'HHZ')]
2019-06-17T19:41:59.14Z	0.800497293	[('DSLS', 'HHZ'), ('MOLT', 'HHZ')]
2019-06-17T20:56:42.28Z	0.688987017	[('DSLS', 'HHZ'), ('MOLT', 'HHZ')]
2019-06-17T21:37:52.54Z	-0.674427509	[('DSLS', 'HHZ'), ('MOLT', 'HHZ')]
2019-06-17T23:06:42.10Z	0.695172071	[('DSLS', 'HHZ'), ('MOLT', 'HHZ')]
2019-06-18T00:08:18.16Z	0.809377611	[('DSLS', 'HHZ'), ('MOLT', 'HHZ')]
2019-06-18T03:26:23.42Z	1.01068902	[('DSLS', 'HHZ'), ('MOLT', 'HHZ')]
2019-06-18T11:18:02.60Z	0.852562428	[('DSLS', 'HHZ'), ('MOLT', 'HHZ')]
2019-06-18T20:55:22.78Z	-0.76038605	[('DSLS', 'HHZ'), ('MOLT', 'HHZ')]
2019-06-18T21:16:02.66Z	0.73402977	[('DSLS', 'HHZ'), ('MOLT', 'HHZ')]
2019-06-19T03:14:31.90Z	0.870553494	[('DSLS', 'HHZ'), ('MOLT', 'HHZ')]
2019-06-19T03:48:43.44Z	0.790278077	[('DSLS', 'HHZ'), ('MOLT', 'HHZ')]
2019-06-19T04:51:34.48Z	0.665339649	[('DSLS', 'HHZ'), ('MOLT', 'HHZ')]
2019-06-19T05:14:09.92Z	-0.759545088	[('DSLS', 'HHZ'), ('MOLT', 'HHZ')]
2019-06-19T05:47:15.22Z	0.630855143	[('DSLS', 'HHZ'), ('MOLT', 'HHZ')]
2019-06-19T06:40:24.56Z	0.762814701	[('DSLS', 'HHZ'), ('MOLT', 'HHZ')]
2019-06-19T07:27:39.74Z	-0.778030396	[('DSLS', 'HHZ'), ('MOLT', 'HHZ')]
2019-06-19T10:35:03.56Z	0.689157844	[('DSLS', 'HHZ'), ('MOLT', 'HHZ')]
2019-06-19T16:45:40.66Z	0.917548418	[('DSLS', 'HHZ'), ('MOLT', 'HHZ')]
2019-06-19T23:46:15.18Z	0.807629406	[('DSLS', 'HHZ'), ('MOLT', 'HHZ')]
2019-06-21T01:13:21.96Z	0.831845939	[('DSLS', 'HHZ'), ('MOLT', 'HHZ')]
2019-06-21T03:43:10.74Z	0.742110133	[('DSLS', 'HHZ'), ('MOLT', 'HHZ')]
2019-06-23T17:27:30.50Z	0.865677595	[('DSLS', 'HHZ'), ('MOLT', 'HHZ')]
2019-06-23T17:30:42.20Z	1.034595966	[('DSLS', 'HHZ'), ('MOLT', 'HHZ')]
2019-06-23T19:03:35.42Z	0.84453553	[('DSLS', 'HHZ'), ('MOLT', 'HHZ')]
2019-06-23T19:14:02.70Z	1.066251397	[('DSLS', 'HHZ'), ('MOLT', 'HHZ')]
2019-06-26T22:39:21.70Z	0.707166612	[('DSLS', 'HHZ'), ('MOLT', 'HHZ')]
2019-09-24T22:01:24.44Z	0.678498745	[('DSLS', 'HHZ'), ('MOLT', 'HHZ')]

ANNEX B: TEMPLATE MATCHING EVENT LIST – MOLT

Event Time	Similarity score	Channels
2016-08-05T16:01:51.99Z	1.210036039	[('MOLT', 'HHE'), ('MOLT', 'HHN'), ('MOLT', 'HHZ')]
2016-08-06T21:22:26.49Z	1.087277889	[('MOLT', 'HHE'), ('MOLT', 'HHN'), ('MOLT', 'HHZ')]
2016-08-06T22:31:38.31Z	1.032800317	[('MOLT', 'HHE'), ('MOLT', 'HHN'), ('MOLT', 'HHZ')]
2016-08-07T01:54:00.48Z	1.005227566	[('MOLT', 'HHE'), ('MOLT', 'HHN'), ('MOLT', 'HHZ')]
2016-08-07T05:02:04.42Z	1.201872587	[('MOLT', 'HHE'), ('MOLT', 'HHN'), ('MOLT', 'HHZ')]
2016-08-07T23:12:34.69Z	1.412037134	[('MOLT', 'HHE'), ('MOLT', 'HHN'), ('MOLT', 'HHZ')]
2016-08-08T04:29:29.87Z	1.057915688	[('MOLT', 'HHE'), ('MOLT', 'HHN'), ('MOLT', 'HHZ')]
2016-08-13T09:36:16.38Z	1.259099126	[('MOLT', 'HHE'), ('MOLT', 'HHN'), ('MOLT', 'HHZ')]
2016-09-01T16:10:23.18Z	1.182552814	[('MOLT', 'HHE'), ('MOLT', 'HHN'), ('MOLT', 'HHZ')]
2016-09-07T07:19:19.25Z	1.108828545	[('MOLT', 'HHE'), ('MOLT', 'HHN'), ('MOLT', 'HHZ')]
2016-09-14T17:14:29.47Z	1.301137209	[('MOLT', 'HHE'), ('MOLT', 'HHN'), ('MOLT', 'HHZ')]
2016-09-14T17:27:37.16Z	1.109629154	[('MOLT', 'HHE'), ('MOLT', 'HHN'), ('MOLT', 'HHZ')]
2016-09-14T19:38:25.73Z	1.216846585	[('MOLT', 'HHE'), ('MOLT', 'HHN'), ('MOLT', 'HHZ')]
2016-09-14T23:38:12.12Z	1.186580896	[('MOLT', 'HHE'), ('MOLT', 'HHN'), ('MOLT', 'HHZ')]
2016-09-15T01:43:25.31Z	1.134980321	[('MOLT', 'HHE'), ('MOLT', 'HHN'), ('MOLT', 'HHZ')]
2016-09-15T04:10:13.07Z	1.20503056	[('MOLT', 'HHE'), ('MOLT', 'HHN'), ('MOLT', 'HHZ')]
2016-09-15T04:30:17.89Z	2.545910835	[('MOLT', 'HHE'), ('MOLT', 'HHN'), ('MOLT', 'HHZ')]
2016-09-15T04:55:00.00Z	1.124422312	[('MOLT', 'HHE'), ('MOLT', 'HHN'), ('MOLT', 'HHZ')]
2016-09-15T05:43:16.39Z	2.463905096	[('MOLT', 'HHE'), ('MOLT', 'HHN'), ('MOLT', 'HHZ')]
2016-09-15T05:57:26.19Z	2.372497559	[('MOLT', 'HHE'), ('MOLT', 'HHN'), ('MOLT', 'HHZ')]
2016-09-15T07:53:51.43Z	2.39303112	[('MOLT', 'HHE'), ('MOLT', 'HHN'), ('MOLT', 'HHZ')]
2016-09-15T09:48:11.11Z	1.305629849	[('MOLT', 'HHE'), ('MOLT', 'HHN'), ('MOLT', 'HHZ')]
2016-09-15T09:50:23.16Z	1.882787943	[('MOLT', 'HHE'), ('MOLT', 'HHN'), ('MOLT', 'HHZ')]
2016-09-15T09:54:22.58Z	1.588008642	[('MOLT', 'HHE'), ('MOLT', 'HHN'), ('MOLT', 'HHZ')]
2016-09-15T11:30:37.44Z	1.518980503	[('MOLT', 'HHE'), ('MOLT', 'HHN'), ('MOLT', 'HHZ')]
2016-09-15T11:33:12.55Z	1.511137962	[('MOLT', 'HHE'), ('MOLT', 'HHN'), ('MOLT', 'HHZ')]
2016-09-15T11:49:02.15Z	1.272411108	[('MOLT', 'HHE'), ('MOLT', 'HHN'), ('MOLT', 'HHZ')]
2016-09-15T13:14:09.88Z	1.271423101	[('MOLT', 'HHE'), ('MOLT', 'HHN'), ('MOLT', 'HHZ')]
2016-09-15T15:24:18.18Z	1.151963234	[('MOLT', 'HHE'), ('MOLT', 'HHN'), ('MOLT', 'HHZ')]
2016-09-15T16:54:21.31Z	-1.178925037	[('MOLT', 'HHE'), ('MOLT', 'HHN'), ('MOLT', 'HHZ')]
2016-09-16T00:04:14.88Z	1.894948244	[('MOLT', 'HHE'), ('MOLT', 'HHN'), ('MOLT', 'HHZ')]
2016-09-16T00:08:05.35Z	1.634678602	[('MOLT', 'HHE'), ('MOLT', 'HHN'), ('MOLT', 'HHZ')]
2016-09-16T01:04:53.03Z	1.486131191	[('MOLT', 'HHE'), ('MOLT', 'HHN'), ('MOLT', 'HHZ')]
2016-09-16T03:13:07.89Z	2.519844055	[('MOLT', 'HHE'), ('MOLT', 'HHN'), ('MOLT', 'HHZ')]
2016-09-16T07:51:01.40Z	-1.117176533	[('MOLT', 'HHE'), ('MOLT', 'HHN'), ('MOLT', 'HHZ')]
2016-09-16T08:11:35.96Z	2.495234251	[('MOLT', 'HHE'), ('MOLT', 'HHN'), ('MOLT', 'HHZ')]
2016-09-16T11:29:11.82Z	2.011828661	[('MOLT', 'HHE'), ('MOLT', 'HHN'), ('MOLT', 'HHZ')]
2016-09-16T15:28:12.20Z	1.542185068	[('MOLT', 'HHE'), ('MOLT', 'HHN'), ('MOLT', 'HHZ')]
2016-09-16T17:44:56.54Z	1.126542568	[('MOLT', 'HHE'), ('MOLT', 'HHN'), ('MOLT', 'HHZ')]
2016-09-17T02:28:09.34Z	1.161015153	[('MOLT', 'HHE'), ('MOLT', 'HHN'), ('MOLT', 'HHZ')]
2016-09-17T15:48:26.94Z	1.354407787	[('MOLT', 'HHE'), ('MOLT', 'HHN'), ('MOLT', 'HHZ')]
2016-09-18T02:08:10.28Z	2.457577467	[('MOLT', 'HHE'), ('MOLT', 'HHN'), ('MOLT', 'HHZ')]
2016-09-18T05:36:53.33Z	1.241078854	[('MOLT', 'HHE'), ('MOLT', 'HHN'), ('MOLT', 'HHZ')]
2016-09-18T06:19:05.25Z	1.698601723	[('MOLT', 'HHE'), ('MOLT', 'HHN'), ('MOLT', 'HHZ')]
2016-09-18T08:08:30.53Z	1.27632308	[('MOLT', 'HHE'), ('MOLT', 'HHN'), ('MOLT', 'HHZ')]
2016-09-18T13:06:53.58Z	1.481397629	[('MOLT', 'HHE'), ('MOLT', 'HHN'), ('MOLT', 'HHZ')]
2016-09-18T17:41:59.60Z	2.363923073	[('MOLT', 'HHE'), ('MOLT', 'HHN'), ('MOLT', 'HHZ')]
2016-09-18T22:11:15.17Z	1.172300816	[('MOLT', 'HHE'), ('MOLT', 'HHN'), ('MOLT', 'HHZ')]
2016-09-18T22:56:21.28Z	1.445738196	[('MOLT', 'HHE'), ('MOLT', 'HHN'), ('MOLT', 'HHZ')]
2016-09-23T08:56:50.40Z	1.242737055	[('MOLT', 'HHE'), ('MOLT', 'HHN'), ('MOLT', 'HHZ')]
2016-09-24T02:02:44.49Z	1.476219177	[('MOLT', 'HHE'), ('MOLT', 'HHN'), ('MOLT', 'HHZ')]
2016-09-24T09:18:20.68Z	2.63758707	[('MOLT', 'HHE'), ('MOLT', 'HHN'), ('MOLT', 'HHZ')]
2016-09-24T09:25:29.48Z	2.058207035	[('MOLT', 'HHE'), ('MOLT', 'HHN'), ('MOLT', 'HHZ')]
2016-09-24T09:40:55.21Z	1.170708895	[('MOLT', 'HHE'), ('MOLT', 'HHN'), ('MOLT', 'HHZ')]
2016-09-26T04:59:25.66Z	1.666303873	[('MOLT', 'HHE'), ('MOLT', 'HHN'), ('MOLT', 'HHZ')]
2016-10-03T19:50:21.41Z	2.790067196	[('MOLT', 'HHE'), ('MOLT', 'HHN'), ('MOLT', 'HHZ')]

2017-01-27T09:09:37.23Z	0.96772933	[('MOLT', 'HHE'), ('MOLT', 'HHN'), ('MOLT', 'HHZ')]
2017-01-28T13:45:22.38Z	1.304224133	[('MOLT', 'HHE'), ('MOLT', 'HHN'), ('MOLT', 'HHZ')]
2017-01-28T17:16:13.96Z	2.094419956	[('MOLT', 'HHE'), ('MOLT', 'HHN'), ('MOLT', 'HHZ')]
2017-03-22T20:25:35.76Z	1.207912207	[('MOLT', 'HHE'), ('MOLT', 'HHN'), ('MOLT', 'HHZ')]
2017-07-25T14:57:33.58Z	1.129573584	[('MOLT', 'HHE'), ('MOLT', 'HHN'), ('MOLT', 'HHZ')]
2017-08-21T01:58:31.93Z	2.185565472	[('MOLT', 'HHE'), ('MOLT', 'HHN'), ('MOLT', 'HHZ')]
2017-09-07T06:07:57.01Z	0.902037859	[('MOLT', 'HHE'), ('MOLT', 'HHN'), ('MOLT', 'HHZ')]
2017-09-20T12:30:46.93Z	0.994101644	[('MOLT', 'HHE'), ('MOLT', 'HHN'), ('MOLT', 'HHZ')]
2017-09-22T10:04:17.07Z	1.009527922	[('MOLT', 'HHE'), ('MOLT', 'HHN'), ('MOLT', 'HHZ')]
2017-09-29T06:17:44.15Z	0.896500945	[('MOLT', 'HHE'), ('MOLT', 'HHN'), ('MOLT', 'HHZ')]
2017-10-12T11:48:45.22Z	0.94391036	[('MOLT', 'HHE'), ('MOLT', 'HHN'), ('MOLT', 'HHZ')]
2018-01-30T12:06:47.92Z	1.1786654	[('MOLT', 'HHE'), ('MOLT', 'HHN'), ('MOLT', 'HHZ')]
2018-06-28T10:15:42.56Z	1.154301286	[('MOLT', 'HHE'), ('MOLT', 'HHN'), ('MOLT', 'HHZ')]
2018-08-22T11:38:45.34Z	1.184481144	[('MOLT', 'HHE'), ('MOLT', 'HHN'), ('MOLT', 'HHZ')]
2018-10-16T08:04:41.78Z	1.031161666	[('MOLT', 'HHE'), ('MOLT', 'HHN'), ('MOLT', 'HHZ')]
2018-11-12T18:25:23.30Z	0.980511189	[('MOLT', 'HHE'), ('MOLT', 'HHN'), ('MOLT', 'HHZ')]
2018-11-21T11:42:48.80Z	1.053378701	[('MOLT', 'HHE'), ('MOLT', 'HHN'), ('MOLT', 'HHZ')]
2018-11-29T11:38:47.61Z	1.046994805	[('MOLT', 'HHE'), ('MOLT', 'HHN'), ('MOLT', 'HHZ')]
2018-11-29T14:26:38.41Z	1.012661219	[('MOLT', 'HHE'), ('MOLT', 'HHN'), ('MOLT', 'HHZ')]
2018-11-29T15:19:21.81Z	1.016279936	[('MOLT', 'HHE'), ('MOLT', 'HHN'), ('MOLT', 'HHZ')]
2018-12-05T05:29:57.87Z	1.968827009	[('MOLT', 'HHE'), ('MOLT', 'HHN'), ('MOLT', 'HHZ')]
2018-12-05T05:46:23.19Z	1.786718607	[('MOLT', 'HHE'), ('MOLT', 'HHN'), ('MOLT', 'HHZ')]
2018-12-05T15:37:34.71Z	2.0712924	[('MOLT', 'HHE'), ('MOLT', 'HHN'), ('MOLT', 'HHZ')]
2018-12-06T12:18:13.00Z	1.749946833	[('MOLT', 'HHE'), ('MOLT', 'HHN'), ('MOLT', 'HHZ')]
2018-12-06T21:12:30.67Z	1.704693556	[('MOLT', 'HHE'), ('MOLT', 'HHN'), ('MOLT', 'HHZ')]
2018-12-07T07:08:00.82Z	2.014741898	[('MOLT', 'HHE'), ('MOLT', 'HHN'), ('MOLT', 'HHZ')]
2018-12-08T22:06:52.63Z	1.04930234	[('MOLT', 'HHE'), ('MOLT', 'HHN'), ('MOLT', 'HHZ')]
2018-12-10T11:47:04.69Z	1.051241994	[('MOLT', 'HHE'), ('MOLT', 'HHN'), ('MOLT', 'HHZ')]
2018-12-12T09:40:05.88Z	1.093480825	[('MOLT', 'HHE'), ('MOLT', 'HHN'), ('MOLT', 'HHZ')]
2018-12-12T13:22:03.42Z	1.714894056	[('MOLT', 'HHE'), ('MOLT', 'HHN'), ('MOLT', 'HHZ')]
2018-12-12T18:16:25.76Z	1.763864756	[('MOLT', 'HHE'), ('MOLT', 'HHN'), ('MOLT', 'HHZ')]
2018-12-13T02:55:03.34Z	1.475283384	[('MOLT', 'HHE'), ('MOLT', 'HHN'), ('MOLT', 'HHZ')]
2018-12-13T08:50:53.32Z	1.031546593	[('MOLT', 'HHE'), ('MOLT', 'HHN'), ('MOLT', 'HHZ')]
2018-12-13T11:40:00.62Z	1.020829201	[('MOLT', 'HHE'), ('MOLT', 'HHN'), ('MOLT', 'HHZ')]
2018-12-14T09:30:09.60Z	-1.047509193	[('MOLT', 'HHE'), ('MOLT', 'HHN'), ('MOLT', 'HHZ')]
2018-12-15T23:43:07.61Z	1.133704185	[('MOLT', 'HHE'), ('MOLT', 'HHN'), ('MOLT', 'HHZ')]
2018-12-18T06:05:11.48Z	1.081026435	[('MOLT', 'HHE'), ('MOLT', 'HHN'), ('MOLT', 'HHZ')]
2018-12-18T10:20:37.67Z	1.043839931	[('MOLT', 'HHE'), ('MOLT', 'HHN'), ('MOLT', 'HHZ')]
2018-12-18T12:40:05.35Z	2.356806278	[('MOLT', 'HHE'), ('MOLT', 'HHN'), ('MOLT', 'HHZ')]
2018-12-18T13:48:20.46Z	2.641542435	[('MOLT', 'HHE'), ('MOLT', 'HHN'), ('MOLT', 'HHZ')]
2018-12-18T14:05:29.05Z	2.159318686	[('MOLT', 'HHE'), ('MOLT', 'HHN'), ('MOLT', 'HHZ')]
2018-12-19T05:49:08.13Z	2.492795706	[('MOLT', 'HHE'), ('MOLT', 'HHN'), ('MOLT', 'HHZ')]
2018-12-19T16:18:38.93Z	1.493463159	[('MOLT', 'HHE'), ('MOLT', 'HHN'), ('MOLT', 'HHZ')]
2018-12-22T21:55:03.60Z	1.824152946	[('MOLT', 'HHE'), ('MOLT', 'HHN'), ('MOLT', 'HHZ')]
2018-12-27T04:48:02.73Z	1.128790379	[('MOLT', 'HHE'), ('MOLT', 'HHN'), ('MOLT', 'HHZ')]
2018-12-27T08:49:00.85Z	1.139734745	[('MOLT', 'HHE'), ('MOLT', 'HHN'), ('MOLT', 'HHZ')]
2019-01-02T17:03:35.05Z	1.875562668	[('MOLT', 'HHE'), ('MOLT', 'HHN'), ('MOLT', 'HHZ')]
2019-01-09T11:44:48.98Z	-1.004047751	[('MOLT', 'HHE'), ('MOLT', 'HHN'), ('MOLT', 'HHZ')]
2019-01-17T23:21:36.60Z	1.777813673	[('MOLT', 'HHE'), ('MOLT', 'HHN'), ('MOLT', 'HHZ')]
2019-01-17T23:22:07.34Z	-1.185319543	[('MOLT', 'HHE'), ('MOLT', 'HHN'), ('MOLT', 'HHZ')]
2019-01-18T05:41:31.38Z	1.126131296	[('MOLT', 'HHE'), ('MOLT', 'HHN'), ('MOLT', 'HHZ')]
2019-01-18T08:25:07.76Z	2.092041016	[('MOLT', 'HHE'), ('MOLT', 'HHN'), ('MOLT', 'HHZ')]
2019-01-18T18:39:42.60Z	1.273261786	[('MOLT', 'HHE'), ('MOLT', 'HHN'), ('MOLT', 'HHZ')]
2019-01-22T23:53:03.04Z	1.897991419	[('MOLT', 'HHE'), ('MOLT', 'HHN'), ('MOLT', 'HHZ')]
2019-01-24T02:36:57.85Z	1.24199605	[('MOLT', 'HHE'), ('MOLT', 'HHN'), ('MOLT', 'HHZ')]
2019-01-30T21:46:42.17Z	1.511853576	[('MOLT', 'HHE'), ('MOLT', 'HHN'), ('MOLT', 'HHZ')]
2019-02-13T08:31:11.10Z	1.047112942	[('MOLT', 'HHE'), ('MOLT', 'HHN'), ('MOLT', 'HHZ')]
2019-02-15T09:41:49.78Z	-1.057751656	[('MOLT', 'HHE'), ('MOLT', 'HHN'), ('MOLT', 'HHZ')]
2019-02-16T23:56:11.86Z	2.431566954	[('MOLT', 'HHE'), ('MOLT', 'HHN'), ('MOLT', 'HHZ')]
2019-02-17T01:25:18.18Z	2.169228554	[('MOLT', 'HHE'), ('MOLT', 'HHN'), ('MOLT', 'HHZ')]

2019-02-18T04:08:17.14Z	2.728271961	[('MOLT', 'HHE'), ('MOLT', 'HHN'), ('MOLT', 'HHZ')]
2019-02-19T12:56:56.41Z	2.373860359	[('MOLT', 'HHE'), ('MOLT', 'HHN'), ('MOLT', 'HHZ')]
2019-02-19T14:21:42.87Z	1.096698165	[('MOLT', 'HHE'), ('MOLT', 'HHN'), ('MOLT', 'HHZ')]
2019-02-19T20:31:46.06Z	1.621302009	[('MOLT', 'HHE'), ('MOLT', 'HHN'), ('MOLT', 'HHZ')]
2019-02-20T01:20:46.73Z	1.182077885	[('MOLT', 'HHE'), ('MOLT', 'HHN'), ('MOLT', 'HHZ')]
2019-02-20T03:44:21.92Z	1.394593	[('MOLT', 'HHE'), ('MOLT', 'HHN'), ('MOLT', 'HHZ')]
2019-03-01T13:28:27.05Z	2.012034655	[('MOLT', 'HHE'), ('MOLT', 'HHN'), ('MOLT', 'HHZ')]
2019-03-02T01:19:52.29Z	1.08571589	[('MOLT', 'HHE'), ('MOLT', 'HHN'), ('MOLT', 'HHZ')]
2019-03-03T03:04:12.61Z	1.059037209	[('MOLT', 'HHE'), ('MOLT', 'HHN'), ('MOLT', 'HHZ')]
2019-03-11T12:45:35.52Z	1.16518259	[('MOLT', 'HHE'), ('MOLT', 'HHN'), ('MOLT', 'HHZ')]
2019-03-28T07:41:17.14Z	1.593424082	[('MOLT', 'HHE'), ('MOLT', 'HHN'), ('MOLT', 'HHZ')]
2019-03-29T14:51:43.81Z	1.102386117	[('MOLT', 'HHE'), ('MOLT', 'HHN'), ('MOLT', 'HHZ')]
2019-04-04T10:43:48.36Z	1.112052321	[('MOLT', 'HHE'), ('MOLT', 'HHN'), ('MOLT', 'HHZ')]
2019-04-05T13:36:24.55Z	1.156163931	[('MOLT', 'HHE'), ('MOLT', 'HHN'), ('MOLT', 'HHZ')]
2019-04-10T12:16:00.71Z	-1.065327048	[('MOLT', 'HHE'), ('MOLT', 'HHN'), ('MOLT', 'HHZ')]
2019-04-16T08:33:27.51Z	1.155616522	[('MOLT', 'HHE'), ('MOLT', 'HHN'), ('MOLT', 'HHZ')]
2019-04-16T09:44:16.45Z	1.138118505	[('MOLT', 'HHE'), ('MOLT', 'HHN'), ('MOLT', 'HHZ')]
2019-04-29T08:43:48.91Z	1.096979022	[('MOLT', 'HHE'), ('MOLT', 'HHN'), ('MOLT', 'HHZ')]
2019-05-16T14:36:52.15Z	1.045184255	[('MOLT', 'HHE'), ('MOLT', 'HHN'), ('MOLT', 'HHZ')]
2019-05-22T04:59:31.23Z	1.222238064	[('MOLT', 'HHE'), ('MOLT', 'HHN'), ('MOLT', 'HHZ')]
2019-05-22T18:27:53.07Z	1.208087325	[('MOLT', 'HHE'), ('MOLT', 'HHN'), ('MOLT', 'HHZ')]
2019-05-22T18:51:23.18Z	1.27531004	[('MOLT', 'HHE'), ('MOLT', 'HHN'), ('MOLT', 'HHZ')]
2019-05-22T19:23:13.44Z	1.333123326	[('MOLT', 'HHE'), ('MOLT', 'HHN'), ('MOLT', 'HHZ')]
2019-05-22T19:25:36.79Z	1.432275295	[('MOLT', 'HHE'), ('MOLT', 'HHN'), ('MOLT', 'HHZ')]
2019-05-23T01:14:28.24Z	1.588445187	[('MOLT', 'HHE'), ('MOLT', 'HHN'), ('MOLT', 'HHZ')]
2019-05-23T02:50:45.88Z	1.557348013	[('MOLT', 'HHE'), ('MOLT', 'HHN'), ('MOLT', 'HHZ')]
2019-05-23T06:37:26.89Z	2.544663429	[('MOLT', 'HHE'), ('MOLT', 'HHN'), ('MOLT', 'HHZ')]
2019-05-23T16:05:29.59Z	1.571648002	[('MOLT', 'HHE'), ('MOLT', 'HHN'), ('MOLT', 'HHZ')]
2019-05-23T16:56:51.66Z	1.532225966	[('MOLT', 'HHE'), ('MOLT', 'HHN'), ('MOLT', 'HHZ')]
2019-05-24T17:01:40.96Z	1.710565805	[('MOLT', 'HHE'), ('MOLT', 'HHN'), ('MOLT', 'HHZ')]
2019-05-25T14:46:23.26Z	1.115467072	[('MOLT', 'HHE'), ('MOLT', 'HHN'), ('MOLT', 'HHZ')]
2019-05-26T00:29:14.00Z	1.677214503	[('MOLT', 'HHE'), ('MOLT', 'HHN'), ('MOLT', 'HHZ')]
2019-05-26T16:42:58.35Z	1.819892049	[('MOLT', 'HHE'), ('MOLT', 'HHN'), ('MOLT', 'HHZ')]
2019-05-27T10:39:24.74Z	1.145774722	[('MOLT', 'HHE'), ('MOLT', 'HHN'), ('MOLT', 'HHZ')]
2019-05-28T05:01:56.95Z	1.117665052	[('MOLT', 'HHE'), ('MOLT', 'HHN'), ('MOLT', 'HHZ')]
2019-05-29T08:26:44.00Z	2.082667589	[('MOLT', 'HHE'), ('MOLT', 'HHN'), ('MOLT', 'HHZ')]
2019-06-01T19:12:07.70Z	1.300372362	[('MOLT', 'HHE'), ('MOLT', 'HHN'), ('MOLT', 'HHZ')]
2019-06-02T00:08:30.64Z	1.16163373	[('MOLT', 'HHE'), ('MOLT', 'HHN'), ('MOLT', 'HHZ')]
2019-06-02T07:23:14.59Z	2.40823555	[('MOLT', 'HHE'), ('MOLT', 'HHN'), ('MOLT', 'HHZ')]
2019-06-05T20:02:44.47Z	1.270207286	[('MOLT', 'HHE'), ('MOLT', 'HHN'), ('MOLT', 'HHZ')]
2019-06-13T22:07:36.21Z	1.184325695	[('MOLT', 'HHE'), ('MOLT', 'HHN'), ('MOLT', 'HHZ')]
2019-06-13T22:20:56.60Z	2.08353138	[('MOLT', 'HHE'), ('MOLT', 'HHN'), ('MOLT', 'HHZ')]
2019-06-14T00:33:13.77Z	1.976020336	[('MOLT', 'HHE'), ('MOLT', 'HHN'), ('MOLT', 'HHZ')]
2019-06-14T01:47:37.82Z	1.161821008	[('MOLT', 'HHE'), ('MOLT', 'HHN'), ('MOLT', 'HHZ')]
2019-06-14T02:47:15.84Z	1.525954485	[('MOLT', 'HHE'), ('MOLT', 'HHN'), ('MOLT', 'HHZ')]
2019-06-14T02:48:17.98Z	1.740636826	[('MOLT', 'HHE'), ('MOLT', 'HHN'), ('MOLT', 'HHZ')]
2019-06-14T02:56:39.73Z	1.267897606	[('MOLT', 'HHE'), ('MOLT', 'HHN'), ('MOLT', 'HHZ')]
2019-06-14T03:21:52.42Z	1.483892679	[('MOLT', 'HHE'), ('MOLT', 'HHN'), ('MOLT', 'HHZ')]
2019-06-14T05:37:24.93Z	2.378635883	[('MOLT', 'HHE'), ('MOLT', 'HHN'), ('MOLT', 'HHZ')]
2019-06-14T05:39:02.31Z	2.050187111	[('MOLT', 'HHE'), ('MOLT', 'HHN'), ('MOLT', 'HHZ')]
2019-06-14T09:43:07.04Z	1.24945271	[('MOLT', 'HHE'), ('MOLT', 'HHN'), ('MOLT', 'HHZ')]
2019-06-15T02:15:43.88Z	1.694055557	[('MOLT', 'HHE'), ('MOLT', 'HHN'), ('MOLT', 'HHZ')]
2019-06-15T06:04:25.28Z	1.31320858	[('MOLT', 'HHE'), ('MOLT', 'HHN'), ('MOLT', 'HHZ')]
2019-06-15T19:13:19.15Z	1.185721874	[('MOLT', 'HHE'), ('MOLT', 'HHN'), ('MOLT', 'HHZ')]
2019-06-15T21:41:47.94Z	1.216351032	[('MOLT', 'HHE'), ('MOLT', 'HHN'), ('MOLT', 'HHZ')]
2019-06-16T03:03:57.37Z	1.321347713	[('MOLT', 'HHE'), ('MOLT', 'HHN'), ('MOLT', 'HHZ')]
2019-06-16T07:05:45.33Z	1.711334229	[('MOLT', 'HHE'), ('MOLT', 'HHN'), ('MOLT', 'HHZ')]
2019-06-16T08:25:07.21Z	1.475435734	[('MOLT', 'HHE'), ('MOLT', 'HHN'), ('MOLT', 'HHZ')]
2019-06-16T13:00:14.56Z	1.600146294	[('MOLT', 'HHE'), ('MOLT', 'HHN'), ('MOLT', 'HHZ')]
2019-06-16T19:52:57.31Z	1.407388806	[('MOLT', 'HHE'), ('MOLT', 'HHN'), ('MOLT', 'HHZ')]

Annex B

2019-06-16T21:46:54.12Z	1.296685338	[('MOLT', 'HHE'), ('MOLT', 'HHN'), ('MOLT', 'HHZ')]
2019-06-16T22:19:54.34Z	1.236940742	[('MOLT', 'HHE'), ('MOLT', 'HHN'), ('MOLT', 'HHZ')]
2019-06-17T02:30:28.62Z	1.528546095	[('MOLT', 'HHE'), ('MOLT', 'HHN'), ('MOLT', 'HHZ')]
2019-06-17T03:20:31.87Z	-1.086346626	[('MOLT', 'HHE'), ('MOLT', 'HHN'), ('MOLT', 'HHZ')]
2019-06-17T03:54:54.66Z	1.351271868	[('MOLT', 'HHE'), ('MOLT', 'HHN'), ('MOLT', 'HHZ')]
2019-06-17T04:05:40.26Z	1.194273949	[('MOLT', 'HHE'), ('MOLT', 'HHN'), ('MOLT', 'HHZ')]
2019-06-17T04:21:22.13Z	1.091662884	[('MOLT', 'HHE'), ('MOLT', 'HHN'), ('MOLT', 'HHZ')]
2019-06-17T05:46:06.70Z	-1.065144539	[('MOLT', 'HHE'), ('MOLT', 'HHN'), ('MOLT', 'HHZ')]
2019-06-17T06:34:24.15Z	-1.060680747	[('MOLT', 'HHE'), ('MOLT', 'HHN'), ('MOLT', 'HHZ')]
2019-06-17T07:30:21.85Z	-1.056687474	[('MOLT', 'HHE'), ('MOLT', 'HHN'), ('MOLT', 'HHZ')]
2019-06-17T10:17:07.42Z	2.271868467	[('MOLT', 'HHE'), ('MOLT', 'HHN'), ('MOLT', 'HHZ')]
2019-06-17T11:34:26.72Z	1.203222871	[('MOLT', 'HHE'), ('MOLT', 'HHN'), ('MOLT', 'HHZ')]
2019-06-17T13:19:46.58Z	1.413104296	[('MOLT', 'HHE'), ('MOLT', 'HHN'), ('MOLT', 'HHZ')]
2019-06-17T13:42:48.86Z	1.110923409	[('MOLT', 'HHE'), ('MOLT', 'HHN'), ('MOLT', 'HHZ')]
2019-06-17T19:20:37.32Z	1.660096288	[('MOLT', 'HHE'), ('MOLT', 'HHN'), ('MOLT', 'HHZ')]
2019-06-17T20:51:49.99Z	1.078945279	[('MOLT', 'HHE'), ('MOLT', 'HHN'), ('MOLT', 'HHZ')]
2019-06-17T21:32:36.54Z	1.069206953	[('MOLT', 'HHE'), ('MOLT', 'HHN'), ('MOLT', 'HHZ')]
2019-06-17T22:51:37.92Z	1.058520794	[('MOLT', 'HHE'), ('MOLT', 'HHN'), ('MOLT', 'HHZ')]
2019-06-17T23:02:27.00Z	1.087837219	[('MOLT', 'HHE'), ('MOLT', 'HHN'), ('MOLT', 'HHZ')]
2019-06-17T23:06:43.44Z	1.687104702	[('MOLT', 'HHE'), ('MOLT', 'HHN'), ('MOLT', 'HHZ')]
2019-06-18T00:02:45.57Z	1.451772451	[('MOLT', 'HHE'), ('MOLT', 'HHN'), ('MOLT', 'HHZ')]
2019-06-18T00:17:30.09Z	1.709621429	[('MOLT', 'HHE'), ('MOLT', 'HHN'), ('MOLT', 'HHZ')]
2019-06-18T02:49:29.23Z	1.284531355	[('MOLT', 'HHE'), ('MOLT', 'HHN'), ('MOLT', 'HHZ')]
2019-06-18T03:26:24.76Z	1.179882765	[('MOLT', 'HHE'), ('MOLT', 'HHN'), ('MOLT', 'HHZ')]
2019-06-18T08:23:42.93Z	1.322200179	[('MOLT', 'HHE'), ('MOLT', 'HHN'), ('MOLT', 'HHZ')]
2019-06-18T17:04:01.30Z	1.313887596	[('MOLT', 'HHE'), ('MOLT', 'HHN'), ('MOLT', 'HHZ')]
2019-06-19T16:45:42.00Z	1.740284681	[('MOLT', 'HHE'), ('MOLT', 'HHN'), ('MOLT', 'HHZ')]
2019-06-19T18:18:02.61Z	1.610262632	[('MOLT', 'HHE'), ('MOLT', 'HHN'), ('MOLT', 'HHZ')]
2019-06-20T00:04:19.24Z	1.285682321	[('MOLT', 'HHE'), ('MOLT', 'HHN'), ('MOLT', 'HHZ')]
2019-06-20T04:31:30.40Z	1.431239367	[('MOLT', 'HHE'), ('MOLT', 'HHN'), ('MOLT', 'HHZ')]
2019-06-20T10:50:13.56Z	1.625264645	[('MOLT', 'HHE'), ('MOLT', 'HHN'), ('MOLT', 'HHZ')]
2019-06-20T14:35:25.78Z	1.159529686	[('MOLT', 'HHE'), ('MOLT', 'HHN'), ('MOLT', 'HHZ')]
2019-06-20T14:54:45.36Z	1.281480789	[('MOLT', 'HHE'), ('MOLT', 'HHN'), ('MOLT', 'HHZ')]
2019-06-20T14:56:43.27Z	1.37304759	[('MOLT', 'HHE'), ('MOLT', 'HHN'), ('MOLT', 'HHZ')]
2019-06-20T15:46:36.01Z	2.524006367	[('MOLT', 'HHE'), ('MOLT', 'HHN'), ('MOLT', 'HHZ')]
2019-06-20T15:51:33.25Z	1.706258655	[('MOLT', 'HHE'), ('MOLT', 'HHN'), ('MOLT', 'HHZ')]
2019-06-20T16:55:40.69Z	1.458785772	[('MOLT', 'HHE'), ('MOLT', 'HHN'), ('MOLT', 'HHZ')]
2019-06-20T19:06:55.06Z	1.870236874	[('MOLT', 'HHE'), ('MOLT', 'HHN'), ('MOLT', 'HHZ')]
2019-06-20T19:43:25.34Z	1.137243032	[('MOLT', 'HHE'), ('MOLT', 'HHN'), ('MOLT', 'HHZ')]
2019-06-21T02:09:00.99Z	1.564216614	[('MOLT', 'HHE'), ('MOLT', 'HHN'), ('MOLT', 'HHZ')]
2019-06-21T03:15:32.75Z	1.247463942	[('MOLT', 'HHE'), ('MOLT', 'HHN'), ('MOLT', 'HHZ')]
2019-06-21T06:20:40.47Z	1.320016146	[('MOLT', 'HHE'), ('MOLT', 'HHN'), ('MOLT', 'HHZ')]
2019-06-21T16:59:40.64Z	1.629021764	[('MOLT', 'HHE'), ('MOLT', 'HHN'), ('MOLT', 'HHZ')]
2019-06-21T19:40:38.28Z	2.245651245	[('MOLT', 'HHE'), ('MOLT', 'HHN'), ('MOLT', 'HHZ')]
2019-06-21T23:17:05.46Z	1.228557944	[('MOLT', 'HHE'), ('MOLT', 'HHN'), ('MOLT', 'HHZ')]
2019-06-22T03:57:52.11Z	1.152070761	[('MOLT', 'HHE'), ('MOLT', 'HHN'), ('MOLT', 'HHZ')]
2019-06-22T07:24:26.37Z	1.967282176	[('MOLT', 'HHE'), ('MOLT', 'HHN'), ('MOLT', 'HHZ')]
2019-06-22T21:28:46.57Z	1.373442054	[('MOLT', 'HHE'), ('MOLT', 'HHN'), ('MOLT', 'HHZ')]
2019-06-22T21:34:52.57Z	1.384294629	[('MOLT', 'HHE'), ('MOLT', 'HHN'), ('MOLT', 'HHZ')]
2019-06-23T00:07:17.51Z	1.354454041	[('MOLT', 'HHE'), ('MOLT', 'HHN'), ('MOLT', 'HHZ')]
2019-06-23T00:21:27.92Z	1.712441206	[('MOLT', 'HHE'), ('MOLT', 'HHN'), ('MOLT', 'HHZ')]
2019-06-23T13:54:24.61Z	1.182717204	[('MOLT', 'HHE'), ('MOLT', 'HHN'), ('MOLT', 'HHZ')]
2019-06-23T17:27:31.83Z	2.144968033	[('MOLT', 'HHE'), ('MOLT', 'HHN'), ('MOLT', 'HHZ')]
2019-06-23T17:30:43.53Z	2.999999523	[('MOLT', 'HHE'), ('MOLT', 'HHN'), ('MOLT', 'HHZ')]
2019-06-23T18:33:33.56Z	1.458178759	[('MOLT', 'HHE'), ('MOLT', 'HHN'), ('MOLT', 'HHZ')]
2019-06-23T20:53:21.03Z	1.417662859	[('MOLT', 'HHE'), ('MOLT', 'HHN'), ('MOLT', 'HHZ')]
2019-06-27T15:47:38.54Z	1.137517691	[('MOLT', 'HHE'), ('MOLT', 'HHN'), ('MOLT', 'HHZ')]
2019-06-28T00:16:28.42Z	1.509433508	[('MOLT', 'HHE'), ('MOLT', 'HHN'), ('MOLT', 'HHZ')]
2019-06-29T10:25:14.22Z	1.066390514	[('MOLT', 'HHE'), ('MOLT', 'HHN'), ('MOLT', 'HHZ')]
2019-07-04T07:12:31.29Z	1.179478168	[('MOLT', 'HHE'), ('MOLT', 'HHN'), ('MOLT', 'HHZ')]

2019-07-04T09:29:11.65Z	1.108267188	[('MOLT', 'HHE'), ('MOLT', 'HHN'), ('MOLT', 'HHZ')]
2019-07-08T05:12:40.57Z	1.148923993	[('MOLT', 'HHE'), ('MOLT', 'HHN'), ('MOLT', 'HHZ')]
2019-07-09T00:05:46.70Z	0.789589167	[('MOLT', 'HHE'), ('MOLT', 'HHN'), ('MOLT', 'HHZ')]
2019-09-24T22:01:25.78Z	1.163854837	[('MOLT', 'HHE'), ('MOLT', 'HHN'), ('MOLT', 'HHZ')]
2019-10-06T18:03:27.13Z	1.638828278	[('MOLT', 'HHE'), ('MOLT', 'HHN'), ('MOLT', 'HHZ')]
2019-10-10T13:43:25.65Z	1.05461061	[('MOLT', 'HHE'), ('MOLT', 'HHN'), ('MOLT', 'HHZ')]
2019-10-11T15:50:49.19Z	1.146011114	[('MOLT', 'HHE'), ('MOLT', 'HHN'), ('MOLT', 'HHZ')]
2019-10-17T10:59:51.36Z	1.071949244	[('MOLT', 'HHE'), ('MOLT', 'HHN'), ('MOLT', 'HHZ')]
2019-12-11T22:38:31.05Z	1.11512506	[('MOLT', 'HHE'), ('MOLT', 'HHN'), ('MOLT', 'HHZ')]

BIBLIOGRAPHY

Ader, T., Chendorain, M., Free, M., Saarno, T., Heikkinen, P. Malin, P.E., Leary, P., Kwiatek, G., Dresen, G., Bluemle, F., Vuorinen, T. 2019. Design and implementation of a traffic light system for deep geothermal well stimulation in Finland. J Seismol. 153. https://doi.org/10.1007/s10950-019-09853-y

Ader, T., Chendorain, M., Free, M., Saarno, T., Heikkinen, P. Malin, P.E., Leary, P., Kwiatek, G., Dresen, G., Bluemle, F., Vuorinen, T.

Allmann, B.P., Shearer, P.M., 2009. Global variations of stress drop for moderate to large earthquakes: GLOBAL STRESS DROP VARIATIONS. J. Geophys. Res. Solid Earth 114. https://doi.org/10.1029/2008JB005821

Ahorner, L., 1983, Historical seismicity and present-day microearthquake activity of the Rhenish Massif, Central Europe, *in* Fuchs, K., von Gehlen, K., Mälzer, H., Murawski, H., and Semmel, A. eds., Plateau Uplift, Springer-Verlag, Berlin, Heidelberg, p. 198–221.

Bachmann, C.E., 2011. New approaches towards understanding and forecasting induced seismicity. ETH Zurich. https://doi.org/10.3929/ethz-a-006715437

Baisch, S., Koch, C., Muntendam-Bos, A., 2019. Traffic Light Systems: To What Extent Can Induced Seismicity Be Controlled? Seismol. Res. Lett. 90, 1145–1154. https://doi.org/10.1785/0220180337

Bolt, B.A., 1993. Earthquakes, Newly rev. and expanded. ed. W.H. Freeman, New York.

Bommer, J.J., Crowley, H., Pinho, R., 2015. A risk-mitigation approach to the management of induced seismicity. J. Seismol. 19, 623–646. https://doi.org/10.1007/s10950-015-9478-z

Bourne, S.J., Oates, S.J., van Elk, J., Doornhof, D., 2014. A seismological model for earthquakes induced by fluid extraction from a subsurface reservoir. J. Geophys. Res. Solid Earth 119, 8991–9015. https://doi.org/10.1002/2014JB011663

Broothaerts, M., Laenen, B. 2012. Seismiciteit en het proefproject geothermie op de Balmatt site. *Vito Rapport SCT/M1022/MB/N11-01*.

Bureau Voor Normalisatie, 2011. Belgische Norm NBN EN 1998-1 ANB, Eurocode 8 - Ontwerp en berekening van aardbevingsbestendige constructies - Deel 1: Algemene regels, seismische belastingen en regels voor gebouwen - Nationale bijlage.

Butcher, A., Luckett, R., Verdon, J.P., Kendall, J. -Michael, Baptie, B., Wookey, J., 2017. Local Magnitude Discrepancies for Near-Event Receivers: Implications for the U.K. Traffic-Light Scheme. Bull. Seismol. Soc. Am. https://doi.org/10.1785/0120160225

Camelbeeck, T., 1994. Mécanisme au foyer des tremblements de terre et contraintes tectoniques: le cas de la zone intraplaque belge. Université Catholique de Louvain, Louvain-la-Neuve.

Camelbeeck, T., Snissaert, M., Verbeiren, R., 1990. The Belgian seismic network: present and future. Cahiers du Centre Européen de Géodynamique et de Séismologie, 1, 93-102.

Camelbeeck, T., Vanneste, K., Lecocq, T., 2019. Natural and man-induced destructive earthquakes in stable continental regions. Bull. Séances- Académie R. Sci. O.-m. 64, 19.

Cesca, S., Grigoli, F., Heimann, S., González, Á., Buforn, E., Maghsoudi, S., Blanch, E., Dahm, T., 2014. The 2013 September–October seismic sequence offshore Spain: a case of seismicity triggered by gas injection? Geophys. J. Int. 198, 941–953. https://doi.org/10.1093/gji/ggu172

Cesca, S., Rohr, A., Dahm, T., 2013. Discrimination of induced seismicity by full moment tensor inversion and decomposition. J. Seismol. 17, 147–163. https://doi.org/10.1007/s10950-012-9305-8

Chamberlain, C. J., C. J. Hopp, C. M. Boese, E. Warren-Smith, D. Chambers,S. X. Chu, K. Michailos, and J. Townend. 2017. EQcorrscan: Repeating and near-repeating earthquake detection and analysis in python. Seismol. Res. Lett. https://doi.org/10.1785/0220170151

Clarke, H., Eisner, L., Styles, P., Turner, P., 2014. Felt seismicity associated with shale gas hydraulic fracturing: The first documented example in Europe. Geophys. Res. Lett. 41, 8308–8314. https://doi.org/10.1002/2014GL062047

Deckers J., De Koninck R., Bos S., Broothaers M., Dirix K., Hambsch L., Lagrou, D., Lanckacker T., Matthijs, J., Rombaut B., Van Baelen K. & Van Haren T., 2019. Geologisch (G3Dv3) en hydrogeologisch (H3D) 3D-lagenmodel van Vlaanderen – versie 3. *Studie uitgevoerd in opdracht van: Vlaams Planbureau voor Omgeving (Departement Omgeving) en Vlaamse Milieumaatschappij 2018/RMA/R/1569, 286p. + bijlagen*

Deng, K., Liu, Y., Harrington, R.M., 2016. Poroelastic stress triggering of the December 2013 Crooked Lake, Alberta, induced seismicity sequence: Poroelastinc stress-induced seismicity. Geophys. Res. Lett. 43, 8482–8491. https://doi.org/10.1002/2016GL070421

Eaton, D.W., Mahani, A.B., 2015. Focal Mechanisms of Some Inferred Induced Earthquakes in Alberta, Canada. Seismol. Res. Lett. 86, 1078–1085. https://doi.org/10.1785/0220150066

Ellsworth, W.L., 2013. Injection-Induced Earthquakes. Science 341, 1225942–1225942. https://doi.org/10.1126/science.1225942

Evans, K.F., Zappone, A., Kraft, T., Deichmann, N., Moia, F., 2012. A survey of the induced seismic responses to fluid injection in geothermal and CO2 reservoirs in Europe. Geothermics 41, 30–54. https://doi.org/10.1016/j.geothermics.2011.08.002

Fischer, T., Hainzl, S., 2017. Effective Stress Drop of Earthquake Clusters. Bull. Seismol. Soc. Am. 107, 2247–2257. https://doi.org/10.1785/0120170035

Gardner, J.K., and Knopoff, L., 1974, Is the sequence of earthquakes in Southern California, with aftershocks removed, Poissonian? Bulletin of the Seismological Society of America, v. 64, no. 5, p. 1363–1367.

Geller, R.J., 1976, Scaling relations for earthquake source parameters and magnitudes: Bulletin of the Seismological Society of America, v. 66, no. 5, p. 1501–1523.

Giardini, D., 2009. Geothermal quake risks must be faced. Nature 462, 848–849.

Goebel, T.H.W. & Brodsky, E.E. (2018) The spatial footprint of injection wells in a global compilation of induced earthquake sequences. Science (80-.)., 361, 899–904, American Association for the Advancement of Science. https://doi.org/10.1126/science.aat5449

Goertz-Allmann, B.P., Goertz, A., Wiemer, S., 2011. Stress drop variations of induced earthquakes at the Basel geothermal site: Stress Drop of Induced Earthquakes in Basel. Geophys. Res. Lett. 38, n/a-n/a. https://doi.org/10.1029/2011GL047498

Grünthal, G. (Ed.), 1998. European Macroseismic Scale 1998 (EMS-98), Cahiers du Centre Européen de Géodynamique et de Séismologie. European Centre for Geodynamics and Seismology, Luxembourg.

Grünthal, G., Bosse, C., and Stromeyer, D., 2009, Die neue Generation der probabilistischen seismische Gefährdungseinschätzuing der Bundesrepublik Deutschland - Version 2007 mit Anwendung für die Erdbeben-Lastfälle der DIN 19700:2004-07 “Stauanlagen”: GeoForschungsZentrum.

Gutenberg, B., and Richter, C.F., 1944, Frequency of earthquakes in California: Bulletin of the Seismological Society of America, v. 34, p. 185–188.

Hicks, S.P., Verdon, J., Baptie, B., Luckett, R., Mildon, Z.K., Gernon, T., 2019. A Shallow Earthquake Swarm Close to Hydrocarbon Activities: Discriminating between Natural and Induced Causes for the 2018–2019 Surrey, United Kingdom, Earthquake Sequence. Seismol. Res. Lett. 90, 2095-2110. https://doi.org/10.1785/0220190125

Hiramatsu, Y., Yamanaka, H., Tadokoro, K., Nishigami, K., Ohmi, S., 2002. Scaling law between corner frequency and seismic moment of microearthquakes: Is the breakdown of the cube law a nature of earthquakes?: SCALING LAW OF MICROEARTHQUAKES. Geophys. Res. Lett. 29, 52-1-52–4. https://doi.org/10.1029/2001GL013894

Huang, Y., Beroza, G.C., Ellsworth, W.L., 2016. Stress drop estimates of potentially induced earthquakes in the Guy-Greenbrier sequence: Stress drop variations of induced earthquakes. J. Geophys. Res. Solid Earth 121, 6597–6607. https://doi.org/10.1002/2016JB013067

Hsieh, P.A. & Bredehoeft, J.D. (1981) A reservoir analysis of the Denver earthquakes: A case of induced seismicity. J. Geophys. Res. Solid Earth, 86, 903–920, American Geophysical Union (AGU). https://doi.org/10.1029/jb086ib02p00903

Huang, Y., Ellsworth, W.L., Beroza, G.C., 2017. Stress drops of induced and tectonic earthquakes in the central United States are indistinguishable. Sci. Adv. 3, e1700772. https://doi.org/10.1126/sciadv.1700772

Induced Seismicity Potential in Energy Technologies, 2013. National Academies Press, Washington, D.C. https://doi.org/10.17226/13355

INERIS 2019. Seismic hazard and risk analysis at Balmatt. Part1: Source mechanism analysis. Confidential Ineris report - 200066 - 830488 - v1.0. 20 p.

Kaiser, J., 1950. Untersuchungen über das Auftreten von Geräuschen beim Zugversuch. TH München, Munich.

Kanamori, H., 1996. Initiation process of earthquakes and its implications for seismic hazard reduction strategy. Proc. Natl. Acad. Sci. 93, 3726–3731. https://doi.org/10.1073/pnas.93.9.3726

Kendall, J.M., Butcher, A., Stork, A.L., Verdon, J.P., Luckett, R., Baptie, B.J. 2019. How big is a small earthquake? Challenges in determining microseismic magnitudes. EAGE 37, 51-56.

Kettlety, T., Verdon, J.P., Werner, M.J. & Kendall, J.M. (2020) Stress Transfer From Opening Hydraulic Fractures Controls the Distribution of Induced Seismicity. J. Geophys. Res. Solid Earth, 125, American Geophysical Union (AGU). https://doi.org/10.1029/2019jb018794

Kim, K.-H., Ree, J.-H., Kim, Y., Kim, S., Kang, S.Y., Seo, W., 2018. Assessing whether the 2017 M_w 5.4 Pohang earthquake in South Korea was an induced event. Science 360, 1007–1009. https://doi.org/10.1126/science.aat6081

Király, E., Gischig, V., Karvounis, D., Wiemer, S., 2014. Validating Models to Forecasting Induced Seismicity Related to Deep Geot hermal Energy Projects, in: Thirty-Ninth Workshop on Geothermal Reservoir Engineering. Presented at the Thirty-Ninth Workshop on Geothermal Reservoir Engineering, Stanford, p. 9.

Lecocq, T., 2011. L'activité sismique en Ardenne et sa relation avec la tectonique active: PhD. thesis, Université Libre de Bruxelles.

Lecocq, T. 2019. On the seismic noise levels and component polarities recorded by the local ROB-NIRAS and VITO seismic stations. *Internal report. Royal Observatory of Belgium. 20 November 2019.*

Lecocq, T., Camelbeeck, T., 2017. Induced Seismic Activity at the Balmatt-site. Report on the seismic activity recorded during the injection tests. *Internal report. Royal Observatory of Belgium, Uccle*. *21p.*

Lee, W.H.K., Lahr, J.C., 1972. Hypo71: a computer program for determining hypocentre, magnitude, and first motion pattern of local earthquakes. U.S. Geol. Surv. Open File Rep. 72–223 (100 pp.).

Luckett, R., Ottemöller, L., Butcher, A., Baptie, B., 2019. Extending local magnitude *M* L to short distances. Geophys. J. Int. 216, 1145–1156. https://doi.org/10.1093/gji/ggy484

Majer, E.L., Baria, R., Stark, M., Oates, S., Bommer, J., Smith, B., Asanuma, H., 2007. Induced seismicity associated with Enhanced Geothermal Systems. Geothermics 36, 185–222. https://doi.org/10.1016/j.geothermics.2007.03.003

McNamara, D.E., Buland, R.P. 2004. Ambient Noise Levels in the Continental United States. BSSA 94, 1517-1527.

McNamara, D.E., Benz, H.M., Herrmann, R.B., Bergman, E.A., Earle, P., Holland, A., Baldwin, R., Gassner, A., 2015. Earthquake hypocenters and focal mechanisms in central Oklahoma reveal a complex system of reactivated subsurface strike-slip faulting: Earthquake Source Parameters in Oklahoma. Geophys. Res. Lett. 42, 2742–2749. https://doi.org/10.1002/2014GL062730

Megies, T., Wasserman, J. 2014. Microseismicity observed at a non-pressure-stimulated geothermal power plant. Geothermics 52, 36-49. http://dx.doi.org/10.1016/j.geothermics.2014.01.002

Meier, M.-A., Heaton, T., Clinton, J., 2016. Evidence for universal earthquake rupture initiation behavior: Universal Earthquake Rupture Initiation. Geophys. Res. Lett. 43, 7991–7996. https://doi.org/10.1002/2016GL070081

Mignan, A., Broccardo, M., Wiemer, S., Giardini, D., 2017. Induced seismicity closed-form traffic light system for actuarial decision-making during deep fluid injections. Sci. Rep. 7. https://doi.org/10.1038/s41598-017-13585-9

Mousavi, S.M., Ogwari, P.O., Horton, S.P. & Langston, C.A. (2017) Spatio-temporal evolution of frequency-magnitude distribution and seismogenic index during initiation of induced seismicity at Guy-Greenbrier, Arkansas. Phys. Earth Planet. Inter., 267, 53–66, Elsevier B.V. https://doi.org/10.1016/j.pepi.2017.04.005

Mulargia, F., Gasperini, P., and Tinti, S., 1987, Contour mapping of Italian seismicity: Tectonophysics, v. 142, no. 2-4, p. 203–216.

Musson, R.M.W., 2011, SHARE Deliverable 3.7a : Assessment of activity rates for seismic source zones.

Onwuemeka, J., Liu, Y., Harrington, R.M., 2018. Earthquake Stress Drop in the Charlevoix Seismic Zone, Eastern Canada. Geophys. Res. Lett. 45, 12,226-12,235. https://doi.org/10.1029/2018GL079382

Oprsal, I., Eisner, L., 2014. Cross-correlation—an objective tool to indicate induced seismicity. Geophys. J. Int. 196, 1536–1543. https://doi.org/10.1093/gji/ggt501

Orazi, M., D'Auria, L., Tramelli, A., Buonocunto, C., Capello, M., Caputo, A., and Scarpato, G. 2013. The seismic monitoring network of Mt. Vesuvius. Annals of Geophysics, 56(4), 0450.

Ottemöller, L., 2005. The 7 May 2001 induced seismic event in the Ekofisk oil field, North Sea. J. Geophys. Res. 110. https://doi.org/10.1029/2004JB003374

Peterson, J. 1993. Observation and modeling of seismic background noise. U.S. Geol. Surv. Tech. Rept. 93-322, 1–95.

Reamer, S.K., and Hinzen, K.G., 2004, An earthquake catalog for the Northern Rhine area, Central Europe (1975-2002): Seismological Research Letters, v. 75, no. 6, p. 713–725.

Ritter, J.R.R., Jordan, M., Christensen, U.R., and Achauer, U., 2001, A mantle plume below the Eifel volcanic fields , Germany: Earth and Planetary Science Letters, v. 186, p. 7–14.

Rivas, J.A., Castellon, J.A., Maravilla, J.N., 2005. Seven years of reservoir seismic monitoring at Berlín Geothermal Field, Usulután, El Salvador, in: Proceedings World Geothermal Congress 2005. Presented at the World Geothermal Congress, Antalya, Turkey, p. 8 pp.

Segall, P., 1989. Earthquakes triggered by fluid extraction. Geology 17, 942. https://doi.org/10.1130/0091-7613(1989)017<0942:ETBFE>2.3.CO;2

Shapiro, S.A., 2008. Microseismicity: a tool for reservoir characterization. https://app.knovel.com/web/toc.v/cid:kpMATRC00E/viewerType:toc//root_slug:microseismicity-a-tool?kpromoter=marc. ISBN: 978-90-73781-70-2

Shapiro, S.A., Dinske, C., 2009. Fluid-induced seismicity: Pressure diffusion and hydraulic fracturing. Geophys. Prospect. 57, 301–310. https://doi.org/10.1111/j.1365-2478.2008.00770.x

Stork, A.L., Verdon, J.P., Kendall, J.-M., 2014. The robustness of seismic moment and magnitudes estimated using spectral analysis: The robustness of seismic moment and magnitudes estimates. Geophys. Prospect. 62, 862–878. https://doi.org/10.1111/1365-2478.12134

Trutnevyte E., Wiemer S. 2017. Tailor-made risk governance for induced seismicity of geothermal energy projects: An application to Switzerland. Geothermics, forthcoming, http://dx.doi.org/10.1016/j.geothermics.2016.10.006.

Uhrhammer, R., 1986, Characteristics of Northern and Central California Seismicity: Earthquake Notes, v. 57, no. 1, p. 21.

Ungemach, P., Antics, M., Papachristou, M., 2005. Sustainable Geothermal Reservoir Management, in: Proceedings World Geothermal Congress 2005. Presented at the World Geothermal Congress, Antalya, Turkey, p. 12 pp.

Utsu, K., 2002, Relationships between magnitude scales, *in* Lee, W.H.K., Kanamori, H., Jennings, P.C., and Kisslinger, P.C. eds., International Handbook of Earthquake & Engineering Seismology, Part A, Academic Press, p. 733–746.

Van Baelen, H., Wouter, L., Sillen, X. 2019. Overleg tussen Vito en ONDRAF/NIRAS over het geothermieproject BALMATT. Meeting 26 september 2019.

Van Noten, K., Lecocq, T., Shah, A. & Camelbeeck, T. 2015. Seismotectonic significance of the 2008-2010 Walloon Brabant seismic swarm in the Brabant Massif (Belgium). Tectonophysics 656, 20-38. https://doi.org/10.1016/j.tecto.2015.05.026

Van Noten, K., Lecocq, T., Hinzen, K.-G., Sira, C. & Camelbeeck, T. 2017. Path and site effects deduced from merged transfrontier internet macroseismic data of two recent M4 earthquakes in NW Europe using a grid cell approach. Solid Earth 8, 453-477. https://doi.org/10.5194/se-8-453-2017

Vanneste, K., Camelbeeck, T., De Vos, W., Degrande, G., Dusar, M., Haegeman, W., Schevenels, M., Vancampenhout, P., Van Dyck, J., and Verbeeck, K., 2009, Compilatiestudie betreffende de seismiciteit in Vlaanderen: Vlaamse Overheid, Departement Leefmilieu, Natuur en Energie, VLA07–4.2.

Verbeeck, 2019. Deterministic seismic hazard assessment in the Belgian Campine basin at the Mol/Dessel site: From seismic source to site effect. PhD thesis. KULeuven. 398p.

Verbeeck, K., Vanneste, K., Camelbeeck, T. 2011. Seismic-loading analysis of the near-surface disposal facility for category-A radioactive waste (cAt) in the municipality of Dessel, Belgium. Part 2: Elastic modeling and experimental determination of the seismic transfer function at the site. *NIROND-TR 2009-03-02, Version 1, 31 October 2011.*

Verdon, J.P., 2014. Significance for secure CO_2 storage of earthquakes induced by fluid injection. Environ. Res. Lett. 9, 064022. https://doi.org/10.1088/1748-9326/9/6/064022

Verdon, J.P., Baptie, B.J., Bommer, J.J., 2019. An Improved Framework for Discriminating Seismicity Induced by Industrial Activities from Natural Earthquakes. Seismol. Res. Lett. 90, 1592-1611. https://doi.org/10.1785/0220190030

Verdon, J.P., Kendall, J.-M., White, D.J., Angus, D.A., 2011. Linking microseismic event observations with geomechanical models to minimise the risks of storing CO2 in geological formations. Earth Planet. Sci. Lett. 305, 143–152. https://doi.org/10.1016/j.epsl.2011.02.048

Verdon, J.P., Stork, A.L., Bissell, R.C., Bond, C.E., Werner, M.J., 2015. Simulation of seismic events induced by CO2 injection at In Salah, Algeria. Earth Planet. Sci. Lett. 426, 118–129. https://doi.org/10.1016/j.epsl.2015.06.029

Weichert, D.H., 1980, Estimation of the earthquake recurrence parameters for unequal observation periods for different magnitudes: Bulletin of the Seismological Society of America, v. 70, no. 4, p. 1337–1346.

Willacy, C., van Dedem, E., Minisini, S., Li, J., Blokland, J.-W., Das, I., Droujinine, A., 2019. Full-waveform event location and moment tensor inversion for induced seismicity. GEOPHYSICS 84, KS39–KS57. https://doi.org/10.1190/geo2018-0212.1

Woo, J. -U., Kim, M., Sheen, D. -H., Kang, T. -S., Rhie, J., Grigoli, F., Ellsworth, W.L., et al. (2019) An In-Depth Seismological Analysis Revealing a Causal Link Between the 2017 M W 5.5 Pohang Earthquake and EGS Project. J. Geophys. Res. Solid Earth, 124, 13060–13078. https://doi.org/10.1029/2019JB018368

Wu, Q., Chapman, M., Chen, X., 2018. Stress-Drop Variations of Induced Earthquakes in Oklahoma. Bull. Seismol. Soc. Am. 108, 1107–1123. https://doi.org/10.1785/0120170335

Zoback, M.L., Zoback, M., 1980. State of stress in the conterminous United States. J. Geophys. Res. Solid Earth 85, 6113–6156. https://doi.org/10.1029/JB085iB11p06113

Zoback, M.L., Zoback, M.D., 1989. Chapter 24: Tectonic stress field of the continental United States, in: Geological Society of America Memoirs. Geological Society of America, pp. 523–540. https://doi.org/10.1130/MEM172-p523